



University of Crete
Interdepartmental P-g. S. P.

<< Optics & Vision >>

**Wave guiding method for the
characterization of Spiropyran doped
polymeric matrices and Zr doped
Sol – Gels**

Ioanna Sakellari

**Supervisors:
David Gray
Maria Farsari**

**March – October 2007
Heraklion - Crete**



Πανεπιστήμιο Κρήτης
Διατμηματικό Π.Μ.Σ.

<< Οπτική & Όραση >>

**Χρήση της μεθόδου κυματοδήγησης για τον
χαρακτηρισμό πολυμερικών μητρών
εμπλουτισμένων με το φωτοχρωμικό μόριο
της Σπιροπυράνης και Sol – Gel
εμπλουτισμένα με Zr**

Ιωάννα Σακελλάρη

Η παρούσα εργασία υπεβλήθη ως μέρος των υποχρεώσεων για την απονομή του μεταπτυχιακού διπλώματος ειδίκευσης του Διατμηματικού Μεταπτυχιακού Προγράμματος Σπουδών «Οπτική και Όραση» και παρουσιάστηκε στην Τριμελή Επιτροπή αποτελούμενη από τους:

1. Μαρία Φαρσάρη
2. David Gray
3. Ιωάννης Ζαχαράκης

Επιβλέποντες:
David Gray, Μαρία Φαρσάρη

Μάρτιος – Οκτώβριος 2007, Ηράκλειο - Κρήτης

Εισαγωγή

Κατά την πραγματοποίηση της παρούσης εργασίας αναπτύχθηκε η τεχνική σύζευξης πρίσματος για τον χαρακτηρισμό λεπτών υμενίων. Σε αυτήν τη μέθοδο, ένα πρίσμα χρησιμοποιείται ως μέσο για να συζευχθεί επαρκώς η δέσμη ενός λέιζερ μέσα σε λεπτά διηλεκτρικά φιλμ κυματοδήγησης. Αυτή η σύζευξη επιτρέπει τον ακριβή υπολογισμό του φάσματος των κυματοδηγούμενων ρυθμών, σύμφωνα με το οποίο μπορούν να καθοριστούν ο δείκτης διάθλασης και το πάχος των υμενίων. Διάφορα φιλμ προετοιμάστηκαν κατά την πειραματική διαδικασία, τα οποία περιείχαν είτε πολυμερικές μήτρες εμπλουτισμένες με φωτοχρωμικά υλικά, είτε υβριδικά υλικά εμπλουτισμένα με ανόργανα μόρια. Η μεταβολή του δείκτη διάθλασης ήταν η βασική ιδιότητα που χρησιμοποιήθηκε για την διερεύνηση των αλλαγών που προκαλούνται στην πολυμερική μήτρα με την ενσωμάτωση τέτοιων ενθεμάτων.

Τα φωτοχρωμικά υλικά έχουν την ιδιότητα να υπόκεινται σε αντιστρεπτές διαμορφώσεις μεταξύ διαφορετικών ισομερικών μορφών κατά την ακτινοβολή τους με κατάλληλο μήκος κύματος ακτινοβολίας αλλάζοντας, κατ'αυτόν τον τρόπο, τη δομή, τον προσανατολισμό, τη διαμόρφωση και τη συσσωμάτωση των μακρομοριακών μητρών στις οποίες έχουν εγκλωβιστεί φωτοχρωμικά μόρια με διάφορους τρόπους. Τα πολυμερή παρουσιάζουν μία αντιστρεπτή μεταβολή στο δείκτη διάθλασής τους ως αποτέλεσμα των φωτοχημικών αλλαγών των φωτοχρωμικών μορίων που έχουν ενσωματωθεί στους μακρομοριακούς σκελετούς. Στην περίπτωση μας, οι φωτοπροκαλούμενες αλλαγές των πολυμερών θα ελεγχθούν φωτοχημικά με τη χρήση λεπτών φιλμ PEMMA, ως πολυμερική μήτρα, στην οποία περιέχεται το φωτοχρωμικό μόριο της Σπιροπυράνης σε διάφορες αναλογίες.

Η φωτοχρωμική συμπεριφορά της Σπιροπυράνης βασίζεται στην αντιστρεψιμότητα μεταξύ της κλειστής, άχρωμης μορφής της Σπιροπυράνης και της ανοικτής, έγχρωμης χρωστικής της Μεροκυανίνης προκαλούμενη από τη διέγερση της πρώτης με υπεριώδη ακτινοβολία. Καταγράφηκαν τα φάσματα απορρόφησης και διάδοσης κατά τη διέγερση με UV ακτινοβολία προκειμένου να παρατηρήσουμε τις φωτοπροκαλούμενες μεταβολές των λεπτών φιλμ με PEMMA εμπλουτισμένα με Σπιροπυράνη. Οι μοριακές

διαμορφώσεις κατά την ακτινοβολή έχουν ως αποτέλεσμα την μεταβολή του μεγίστου απορρόφησης από την υπεριώδη περιοχή μηκών κύματος προς την ορατή περιοχή μεταξύ 500nm – 600nm προκαλώντας αλλαγές στο δείκτη διάθλασης μετά τη διέγερση. Αρχικά, τα πειραματικά αποτελέσματα δείχνουν ότι η ενσωμάτωση της Σπιροπυράνης στην PEMMA προκαλεί μια αύξηση του δείκτη διάθλασης της πολυμερικής μήτρας συνοδευόμενη από μια ισχυρή γραμμική αύξηση σε σχέση με την περιεκτικότητα της Σπιροπυράνης. Η ακόλουθη διέγερση των φιλμ με υπεριώδη ακτινοβολία μεταβάλλει το δείκτη διάθλασης, όπως αναμενόταν, προς μικρότερες τιμές σε πλήρη συμφωνία με τη γραμμική αύξηση που παρουσιάστηκε πριν τη διέγερση. Επαναλαμβανόμενοι κύκλοι της αντιστρεπτής διαμόρφωσης των φωτοχρωμικών μορίων καταγράφεται μετέπειτα, και η απώλεια της απόκρισης σε σχέση με το χρόνο εξαιτίας της «κούρασης» του υλικού επιδεικνύεται σαφώς. Οι μετρήσεις της μεταβολής του δείκτη διάθλασης και η καταγραφή του φάσματος διάδοσης έλαβαν χώρα με τη χρήση ενός He-Ne λέιζερ στα 543.5 nm, ενώ η διέγερση των φιλμ πραγματοποιείται με ένα παλμικό λέιζερ στα 308nm και συχνότητας παλμών στα 3Hz.

Η τεχνική σύζευξης πρίσματος χρησιμοποιήθηκε, επίσης, για τον χαρακτηρισμό λεπτών φιλμ που παρασκευάστηκαν με τη μέθοδο Sol – Gel. Η μέθοδος αυτή είναι μία ευρέως διαδιδόμενη τεχνική για την ενσωμάτωση οργανικών μορίων εντός ενός δικτύου ανόργανων μορίων σε οποιαδήποτε αναλογία οδηγώντας στη δημιουργία ενός υβριδικού οργανικού – ανόργανου υλικού. Αυτά τα υβρίδια είναι πολύ εύκολα στην σύνθεσή τους, στην επεξεργασία, στις οπτικές και μηχανικές τους ιδιότητες. Η ενσωμάτωση τέτοιων ενθεμάτων έχει ως αποτέλεσμα τη δημιουργία υλικών με διαφορετική φυσικοχημική συμπεριφορά έχοντας μία διαφορετική επίδραση στην τιμή του δείκτη διάθλασης.

Τα υλικά που παρασκευάσαμε με τη μέθοδο Sol - Gel αποτελούνται από αλκοξίδια του πυριτίου, στα οποία έχουν ενσωματωθεί μεθακρυλικές ενώσεις. Ο έλεγχος το δείκτη διάθλασης επιτυγχάνεται με την προσθήκη $Zr(OPr)_4$. Με βάση τα αποτελέσματα που προέκυψαν κατά την πειραματική διαδικασία, η ενσωμάτωση ζirkονίου είχε ως αποτέλεσμα την αύξηση του δείκτη διάθλασης των φιλμ που περιείχαν αλκοξίδια του πυριτίου οδηγώντας, επιπλέον, σε μία γραμμική μεταβολή του δείκτη διάθλασης σε σχέση με την περιεκτικότητα σε ζirkόνιο. Οι μετρήσεις πραγματοποιήθηκαν με τη χρήση δύο λαζερ: ενός He – Ne με μήκος κύματος ακτινοβολίας στα 632.5nm και ενός

υπέρυθρου λέζερ στα 825nm. Παρόμοια συμπεριφορά παρατηρήθηκε κατά τη χρήση και των δύο μηκών κύματος. Οι μεταβολές στο δείκτη διάθλασης που επιτεύχθηκαν είναι της τάξης του 0.06: συγκεκριμένα από 1.4898 (χωρίς την προσθήκη ζirkονίου) έως την τιμή 1.5437 για το ορατό λέζερ και για το υπέρυθρο από 1.4744 έως 1.5343.

CONTENTS

<i>Introduction</i>	8
<i>Chapter 1</i>	10
<i>Theory of optical waveguides</i>	10
1.1 Thin film waveguide modes	10
1.2 Coupling of a plane wave in a planar waveguide	15
1.2.1 Coupling of TE modes	19
1.2.2 Coupling of TM modes	21
1.3 Ray-Optic Approach	23
1.3.1 Waveguiding of light in a planar three layer guide	23
1.3.2 The discrete nature of propagation constant β	28
1.4 The prism-film coupler	36
1.4.1 Light-waves progression in the film	39
<i>Chapter 2</i>	41
<i>Photochromism</i>	41
2.1 Definition of photochromism	41
2.2 One-photon and two-photon systems	44
2.3 Common photochromic systems	46
2.4 Families of organic photochromic compounds	50
2.4.1 Spiropyran (NO ₂ -BIPS)	53
2.5 Fatigue	60
<i>Chapter 3</i>	62
<i>Sol-Gel process</i>	62
<i>Chapter 4</i>	66
<i>Methodology</i>	66
4.1 Measurement of the refractive index and the thickness of a thin film	66
4.2 Determination of thin film thickness using reflectance spectroscopy (number of modes expected)	71
4.3 Measurement of the change in the refractive index based on the intensity profile of a thin film	74
<i>Chapter 5</i>	78
<i>Experimental process</i>	78
5.1 Validation of the prism – film coupler method	80

5.2 Application of the prism-film coupler method for the calculation of the refractive index of unknown materials	84
5.3 Measurement of the change in refractive index based on the intensity profile of a thin film	96
5.4 Fatigue	106
<i>Chapter 6</i>	<i>107</i>
<i>Conclusions</i>	<i>107</i>
<i>Appendix A</i>	<i>113</i>
<i>Appendix B</i>	<i>116</i>
<i>Appendix C</i>	<i>118</i>
<i>References</i>	<i>119</i>

Introduction

During the realization of the present project, the prism - film coupling technique was developed for the characterization of thin films. According to this method, a prism is used as a device to couple efficiently a laser beam into thin-film dielectric wave guides. This coupler allows an accurate measurement of the spectrum of propagating modes, from which the refractive index and the thickness of the film can be determined. Several films prepared containing either photochromic materials doped polymeric matrices or hybrid organic materials doped with inorganic molecules. Refractive index variation was the basic property used to investigate the changes induced into the host matrices by the incorporation of these dopants.

Photochromic molecules undergo reversible transformations between different isomeric forms, upon irradiation at appropriate laser wavelengths, thereby altering the structural, conformational, orientational, and aggregational states of macromolecular matrices entrapping photochromic molecules in various manners. Polymers exhibit a reversible refractive index change as a result of the molecular photochemistry of photochromic molecules dissolved in or attached to macromolecular skeletons. In our case, the photoinduced changes of polymers will be controlled photochemically by employing thin films of PEMMA, as a polymer composite, containing the photochromic molecule of spiropyran (SP-NO₂) in different ratios.

The photochromic behavior of spiropyrans is based on the reversibility between the closed, colorless spiropyran form and the colored “open” merocyanine dye obtained by excitation of the former by ultra-violet irradiation. Absorption and transmission spectra were recorded upon UV excitation in order to observe the photoinduced changes of Spiropyran doped PEMMA films. Molecular transformations during the photoprocess resulted in a shift in absorption maxima from the UV region to 500nm – 600nm band inducing changes in refractive index after excitation. At first, experimental results show that the incorporation of Spiropyran into PEMMA induces an increase in refractive index of the host polymer accompanied by a strong linear increment in relation to the

percentage Spiropyran. The following excitation of the films by UV irradiation shifts the refractive index, as expected, to smaller values in accordance with the linear increment presented before excitation. Repeating cycles of the reversible transformations of the photochromic molecules were recorded afterwards, and the loss of performance over time due to chemical degradation of the material (fatigue) is well demonstrated. Refractive index measurements and transmission spectra records take place with the use of a 543.5 nm He-Ne laser, while the excitation of our films is achieved through a pump laser of 308 nm wavelength at 3 Hz pump frequency.

Prism - film coupler technique also used for the characterization of thin films prepared by Sol – gel method. This process is a favorable method for the introduction of organic molecules inside an inorganic network at any ratio leading to so-called hybrid organic – inorganic nanocomposites. These hybrids are extremely versatile in their composition, processing, optical and mechanical properties. The incorporation of dopants results in hybrid materials with distinctive physicochemical behaviors having a direct effect on the refractive index value.

The material produced by sol-gel synthesis constituted of a silicon alkoxide species that also possessed methacrylate functionality. Control over the films refractive index achieved through zirconium – n – propoxide doping. According to the results obtained during the experimental process, incorporation of zirconium resulted in an increase in refractive index of silicon alkoxides films leading, furthermore, to a linear variation in refractive index in relation to the percentage zirconium. The measurements take place with the use of two lasers: a He – Ne working at 632.8nm and an infrared at 825nm. Similar behaviour observed for both laser wavelengths. The variations in refractive index achieved are of the order of 0.06: from 1.4898 (no zirconium added) to 1.5437 for the former and for the latter from 1.4744 to 1.5343.

Chapter 1

Theory of optical waveguides

Thin dielectric films are routinely used as planar light guides. The main parameters characterizing such films are the refractive index and the film thickness. For the determination of these parameters, the prism-film coupler method has proved to be one of the most favorable techniques among other methods. Both parameters are obtained simultaneously and with good accuracy by measuring the coupling angles at the prism. Hence, the main topics discussed in this chapter are physics of light waves in thin films, the fundamentals of the prism – film coupler method for coupling a light beam into and out of a thin film, as well as, the mathematical procedures for the evaluation.

1.1 Thin film waveguide modes

As well known, the optical waveguide relates to the way that light waves propagate confined, via total internal reflection, within a dielectric medium. The main characteristic of such a structure is that the optical waves travel in the waveguide in distinct optical modes, each mode considered as *a spatial distribution of optical energy in one or more directions*.

A dielectric planar waveguide, such as a thin film, is characterized by parallel planar boundaries with respect to one (x) direction, but is infinite in extent in the lateral directions (z and y), as shown in Figure 1. More explicitly, a typical thin film waveguide

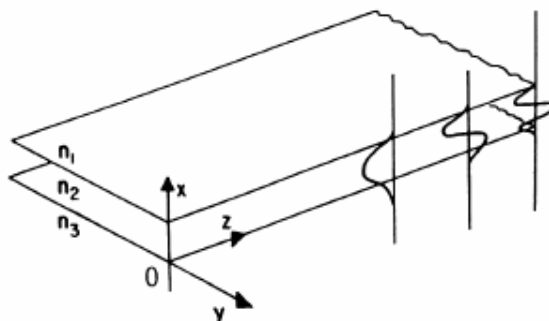


Figure 1. Three layer planar waveguide. Three modes are shown, representing distributions of electric field in the x direction

is a dielectric film sandwiched between two media (the substrate n_s and the cover n_c) of lower refractive indices in relation to that of the film (n_f). A well known way to *couple* large amounts of light, i.e. to excite any selected mode of propagating light wave, in planar optical waveguides is the *prism coupler*.

The prism-film coupler, given schematically in Figure 2, consists of a rectangular and isosceles (in our case) prism with a refractive index n_p (higher than that of the film), tightened against a planar waveguide. The prism is placed above the thin film guide and is separated from it by a small gap of low refractive index material (air). The air gap thickness, S , is controlled with a pushing screw at the back of the waveguide.

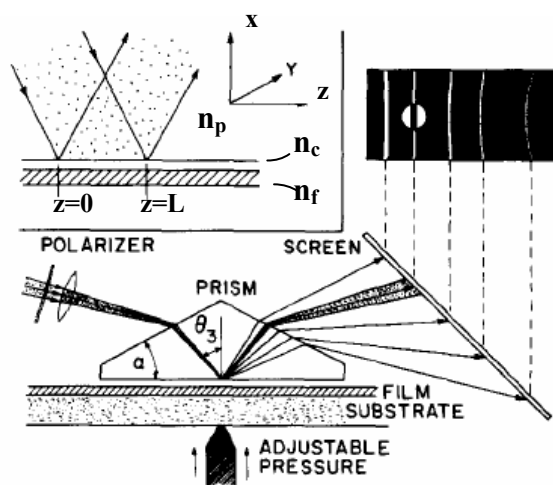


Figure 2. Prism – film coupler

In general, the coupling of an incident laser beam by a prism into a thin film is governed by the incident angle of the beam on the prism base. The laser beam enters the prism, reaches the base at an angle of incidence θ_3 and is totally reflected. Normally, the incident power is totally reflected. Under certain conditions, however, the light energy can be transferred into the film via resonant frustrated total internal reflection, i.e. via evanescent waves excited in the air layer [1]. The evanescent waves, having traversed the gap, drive electrons in the frustrating medium and in turn generate a wave that significantly alters the field configuration, thereby permitting energy flow. The part of the incident energy that has tunneled through the low-index gap into the film, is then alternately reflected at the film-substrate and at the film-gap interfaces so that a zig-zag propagation along the guide results (Figure 3).

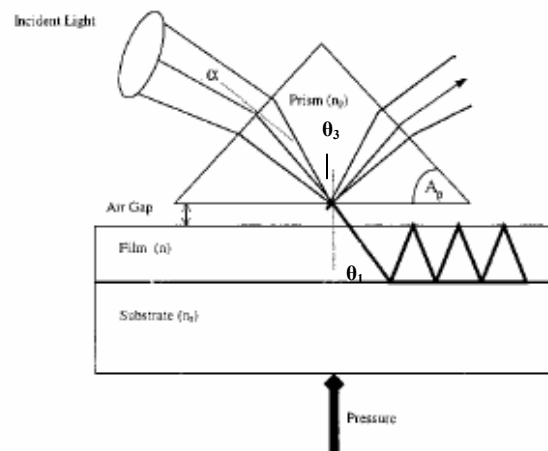


Figure 3. Zig-zag waves in the waveguide mode of the film

The optical energy can be transferred from the prism to the film and back from the film to the prism, a process similar to the quantum mechanical phenomenon of *optical tunneling*.

Here the air space and the substrate are the potential barriers.

The coupling, described above, occurs only when resonant conditions inside the waveguide are met and takes place along the entire width of the incident beam (from $z = 0$ to $z = L$, Figure 2). The conditions for coupling are [2]

- i) The incident beam must have the proper angle of incidence so that the evanescent fields in the gap S travel with the same velocity as the mode to be

excited in the film. In other words, the component of the propagation constant parallel to the film surface must be equal for the wave in the prism and the wave in the guiding film. This leads to a finite number of *discrete incidences* of the input laser beam, for which the light can be strongly coupled into the guide, called **synchronism angles**.

- ii) As the modes of the film have a distinct polarization (TM or TE), the incident beam must have the same polarization as the mode to be excited.
- iii) The film must be placed close enough to the prism base ($S \sim \lambda/2$).

In order to state the condition (i) more precisely, let the propagation constant of the mode under consideration be β . Similarly, for the incident beam at the prism base the component of the propagation vector parallel to the film is $kn_p \sin \theta_3$, $k = \omega/c$. Then a direction θ_3 , is a synchronous one if $\beta = kn_p \sin \theta_3$. Hence, by proper orientation of the direction of the incident beam, with respect to the prism surface and therefore with the film surface, it is possible to excite any of the film guided modes. Alternatively, the propagation constant β or the phase velocity ω/β of a mode can be determined by measuring the synchronous direction of θ_3 of that mode.

Furthermore, when light is coupled into one of the waveguide modes, because of film inhomogeneities, the optical energy is rapidly scattered into other modes and is *then* coupled back to the outside medium through the other face of the prism. The returned light wave in the prism, therefore, consists of many waveguide modes [10, 44]; each of them appears in its own synchronous direction. We thus see on the screen, where the light beam is reflected, a series of bright lines (called **m-lines**) with a bright spot on one of this lines (shown in Figure 2). Each line represents a mode (i.e. the light propagated in the film) of different order m , while the bright spot is the beam totally reflected from the base of the prism. When the spot is on the m^{th} bright line, this means that we are exciting the m^{th} mode. Perfect coupling is indicated by the appearance of a small black line inside the spot and represents the energy lost from the excited mode by scattering. With increasing coupling the lines become brighter first, and then become broader and shift. Their positions and line widths depend critically on the spacing S of the coupling gap. For infinite gap width they converge against the modes of the free guide, i.e. the modes in the

absence of the prism. The m lines are, therefore, a direct display of the spectrum of the film modes.

The phase velocity of a light wave in a thin film waveguide depends on the thickness of the film and the mode of propagation. If the characteristics of the prism ($\varepsilon \equiv$ prism angle and n_p) are known, as well as the substrate refractive index, n_s , and at least two modes are supported by the waveguide, we can estimate both thickness and refractive index of the guiding film. In addition, the intensity distribution of the reflected spot gives the m line's profile. A change in the coupling efficiency (i.e. the thickness S of the air layer between the prism and the guide) changes the shape of the m line, whereas a change in the refractive index of the film causes a pure shift of the m line (with no distortion of the m line's profile) [3]. This is the property that permits the detection of the modifications of the refractive index of a thin film.

1.2 Coupling of a plane wave in a planar waveguide

In the present section, the coupling is analyzed by the method of plane-wave expansion. For this purpose, we consider first a single plane wave that is incident on the simple three-layer planar waveguide structure of Figure 1 in the absence of the prism. The layers are all assumed to be infinite in the y and z directions and layers 1 and 3 to be semi-infinite in the x direction. Light waves are assumed to be propagating in the z direction, the plane of incidence is the $x\hat{O}z$. An equivalent mathematical definition of a mode is that represents an electromagnetic field which is a solution of Maxwell's wave equation

$$\nabla^2 E(\mathbf{r}) = (n^2/c^2) \partial^2 E(\mathbf{r})/\partial t^2 \quad , \quad (1.1)$$

where \mathbf{E} is the electric field vector, \mathbf{r} is the radius vector, n is the index of refraction, and c is the speed of light in vacuum. All media considered homogenous and isotropic. The solutions of (1.1) have the form

$$\mathbf{E}(\mathbf{r},t) = \mathbf{E}(\mathbf{r}) e^{i[\omega t - \phi(\mathbf{r})]} \quad , \quad (1.2)$$

where ω is the radian frequency and ϕ is a phase function. Substituting (1.2) into (1.1) we obtain

$$\nabla^2 E(\mathbf{r}) + k^2 n^2(\mathbf{r})E(\mathbf{r}) = 0 \quad , \quad (1.3)$$

where $k \equiv \omega/c$. In Cartesian coordinates, the above equation becomes

$$\partial^2 E_x/\partial x^2 + \partial^2 E_x/\partial y^2 + \partial^2 E_x/\partial z^2 + k^2 n^2(x,y,z) E_x = 0 \quad (1.3.i)$$

$$\partial^2 E_y/\partial x^2 + \partial^2 E_y/\partial y^2 + \partial^2 E_y/\partial z^2 + k^2 n^2(x,y,z) E_y = 0 \quad (1.3.ii)$$

$$\partial^2 E_z/\partial x^2 + \partial^2 E_z/\partial y^2 + \partial^2 E_z/\partial z^2 + k^2 n^2(x,y,z) E_z = 0 \quad (1.3.iii)$$

If we assume, for convenience, a uniform plane wave propagating in the z direction, i.e. $\varphi(\mathbf{r}) = \beta z$ (where β is a propagation constant), and there is no explicit z dependence of $E(\mathbf{r})$, that is $E(\mathbf{r}) = \mathbf{E}(x, y) e^{-i\beta z}$, then (1.3) becomes

$$\partial^2 E(x, y) / \partial x^2 + \partial^2 E(x, y) / \partial y^2 + [k^2 n^2(x, y, z) - \beta^2] E(x, y) = 0 \quad (1.4)$$

where $\mathbf{E}(x, y) = E_x(x, y)\hat{i} + E_y(x, y)\hat{j} + E_z(x, y)\hat{k}$

Since the waveguide is assumed infinite in the y direction ($\partial/\partial y \rightarrow 0$), by writing (1.4) separately for the three regions in x , we get:

$$\begin{aligned} \text{Region 1. } & \partial^2 E(x, y) / \partial x^2 + [k^2 n_1^2 - \beta^2] E(x, y) = 0 \\ \text{Region 2. } & \partial^2 E(x, y) / \partial x^2 + [k^2 n_2^2 - \beta^2] E(x, y) = 0 \\ \text{Region 3. } & \partial^2 E(x, y) / \partial x^2 + [k^2 n_3^2 - \beta^2] E(x, y) = 0 \end{aligned} \quad (1.5)$$

where $E(x, y)$ is one of the Cartesian components of $\mathbf{E}(x, y)$.

It is recalled that for the transverse modes (TE modes) the wave vector \mathbf{E} is normal to the plane of incidence, E_x and E_z are zero and E_y has no y or z dependence since the layers are assumed to be infinite in these directions. Thereby, no reflections take place in y and z directions precluding, therefore, the possibility of interference, and thus, no resultant standing waves occur [4]. Hence, the non-zero components are H_x , H_z and E_y .

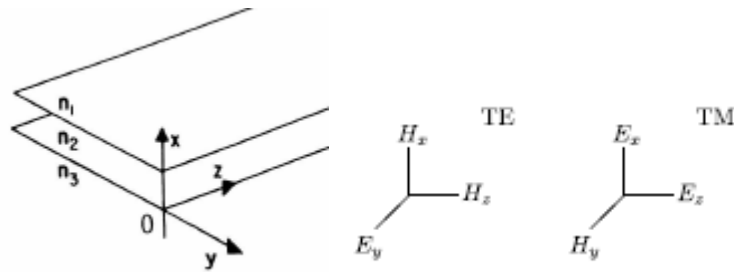


Figure 4. TE and TM modes

In accordance, for the longitudinal modes (TM) the wave vector \mathbf{E} is parallel to the plane of incidence, H_x and H_z are zero and H_y has no y or z dependence. The non vanishing field components are E_x , E_z , H_y [5]. Consequently, the vector of the electric field becomes

$$\mathbf{E}(x, y) = \mathbf{E}(x) = E_x(x)\hat{i} + E_y(x)\hat{j} + E_z(x)\hat{k}$$

$$\text{TE waves: } \mathbf{E}(x) = E_y(x)\hat{j}$$

$$\text{TM waves: } \mathbf{E}(x) = E_x(x)\hat{i} + E_z(x)\hat{k}$$

Hence, for the case of TE plane waves traveling in the z direction, with propagation constant β , the Maxwell's wave equation reduces to

$$\nabla^2 E_y = (n_i^2/c^2) \partial^2 E_y / \partial t^2, \quad i=1, 2, 3$$

with solutions of the form $E_y(x, z, t) = E_y(x) e^{i(\omega t - \beta z)}$ and the equation (1.5) gets the final form for each region separately:

$$\text{Region 1. } \partial^2 E_y(x) / \partial x^2 + [k^2 n_1^2 - \beta^2] E_y(x) = 0$$

$$\text{Region 2. } \partial^2 E_y(x) / \partial x^2 + [k^2 n_2^2 - \beta^2] E_y(x) = 0 \quad (1.6)$$

$$\text{Region 3. } \partial^2 E_y(x) / \partial x^2 + [k^2 n_3^2 - \beta^2] E_y(x) = 0$$

where n_1 , n_2 , n_3 are the refractive indices of the cover (air), the film (n_f) and the substrate (n_s) respectively. The solutions of (1.6) are either sinusoidal or exponential functions of x in each of the regions, depending on whether the term $(k^2 n_i^2 - \beta^2)$, $i=1, 2, 3$ is greater than or less than zero [6]. In order to support propagating modes in region 2, the film refractive index n_2 must be greater than both n_1 and n_3 ($n_2 > n_3 > n_1$). That is the necessary condition for wave guiding in the film.

In detail, when $\beta > kn_2$, the term $(k^2 n_i^2 - \beta^2)$, $i=1, 2, 3$ is less than zero for $i=1, 2, 3$, therefore, the function $E(x)$ must be exponential in all three regions and only the mode shape shown in Figure 5(a) could satisfy the boundary conditions of $E_y(x)$, $\partial E_y(x) / \partial x$

being continuous at the interfaces. This mode is not physically realizable because the field increases unboundedly in regions 1 and 2 implying infinite energy. When $kn_2 > \beta > kn_3$, the term $(k^2 n_i^2 - \beta^2)$ is less than zero for $i = 1, 3$ and positive for $i = 2$. The field distribution is, thus, a standing wave (sinusoidal solution) in the film and exponential in the substrate and in the air space. Modes (b) and (c) are well confined **waveguided modes**, generally referred to as the zeroth order and first order transverse electric modes, TE_0 and TE_1 . In this sense, for values of β between kn_2 and kn_3 such modes can be supported. Next, if β is greater than kn_1 , but less than kn_3 , a mode like that in (d) will result. The fields in this case, are standing waves in the film and the substrate, but exponential in the air space. This type of mode which is confined at the air interface, but sinusoidally varying at the substrate, is often called a **substrate radiation mode**. It can be supported by the waveguide structure, but because it is continually losing energy from the wave guiding region 2 to the substrate region 3 as it propagates, it tends to be damped out over a short distance. Finally, if β is less than kn_1 , the solution for $E(x)$ is oscillatory in all three regions of the waveguide structure. These modes are not guided modes because the energy is free to spread out of the wave guiding region 2. They are generally referred to as the **air radiation modes** of the waveguide structure.

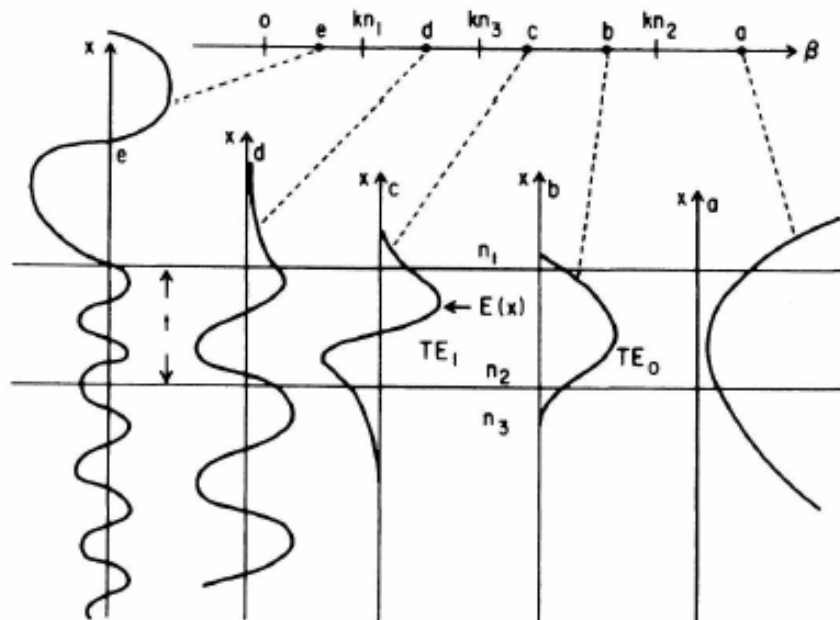


Figure 5a – 5b – 5c - 5d. modes in aplanar waveguide

1.2.1 Coupling of TE modes

Keeping in mind the analysis made in the previous section and also the assumption that the only reflections occurring are those in the x direction at n_2 - n_1 and n_2 - n_3 interfaces (resulting in standing waves there), the transverse function $E_y(x)$ has the general form

$$A \exp(-qx) \quad , \quad x > 0 \quad (1.7.i)$$

$$E_y(x) = B \cos(hx) + C \sin(hx) \quad , \quad -t_g < x < 0 \quad (1.7.ii)$$

$$D \exp[p(x + t_g)] \quad , \quad x < -t_g \quad (1.7.iii)$$

where A, B, C, D, q, h and p are all constants that can be determined by matching the boundaries conditions requiring the continuity of E_y and $H_z = i\omega\mu \partial E_y / \partial x$ (i.e. $\partial E_y / \partial x$ to be continuous).

In order to determine the constant h , we substitute the equation (1.7.ii) into the one of the equations (1.6) standing for the region 2 ($-t_g < x < 0$). The resulting expression we get is that

$$h = [(k^2 n_2^2 - \beta^2)]^{1/2} \quad (1.8.i)$$

In similar way, on substituting the equation (1.7.i) into (1.6) for the region 1 ($x > 0$), we obtain an expression for the constant q , that is

$$q = [\beta^2 - k^2 n_1^2]^{1/2} \quad (1.8.ii)$$

Finally, by substituting the equation (1.7.iii) into the one of (1.6) for the region 3 ($x < -t_g$) we get an expression for the constant p , that is

$$p = [\beta^2 - k^2 n_3^2]^{1/2} \quad (1.8.iii)$$

Furthermore, if we satisfy the boundary conditions (E_y and $\partial E_y / \partial x$ continuous at the interfaces), the above constants A, B, C, D can be determined and the procedure provides three equations in four unknowns, so that the solution for E_y can be expressed in terms of

a single constant C. More explicitly, because of the continuity of the E_y at $x = 0$ and by matching the equations (1.7.i) and (1.7.ii), we get

$$\begin{aligned} A \sin(0) + B \cos(0) &= C \exp(0) \quad \Rightarrow \\ B &= C \end{aligned}$$

In similar way, because of the continuity of $H_z = i\omega\mu \partial E_y / \partial x$ at $x = 0$:

$$\begin{aligned} A h \cos(0) - B h \sin(0) &= -C q \exp(0) \quad \Rightarrow \\ A &= -C q / h \end{aligned}$$

Because of the continuity of E_y at $x = -t_g$:

$$\begin{aligned} A \sin(-h t_g) + B \cos(h t_g) &= D \exp(-p t_g) \quad \Rightarrow \\ D &= [-A \sin(h t_g) + B \cos(h t_g)] / \exp(-p t_g) \end{aligned}$$

Keeping in mind the three last expressions, the form of E_y simplifies as follows:

$$\begin{aligned} E_y(x) &= C \exp(-qx) \quad , \quad x > 0 & (1.9.i) \\ E_y(x) &= C [\cos(hx) - (q/h) \sin(hx)] \quad , \quad -t_g < x < 0 & (1.9.ii) \\ E_y(x) &= C [\cos(ht_g) + (q/h) \sin(ht_g)] \exp[p(x+t_g)] \quad , \quad x < -t_g & (1.9.iii) \end{aligned}$$

Finally, the last boundary condition that has remained to be satisfied is that of the continuity of $H_z = i\omega\mu \partial E_y / \partial x$ at $x = -t_g$. Using the above simplified expression for the E_y , we derive the following expression:

$$-h \sin(-h t_g) - h (q/h) \cos(-h t_g) = p [(q/h) \sin(h t_g) + \cos(h t_g)] ,$$

or, after simplification

$$\tan(h t_g) = (p + q) / [h (1 - pq / h^2)] \quad , \quad (1.10)$$

The transcendental equation (1.10) in conjunction with (1.8) can be solved graphically, by plotting right and left hand sides as a function of β and noting the intersection points. The result is a set of discrete allowed values of β corresponding to the allowed modes. For each β_m , the corresponding values of q_m , h_m and p_m can be determined from the set of equations of (1.8).

1.2.2 Coupling of TM modes

Considering the case of the TM modes, the resulting field components are

$$H_y(x, z, t) = H_y(x) e^{i(\omega t - \beta z)}, \quad (1.11.i)$$

$$E_x(x, z, t) = (i/\omega\epsilon) \partial H_y / \partial z = (\beta/\omega\epsilon) H_y(x) e^{i(\omega t - \beta z)}, \quad (1.11.ii)$$

$$E_z(x, z, t) = - (i/\omega\epsilon) \partial H_y / \partial x, \quad (1.11.iii)$$

The transverse magnetic component H_y is given by

$$C \exp(-qx) \quad , \quad x > 0 \quad (1.12.i)$$

$$H_y(x) = B \cos(hx) + A \sin(hx) \quad , \quad -t_g < x < 0 \quad (1.12.ii)$$

$$D \exp(px) \quad , \quad x < -t_g \quad (1.12.iii)$$

where the constants h , q , p have already been defined by (1.8).

The form of the E_z component, therefore, according to equation (1.11.iii) will be

$$(iq/\omega\epsilon_0 n_1^2) C \exp(-qx) \quad , \quad x > 0 \quad (1.13.i)$$

$$E_z(x) = -(ih/\omega\epsilon_0 n_1^2) [A \cos(hx) - B \sin(hx)] \quad , \quad -t_g < x < 0 \quad (1.13.ii)$$

$$-(ip/\omega\epsilon_0 n_3^2) D \exp(px) \quad , \quad x < -t_g \quad (1.13.iii)$$

Because of the continuity of H_y and E_y at the interfaces ($x = 0$, $x = -t_g$):

For $x = 0$, the equations (1.12.ii) and (1.13.ii) result in

$$A \sin(0) + B \cos(0) = C \exp(0) \Rightarrow B = C$$

and

$$-(ih/\omega\epsilon_0 n_1^2) [A \cos(h0) - B \sin(h0)] = (iq/\omega\epsilon_0 n_1^2) C \exp(-q0) \Rightarrow$$

$$C = (-n_1^2 h / n_2^2 q) A$$

For $x = -t_g$ and in relation to equation (1.12), we obtain:

$$B \cos(-h t_g) + A \sin(-h t_g) = D \exp(-p t_g) \Rightarrow$$

$$D = [B \cos(h t_g) - A \sin(h t_g)] / \exp(-p t_g)$$

By setting $p' = (n_2^2 / n_3^2) p$ and $q' = (n_2^2 / n_1^2) q$, then we get

$$B = C = - (h / q') A$$

$$D = -A [\sin (h t_g) + (h / q') \cos (h t_g)] \exp (p t_g)$$

Consequently, we can rewrite the equation (1.12) as follows:

$$-(h/q') A \exp(-qx) \quad , \quad x > 0 \quad (1.14.i)$$

$$H_y(x) = A[-(h/q') \cos(hx) + \sin(hx)] \quad , \quad -t_g < x < 0 \quad (1.14.ii)$$

$$-A[-(h/q') \cos(h t_g) + \sin(h t_g) \exp[p(t_g + x)]] \quad , \quad x < -t_g \quad (1.14.iii)$$

Finally, because of the continuity of E_y at the interface $x = -t_g$, we get:

$$-(1/n_2^2) [-(h^2/q') \sin(h t_g) + h \cos(h t_g)] = (p/n_3^2)[(h/q') \cos(h t_g) + \sin(h t_g)] \Rightarrow$$

$$\tan(h t_g) = [-h (p' + q')] / (p' q' - h^2) \quad (1.15)$$

The equation (1.15) is analogous to (1.10) for the TE modes. The number of modes that can be supported depends on the thickness t of the waveguiding layer and on ω , n_1 , n_2 and n_3 . For a given t , n_1 , n_2 , n_3 there is a cutoff frequency ω_c below which waveguiding can not occur.

1.3 Ray-Optic Approach

The modes described above can be explained simply by the Snell law of refraction and the related total internal reflection phenomenon in optics. In the so-called ray-optic approach the plane waves propagating along the z direction, supported one or more optical modes, are generally represented by rays moving in zigzag paths in the x-z plane undergoing total internal reflection at the interfaces bounding the waveguide. The plane waves, comprising each mode, travel with the same phase velocity. However, because the angle of reflection in the zig-zag path differs, the light propagating in each mode travels in the z direction with a different phase velocity, which is characteristic of that mode.

1.3.1 Waveguiding of light in a planar three layer guide

The correlation between the physical – optic and ray - optic can be seen by referring back to the equation (1.8.i)

$$h = [(k^2 n_2^2 - \beta^2)]^{1/2}$$

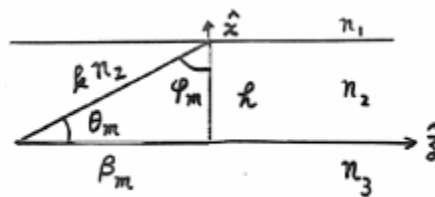


Figure 6. Ray – optic approach

A mode with a z direction propagation constant β_m and an x direction propagation constant h can be represented by a plane wave traveling at an angle $\theta_m = \tan^{-1}(h/ \beta_m)$ with respect to the z direction, having a propagation constant kn_2 . The term kn_2 is constant, while θ_m , β_m , h are all parameters associated with the m^{th} mode, with different values for each mode.

In the ray-optic approach, we consider a ray of light propagating within the three layer waveguide structure. In this manner, we denote as φ_1 , φ_2 , φ_3 the angles measured between the light paths and the normals of the interfaces in the substrate, film, and air respectively. It is also recalled that $n_2 > n_1 > n_3$. Then, from the Snell law we have

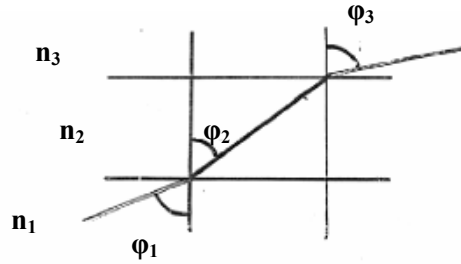


Figure 7. A ray of light propagating within three layer waveguide structure

$$\sin\varphi_1 / \sin\varphi_2 = n_2 / n_1$$

and

$$\sin\varphi_3 / \sin\varphi_2 = n_2 / n_3$$

On total internal reflection (TIR) at:

$n_2 - n_1$ interface

$$\varphi_1 = 90^\circ$$

$$\varphi_2 \geq \varphi_c = \sin^{-1}(n_1/n_2) \text{ for TIR at point B} \quad (1.16)$$

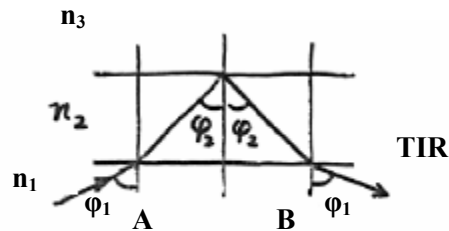


Figure 8. Total internal reflection (TIR) at $n_2 - n_1$ interface

$n_2 - n_3$ interface

$$\begin{aligned} \varphi_3 &= 90^\circ \\ \varphi_2 &= \sin^{-1}(n_3/n_2 \sin \varphi_3) \end{aligned} \quad (1.17)$$

Hence,

$$\sin^{-1}(n_1/n_2) \leq \sin^{-1}(n_3/n_2 \sin \varphi_3)$$

or

$$\varphi_3 \geq \sin^{-1}(n_1/n_3) \quad (1.18)$$

On total internal reflection (TIR) at $n_2 - n_3$ interface:

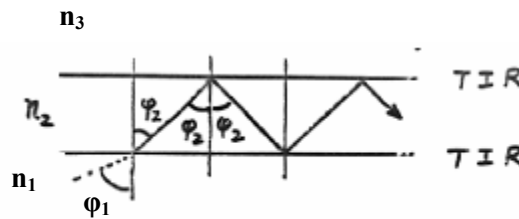


Figure 9. Total internal reflection (TIR) at $n_2 - n_3$ interface

$$\begin{aligned} \varphi_3 &> 90^\circ, \text{ totally confined} \\ \varphi_2 &> \varphi_{2c} = \sin^{-1}(n_3/n_2) \end{aligned} \quad (1.19)$$

Assuming that we begin to increase the angle of incidence, φ_1 , gradually from 0, we find the following behavior. When φ_2 is small and as long as $\varphi_2 < \sin^{-1}(n_1/n_2)$, a light wave starts from the air space above the film (point A), then is refracted into the film, and is finally refracted again into the substrate. In this case, the waves propagate freely in all three media – air, film, and substrate – and they represent the radiation fields that fill all the three spaces (air modes). Next, as φ_2 is increased to a value larger than the critical angle $\varphi_2 \geq \varphi_c = \sin^{-1}(n_1/n_2)$ of the film – air interface (at the point B we assume $\sin \varphi_1 > 1$, which is an impossible condition), the light wave is totally reflected at the film – air boundary. Now, the wave can no longer propagate freely in the air space and the light

energy in the film radiates into the substrate only corresponding to a substrate radiation mode. As long as φ_2 increases so that $\sin^{-1}(n_1/n_2) < \varphi_2 < \sin^{-1}(n_3/n_2)$, the wave is partially confined. Finally, when φ_2 is larger than the critical angle $\sin^{-1}(n_3/n_2)$ of the film – substrate interface, the light wave is totally reflected at both the upper and lower surfaces of the film. The energy flow is confined within the film (waveguide modes). The ray paths for all possible modes are demonstrated below.

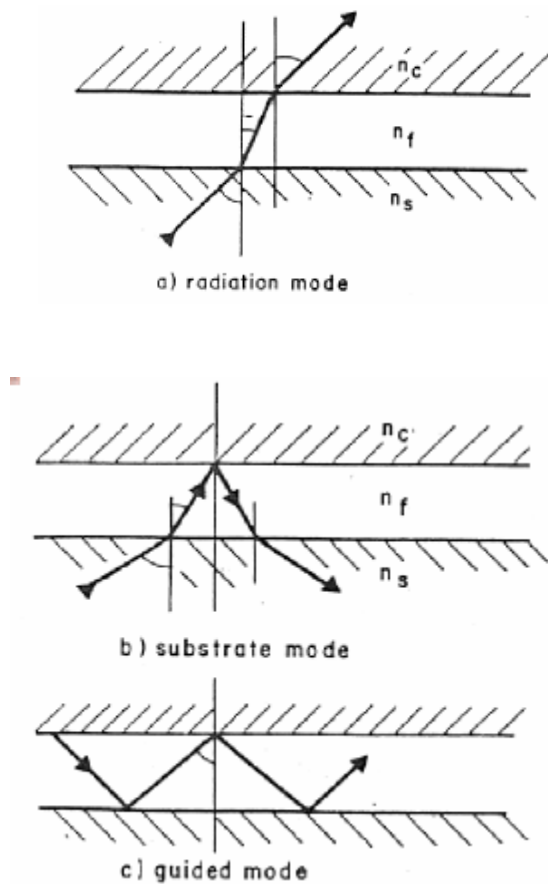


Figure 10. Zigzag picture of optical ray pattern

The conditions given above for determining what type of modes can be supported by a particular waveguide as a function of φ_2 , are exactly equivalent by the conditions given by (1.6) as a function of β [46]. In this sense, referring back to Figure 6, it is indicated that β must be less than kn_2 , since

$$\sin\varphi_2 = \beta / kn_2 \leq 1$$

else we get the unrealizable inequality of $\sin\varphi_2 > 1$. Furthermore, for β greater than kn_3 but less than kn_2 , indicates that waveguide modes occur.

$$\begin{aligned} kn_3 &\leq \beta \leq kn_2 \\ kn_3 &\leq kn_2 \sin\varphi_2 \leq kn_2 \\ \varphi_2 &\geq \varphi_c = \sin^{-1}(n_3/n_2) \end{aligned}$$

or

$$n_2 > n_3$$

Similarly, if β is greater than kn_1 but less than kn_3 , indicates that substrate modes will be supported.

$$\begin{aligned} kn_1 &\leq \beta \leq kn_3 \\ kn_1 &\leq kn_2 \sin\varphi_2 \leq kn_3 \\ \varphi_2 &\geq \varphi_c = \sin^{-1}(n_1/n_2) \end{aligned}$$

Finally, if $\beta \leq kn_1$, only radiation modes result

$$\sin\varphi_2 \leq kn_1 / kn_2 = n_1 / n_2$$

which is the same condition given by $\varphi_2 \geq \sin^{-1}(n_1/n_2)$.

Thus, equivalence has been demonstrated between the ray-optic and physical optic approaches in regard to the determination of mode type.

1.3.2 The discrete nature of propagation constant β

As it is shown in Figure 10c, in the waveguide modes, the light wave follows a zig – zag path. The light energy is trapped in the film as the wave is totally reflected back and forth between the two film surfaces. As already stated in a previous section, the electric field of the propagation mode in the waveguide is described by

$$E(x, y, z) = A(z) E(x, y) = A(z) E(x) \quad (1.20)$$

where $A(z)$ is a complex amplitude which includes the phase term $e^{i\beta z}$ and $E(x, y)$ is the solution for the field distribution of the mode in the waveguide [8]. In this manner, we can represent this zig-zag path by two wave vectors A_1 and B_1 being the complex amplitudes of the incident and reflected beams respectively, as shown in Figure 11. In accordance, we denote the waves in the film by A_2 and B_2 . We, then, divide the wave vectors into vertical and horizontal components. The horizontal components of the wave vectors A_2 and B_2 are equal, indicating that the waves propagate with a constant speed in a direction parallel to the film. Thus, since the waves are coupled, they all have the same phase constant β along the z axis. By convention, we consider that all the A_i waves propagate towards the lower right, and the B_i waves toward the upper right. When the upward and downward traveling waves are superposed, they form a standing wave field pattern across the thickness of the film. By changing θ_1 , we change the direction of the wave vectors A_2 and B_2 and thus their horizontal and vertical components. Consequently, we change the wave velocity parallel to the film, as well as, the standing wave field pattern across the film.

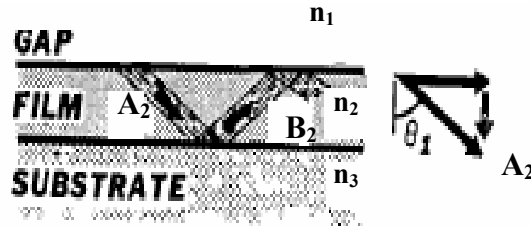


Figure 11. The wave vectors A_2 and B_2 decomposed in vertical and horizontal components

Since there is much overlapping of the waves as they travel in the zig-zag path, in order to avoid decay of optical energy due to destructive interference as the waves travel through the guide, the total phase change for a point on a wavefront that travels from the

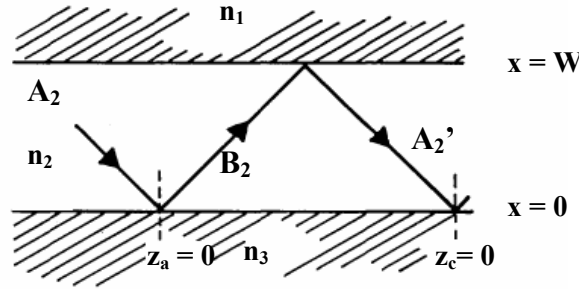


Figure 12. Zig – zag path of the wave vectors A_2 and B_2

$n_2 - n_3$ interface to the $n_2 - n_1$ interface and back again must be a multiple of 2π . In detail, because the reflections at both film interfaces are total, the amplitudes A_2 and A_2' can differ only by a phase Δ . After subsequent zig-zags, the wave has phase differences 2Δ , 3Δ , 4Δ ... relative to A_1 . In general, the superposition of such a set of plane waves is zero except when $\Delta = 2m\pi$ with integer m . In that case the beams A_2 , A_2' and all further reflections of this beam interfere constructively. As shown in Figure 11, the vertical components of the wave vectors A_2 and B_2 , have a magnitude $kn_2\cos\theta_1$. The phase change for the plane to cross the thickness W of the film twice (up and down) is then $2kn_2W\cos\theta_1$. In addition, the wave suffers a phase change at the lower and upper film boundary due to total internal reflection.

Thereby, in general, if we set as R the reflection coefficient at an interface, we can write

$$B = R A$$

where B is the reflected wave and A the incident one. We denote as φ_1 , φ_2 the angles measured between the light paths and the normals of the interfaces

At the interface $n_2 - n_1$ (for this example $n_2 < n_1$):

Snell's law:

$$n_1 \sin\varphi_1 = n_2 \sin\varphi_2$$

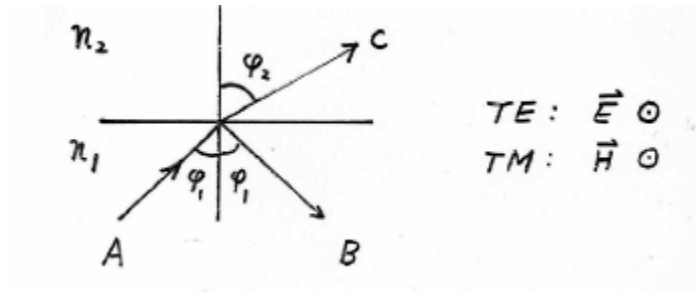


Figure 13. Reflection at an interface, $n_1 > n_2$

On total internal reflection (TIR)

$$n_2 < n_1$$

$$\varphi_2 > \varphi_1$$

$$\varphi_c = \sin^{-1}(n_2/n_1)$$

Fresnel formulas:

$$R_{TE} = [n_1 \cos\varphi_1 - n_2 \cos\varphi_2] / [n_1 \cos\varphi_1 + n_2 \cos\varphi_2]$$

$$R_{TE} = [n_1 \cos\varphi_1 - (n_2^2 - n_1 \sin^2\varphi_1)^{1/2}] / [n_1 \cos\varphi_1 + (n_2^2 - n_1 \sin^2\varphi_1)^{1/2}]$$

$$R_{TE} = [n_1 \cos\varphi_1 - i(n_1^2 \sin^2\varphi_1 - n_2^2)^{1/2}] / [n_1 \cos\varphi_1 + i(n_1^2 \sin^2\varphi_1 - n_2^2)^{1/2}]$$

$$R_{TE} = [1 - i(n_1^2 \sin^2\varphi_1 - n_2^2)^{1/2} / (n_1 \cos\varphi_1)] / [1 + i(n_1^2 \sin^2\varphi_1 - n_2^2)^{1/2} / (n_1 \cos\varphi_1)]$$

$$R_{TE} = [(1 - i \tan \Phi_{TE}) / (1 + i \tan \Phi_{TE})] = e^{-i\Phi_{TE}} / e^{+i\Phi_{TE}} = e^{-2i\Phi_{TE}}$$

where

For an overview of the effects of total internal reflection to Fresnel equations, an example is given schematically in Figure 15, where an incident light beam travels from a denser medium to a less dense one.

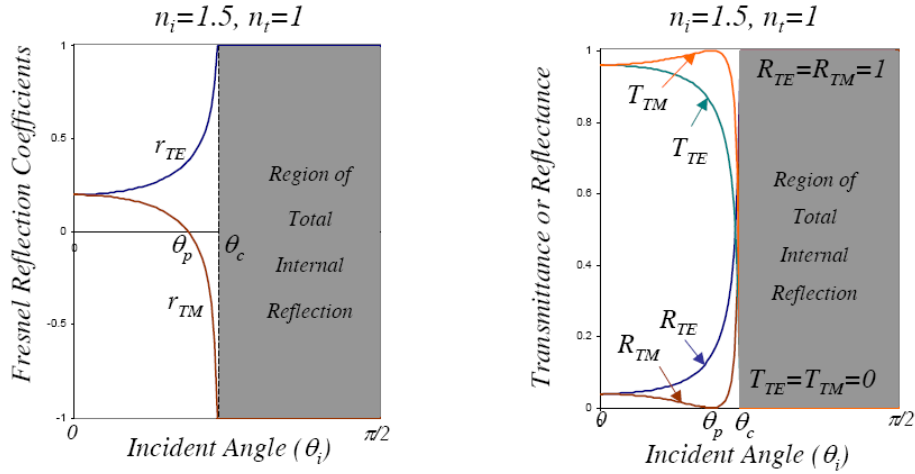


Figure 15. Example of total internal reflection at glass –air interface

In summary, in order to much the above conditions into those comprising our case, we can write the general equations expressing the phase shift in each of the waveguide interfaces as follows:

At the interface $n_2 - n_1$ ($x = W$, $n_2 > n_1$), the B_2 wave suffers a phase change of $-2\Phi_{21}$:

$$A_2' = R B_2 \Rightarrow$$

$$A_2' / B_2 = e^{-2i\Phi_{21,TE}} \equiv R$$

and

$$\tan \Phi_{21,TE} = (n_2^2 \sin^2 \theta_1 - n_1^2)^{1/2} / (n_2 \cos \theta_1) = [(n_2^2 \sin^2 \theta_1 - n_1^2) / (n_2^2 - n_2^2 \sin^2 \theta_1)]^{1/2}$$

$$\tan \Phi_{21,TM} = (n_2^2 / n_1^2) (n_2^2 \sin^2 \theta_1 - n_1^2)^{1/2} / (n_2 \cos \theta_1) = (n_2^2 / n_1^2) \tan \Phi_{21,TE} \quad (1.21)$$

At the interface $n_2 - n_3$ ($x = 0$), the A_2 wave suffers a phase change of $-2\Phi_{23}$:

$$B_2 = R A_2 \Rightarrow$$

$$B_2 / A_2 = e^{-2i\Phi_{23,TE}} \equiv R$$

and

$$\tan \Phi_{23,TE} = (n_2^2 \sin^2 \theta_1 - n_3^2)^{1/2} / (n_2 \cos \theta_1) = [(n_2^2 \sin^2 \theta_1 - n_3^2) / (n_2^2 - n_2^2 \sin^2 \theta_1)]^{1/2}$$

$$\tan \Phi_{23,TM} = (n_2^2/n_3^2) (n_2^2 \sin^2 \theta_1 - n_3^2)^{1/2} / (n_2 \cos \theta_1) = (n_2^2/n_3^2) \tan \Phi_{23,TE} \quad (1.22)$$

In this manner, we can find the phase difference after subsequent zig-zags, as follows [7]:

The phase of the A_2 wave at $z = z_c$ and $x = 0$ is

$$-\omega t + \beta z_c$$

The phase of the A_2' wave at the same point is the phase of the A_2 wave at $z = z_a$ and $x = 0$ plus that of a zig-zag. It is

$$-\omega t + \beta z_a + \beta (z_c - z_a) + 2kn_2 \cos \theta_1 W - 2\Phi_{21} - 2\Phi_{23}$$

The difference of the last two equations is $\Delta = 2m\pi$, therefore,

$$2k n_2 \cos \theta_1 W - 2\Phi_{21} - 2\Phi_{23} = 2m\pi \quad (1.23)$$

This is the equation of the modes. Since $2k n_2 \cos \theta_1 W$ is positive and both $\Phi_{21}, \Phi_{23} \leq \pi/2$, m can not be negative. The integer m may then be 0, 1, 2, 3... up to certain finite value, depending on W . This m specifies the order of the mode. The equation (1.23) stands for both polarization states.

Furthermore, it is also worth to note that in spite of the zigzag wave motion described above, the wave in the waveguide mode appears to propagate in the horizontal direction only. The vertical path of the wave motion simply forms a standing wave between the two film surfaces. Thus, in a more explicit manner, it is better to use β and u exclusively

for the phase constant and the wave velocity parallel to the film. These two last quantities are related through

$$\beta = kn_2 \sin\theta_1, \quad u = c (k/\beta) \quad (1.24)$$

The ratio β/k , which is called the *effective refractive index*, is a quantity equal to the ratio of the speed of light in vacuum to the speed of wave propagation in the waveguide in the same way as the ordinary refractive index measures the ratio of the speed of light in vacuum to that in a dense medium. For a given n_1, n_2, n_3 and m we may easily compute both β/k and W for a common θ_1 , and then according to equation (1.23), tabulate β/k and W by assigning different values for θ_1 . The curves showing W vs β/k using m as the parameter are the mode characteristics of the waveguide.

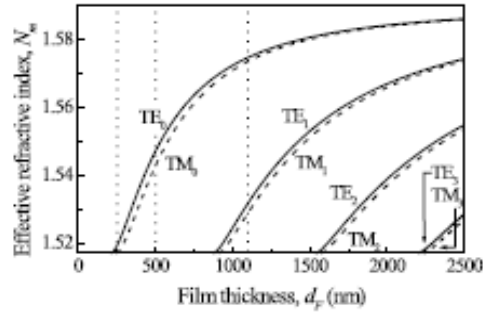


Figure 16. Effective thickness vs film thickness

As already mentioned in the previous section, the possible values for β/k in order to support waveguide modes, range from n_3 to n_2 . In the upper limit ($\beta \rightarrow kn_2$), the effective index approaches the refractive index of the film n_2 and W is large. In this case, the term $k n_2 \cos\theta_1 \rightarrow 0$, the waves propagate as plane waves parallel to the z axis and the boundaries of the film must be at $x = \pm\infty$. The film acts as a bulk medium and all the light energy is contained within the film. The fields, therefore, vanish at the two film surfaces. At the lower limit ($\beta \rightarrow kn_3$), we have $\Phi_{23} = 0$ and therefore, the thickness of the film, W , calculated from equation (1.23),

$$W_{\min} = (1/k) [m\pi + (\tan^{-1}[(n_3^2 - n_1^2) / (n_2^2 - n_3^2)])^{1/2}] / (n_2^2 - n_3^2)^{1/2} \quad (1.25)$$

is the minimum thickness, for the TE waves, required for a waveguide to support a mode of order m .

Thereby, an easy way to summarize those stated through the ray-optic method, is to consider the case of the quarter-circle shown below. Any radius represents a possible direction for the wave vector B_2 described above, and θ_1 is the incident angle measured between the wave vector and the vertical axis. The waveguide modes occur in the range of $\sin^{-1}(n_3 / n_2) < \theta_1 < \pi/2$

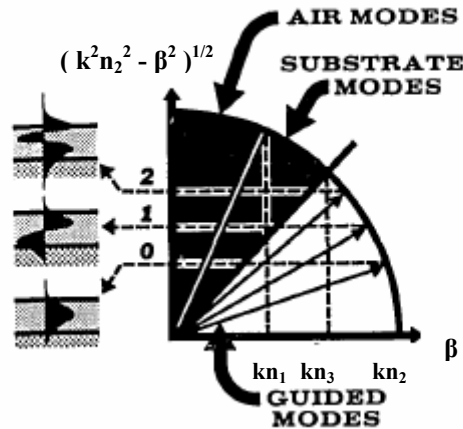


Figure 17. Discrete set of directions satisfying the equation of the modes

and occupy the white region of the circle. Within this range of θ_1 , there is a discrete set of directions which satisfies the equation of the modes (1.23). Each direction corresponds to one waveguide mode of the film and each waveguide mode has its own field distribution, as shown in the left side of the figure. The horizontal component of the wave vector, $kn_1 \sin \theta_1$, determines the wave motion parallel to the film, while its vertical component, $kn_1 \cos \theta_1$, determines the standing wave field pattern across the film. The air and substrate modes, occupying the black region of the quarter-circle, occur in the range $0 < \theta_1 < \sin^{-1}(n_3 / n_2)$. As we vary θ_1 continuously from 0 to $\sin^{-1}(n_1 / n_2)$ for the air modes and $\sin^{-1}(n_1 / n_2)$ to $\sin^{-1}(n_3 / n_2)$ for the substrate modes, the corresponding incident angle to the film and the refracted one to the substrate sweep through the entire space of the substrate and the air space.

1.4 The prism-film coupler

As it has already been stated in section 1.1, for coupling to occur, it is necessary that the components of the phase velocities of the waves in the z direction be the same in both the waveguide and the beam. Thus, a phase-match condition must be satisfied, which requires

$$\beta_m = k n_1 \sin\theta_m = (2\pi/\lambda_0) n_1 \sin\theta_m$$

However, in section 1.2 it was shown that for waveguided mode, $\beta_m > kn_1$. Combining the last two conditions leads to the result $\sin\theta_m > 1$, which is impossible.

One solution to the problem of phase matching is to use a prism, as shown in figure.

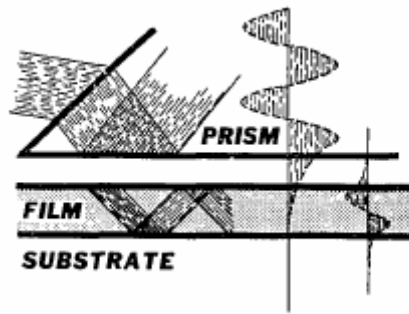


Figure 18. Evanescent fields overlap in the gap region of a prism-film coupler

A beam of light of width w is directed into the face of the prism, which has a refractive index n_p greater than n_2 , a necessary condition in order to excite all possible modes in the film. The beam is totally internally reflected at $n_p - n_1$ interface, setting up a standing wave mode in the prism that continuous into an exponential decreasing function below the base of the prism. The part of the field that extends below the prism base is called the evanescent field, since it decreases rapidly away from the prism and does not represent a free radiation. This mode is stationary in the x direction, but moves in the z direction with phase constant β_p . If we represent the incoming wave in the prism by a wave vector A_p (as shown in Figure 19), it has a magnitude kn_p and can be decomposed into an horizontal component $kn_p \sin\theta_3$ and a vertical component $kn_p \cos\theta_3$. The evanescent field below the

prism varies, therefore, as $\exp[i(kn_p \sin\theta_3 z)]$ and penetrates into the film exciting a light wave. This coupling process is called *optical tunneling*. Simultaneously, in the waveguide various guided modes can exist, moving in the z direction with phase constants β_m . All of these guided modes have an evanescent tail extending slightly beyond the n_1 - n_2 interface. If the prism spacing S is small enough, so that the tails of the waveguided modes overlap the tail of the prism mode, there is coherent coupling of energy from the prism mode to the m th waveguide mode when θ_m is chosen so that $\beta_p = \beta_m$. In other words, if the horizontal component of the wave vector A_2 or B_2 of one of

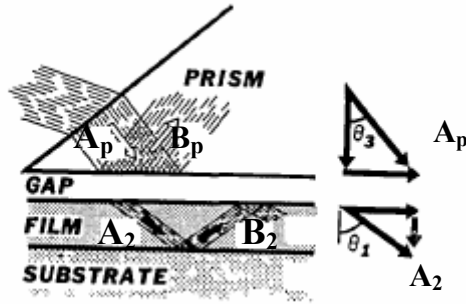


Figure 19. Coherent coupling occurs when the horizontal component of the input beam equals to the horizontal component of the wave excited in the film

the waveguide modes happens to be equal to that of the incoming light wave in the prism $kn_p \sin\theta_3$, the light wave in the prism is coupled exclusively to this waveguide mode and the laser beam is said to be in *synchronous direction*. The condition for matching of the terms is given by

$$\beta_p = \beta_m \Leftrightarrow (2\pi/\lambda_0) n_p \sin\theta_3 = (2\pi/\lambda_0) n_f \sin\theta_m \quad (1.26)$$

It is, therefore, possible to couple the light wave to any waveguide mode by simply choosing a proper direction θ_3 for the incoming laser beam. When the laser beam is in synchronous direction, the waves in the prism and in the film have the same horizontal wave motion. The fields at the two opposite sides of the air gap are in phase at every point along x. The field in the waveguide mode has an exponential tail extending upward above the film. The evanescent field of the prism is an exponential extending downward

below the prism. These two exponential tails overlap in the air gap. The parts of the fields that overlap are common to the prism and the film and constitute the coupling between them.

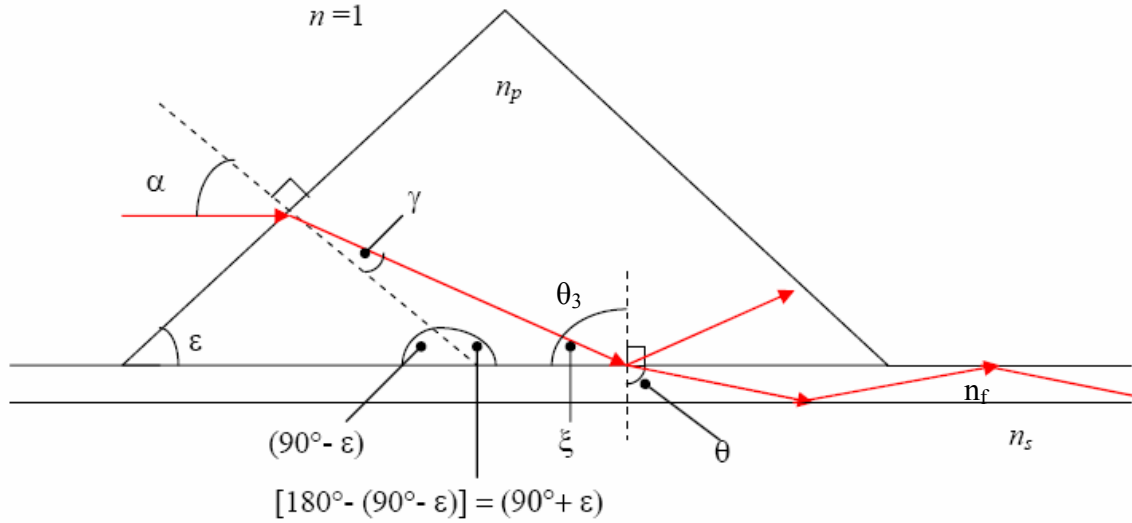


Figure 20. Prism coupling: relations between propagation angles in ambient, prism and film

The light propagation angle inside the waveguide can easily be related to the angle between the laser beam and the normal to the surface of the prism (α) [9]. The relations between the angles reported in Figure 20 are:

$$\xi = 180^\circ - (90^\circ + \epsilon) - \gamma = 90^\circ - \epsilon - \gamma$$

$$\theta_3 = 90^\circ - \xi = \epsilon + \gamma = \epsilon + \sin^{-1}(\sin \alpha / n_p)$$

and recalling Snell's law at the interfaces:

$$\text{prism-air : } \sin \gamma = (n_c / n_p) \sin \alpha$$

$$\text{prism-film: } \sin \theta = (n_p / n_f) \sin \theta_3$$

Using the above equations we can rewrite equation (1.16) as

$$\beta = k n_p \sin(\varepsilon + \gamma) \Rightarrow$$

$$\beta/k = n_p \cos[(90^\circ - \varepsilon) - \gamma] \Rightarrow$$

$$\beta/k = n_p \cos[(90^\circ - \varepsilon) - \sin^{-1}(\sin \alpha / n_p)] \quad (1.27)$$

We note that in this case the angle α is measured clockwise, that is $\alpha < 0$. If the angle α is measured towards the positive direction, then the equation (1.17) becomes

$$\beta/k = n_p \cos[(90^\circ - \varepsilon) + \sin^{-1}(\sin \alpha / n_p)] \quad (1.28)$$

1.4.1 Light-waves progression in the film

Because of the coupling described above, the energy is continuously transferred from the prism to the film along the coupling length which starts from $z = 0$ to $z = L$. The coupling of the laser beam into the film can be observed in various ways, depending on the characteristics of film and substrate and on the type of the film used. Usually coupling is observed by the appearance of a streak of guided light in the film and simultaneously, the appearance of bright or dark m-lines on the screen. The laser beam is coupled into a mode of the film. The light propagating in that mode is scattered into other directions (in the plane of the film) of the same mode and of other modes. A fraction of the scattered light is then coupled out again by the prism and produces the bright lines on the screen. Moreover, in each of these coupling situations, the reflected beam on the screen coincides with one of the m lines. Occasionally, dark m-lines can be observed on the reflected spot besides the related bright ones. They represent the scattered light of the evanescent wave leaking into the waveguide. There, the evanescent wave may subsequently be guided away from the coupling spot, or may be absorbed. If we represent as α_p and b_p the field amplitudes of the incoming and reflected waves in the prism and also as α_2 and b_2 the field amplitudes of the zig-zag waves in the waveguide mode of the film, then the wave

vectors A_2 and B_2 represent the α_2 and b_2 waves and b_2 may be considered as the reflection of the α_2 wave so that $|\alpha_2| = |b_2|$. Since the Maxwell equations are linear in field amplitudes, we expect that a_2 (or b_2) increases in x according to a_p , or that da_2/dz should be linearly proportional to a_p . On the other hand, as soon as the wave energy in the film builds up, it continuously leaks into the prism, since the energy transfer is possible in both ways between the prism and the film. We ought to expect that da_2/dz is also proportional to $(-a_2)$. We have thus,

$$da_2 / dz = Ta_3 - Sa_1 \quad (1.29)$$

where T and S are the coupling constants that depend on the geometric configuration and the refractive indices of the media. Near $z = 0$, a_2 is small and so is the term Sa_2 in equation (1.29). From $z = 0$, a_2 increases linearly according to Ta_3z . At a large z , a_2 grows to amplitude so that Sa_2 approaches a value that nearly cancels the term Ta_p in equation (1.29). Then $da_2/dz = 0$ and a_2 reaches a saturation.

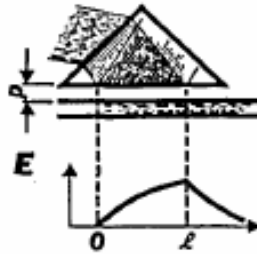


Figure 21. The light energy transferred from the prism to the film in the region $0 < z < l$ is returned to the prism in the region $z > l$. the net energy retained in the film is zero

Chapter 2

Photochromism

Photochromism is usually defined as the reversible color change observed upon UV or visible light irradiation. Photochromic materials typically undergo photoreactions that proceed by means of electronically excited states that cause changes in molecular structure or conformation, thereby altering the UV-visible absorption spectra and the index of refraction of the sample. General definitions and concepts of photochromism are stated in this chapter including photochromic systems, basic chemical photochromic processes, families of organic photochromic compounds emphasizing to the spiropyrans family

2.1 Definition of photochromism

Photo-chromic molecules are compounds that are able to exist in different isomeric forms that are very different from each other in geometry and chemical properties; they can change their form by being exposed to different wavelength illumination ranges switching from of visible [700 – 400nm] to ultra violet [>390 -200nm]. By definition, *photochromism* is a reversible transformation of a chemical species induced in one or both directions by absorption of electromagnetic radiation between two forms, A and B, having different absorption spectra. The characteristic that identifies photochromism from other photophysical processes is thermal or light induced *reversibility*. This phenomenon is often routinely understood as light-induced change of color, well known

in every-day life due to photochromic glasses that darken in the sun and recover their transparency in diffuse light.

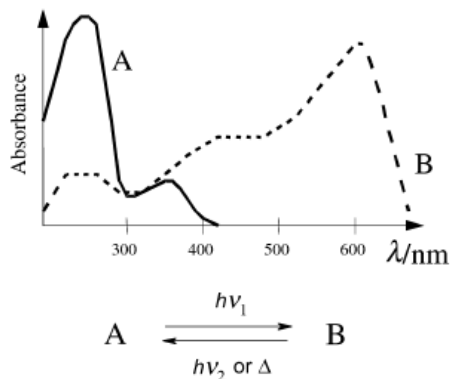
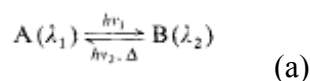


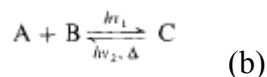
Figure 22. Photochromic reversibility

Ordinarily, the photochromic reaction involves a *reversible* transformation between two chemical species A, B: the thermodynamically form A is transformed by irradiation into form B, with B having at least one absorption band appearing at longer wavelength than those of A. In other words, the electromagnetic irradiation of the photochromic compound A causes a change in conformation or molecular structure that leads in form B. This change is reversible; the original structure can be restored by exposure to light or heat. Therefore, a photochromic system has two different molecular structures (A, B), giving rise to different absorption characteristics. A typical photochromic system can be represented by the above equation shown in Figure 22. The activating radiation generally is in the UV region (300 to 400nm) but could be in the visible one (400 to 700 nm) [16]. The reversibility is the main criterion for photochromism. The back reaction (B → A) can occur as spontaneous *thermal process* in room temperature (*Photochromism of type T*), but may also be light induced i.e. *photochemically* (thermally stable, *Photochromism of type P*).

The most prevalent organic photochromic systems are established to be *unimolecular* reactions (A → B):



Common photochromic molecules have colorless or pale yellow form A and a colored form B (red or blue). The phenomenon is referred to as *positive photochromism*. Other systems are *bimolecular*, such as those involving photocycloaddition reactions.



When $\lambda_{\max}(A) > \lambda_{\max}(B)$, *photochromism* is *negative* or *reverse*.

In this manner, photochromic systems according to equation (a) can be classified into several groups on the basis of the photochemically induced primary step [11]:

- 1) photoreversible systems, in which the colored form B undergoes a light induced reaction back to the form A
- 2) thermoreversible systems, in which the colored form B reverts thermally to A
- 3) photo- and thermoreversible systems
- 4) inverse photochromic systems, in which the initial form A absorbs at the longer wavelength and form B at the shorter wavelength
- 5) multiphotochromic systems, in which more than two forms undergo photochemical and/or thermochemical interconversion

Typical example of the unimolecular processes are encountered with *spiropyrans*, a family of molecules that are colorless or weakly colored in solid photochromic spiropyran or solutions (in ethanol, toluene, ether, ketones, esters etc). Upon UV irradiation, they become colored. The colored solutions fade *thermally* to their original state. In many cases, they can also be decolorized (bleached) by visible light. A few spiropyran display negative photochromism. They are colored in the dark and bleached by UV light. Many spiropyran are also thermochromic, and spectra of the colored forms are identical to those produced photochemically.

2.2 One-photon and two-photon systems

In general, the photochromic process involves a one-photon mechanism. B is formed from the singlet ($^1A^*$) or triplet ($^3A^*$) excited states or both. B, the photoproduct, may also be formed from an upper excited state populated by absorption of two photons.

In the case of two photon photochromism, electron excitations need absorbance of two-photon energy. The transition probability to populate the final state (hence to obtain the photoproduct) depends on the product of the photon irradiances $E_{p(1)}$ and $E_{p(2)}$ of the two exciting beams. Two absorption processes may be distinguished [12]:

- a) stepwise (or sequential) two-photon absorption where the second photon absorption takes place from a real level.
- b) simultaneous absorption of two photons via a virtual level

The former relies on the existence of a real intermediate state, from which an excited population is further pumped to a higher energy level by absorbing photons of the same energy as the ground state (excited state absorption). Compared to simultaneous TPA, stepwise TPA does not require coherence of the incident light, and may be treated as two sequential single photon absorption process. The excitation efficiency can be high enough to provide intense up-conversion fluorescence, which is one of the important mechanisms of IR sensor cards.

The simultaneous TPA, most generally referred to TPA, is a quantum mechanical three body process, where electron absorbs two photons simultaneously to transcend the energy gap in one excitation event [13]. An intuitive physical scenario is, as light passes through a molecule, a virtual state is formed when the first photon is absorbed. It persists for a very short duration (of the order of several femtoseconds as prescribed by Heisenberg's Uncertainty Principle), which contrasts with the long lifetime of the actual intermediate energy level in stepwise absorption. TPA can result if the second photon arrives before the decay of this virtual state. If the energy of the two photons is identical, the process is referred to as degenerate TPA, otherwise the process is a non – degenerate one.

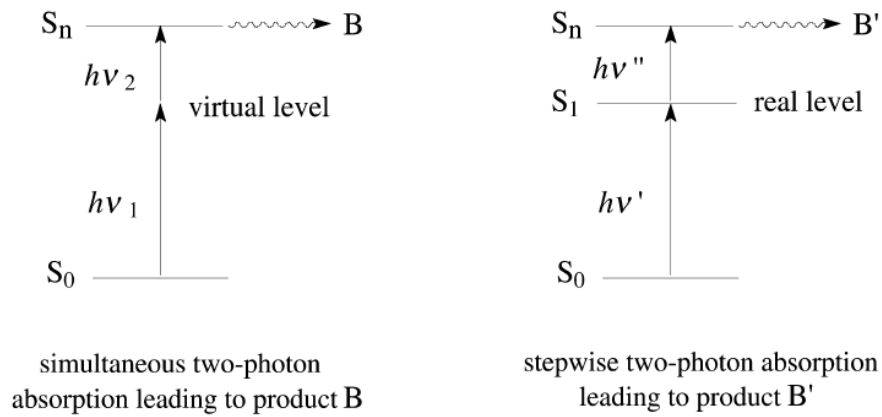


Figure 23: Simultaneous and Stepwise two-photon absorption

The excitation process can also proceed through a metastable intermediate (process b). The derivative A isomerizes to the form B via an intermediate X (not isolated). The reverse reaction B \rightarrow A proceeds at different wavelength ($h\nu_2$)

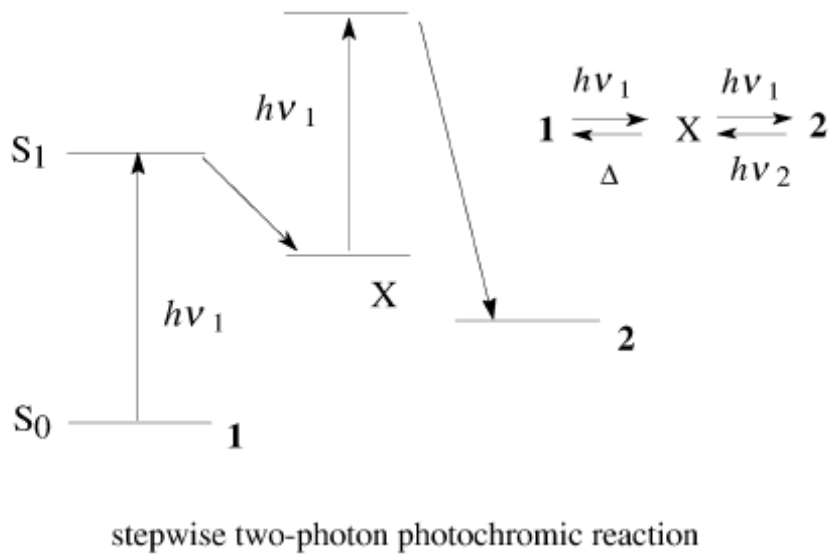


Figure 24: Stepwise two-photon absorption through a metastable intermediate

2.3 Common photochromic systems

Photochromic systems can be classified into six major groups according to reaction types (molecular transitions) responsible for the reversible color change. They are briefly stated below [11]:

I) Triplet –Triplet Absorption

The simplest photochromic system is one which contains molecules in the stable ground state and in a metastable, photochemically excited state.

II) *cis* – *trans* Isomerization of double bonds (e.g. stilbenes, azo compounds, polymethines)

When the double bond of several photochromic compounds are excited either directly or via special sensitizers, a reversible *cis-trans* isomerization is observed involving a 180° rotation around a carbon – carbon double bond. The two configurational isomers usually differ in the positions and intensities of their UV absorption maxima. For example, the absorption of photons results in the conversion of 11-*cis* retinal ($\lambda_{\text{max}} = 498\text{nm}$), bound as a Schiff base via the amino acid lysine to the protein opsin together forming rhodopsin, to 11-*trans* retinal ($\lambda_{\text{max}} = 380\text{nm}$)

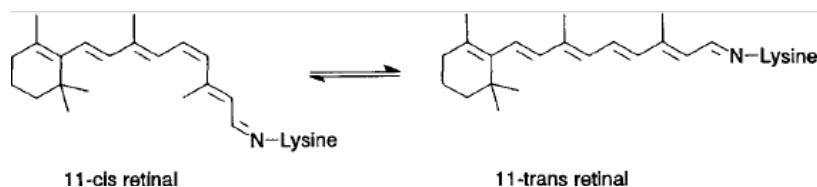


Figure 25: Cis-Trans isomerization of 11-cis retinal

The structural disturbance induced by the *cis-trans* isomerization of the retinal moiety of rhodopsin leads to conformational change of the whole protein molecule and, via a

cascade of reactions, this eventually creates a nerve pulse responsible for the visual process.

III) *Pericyclic Reactions* (e.g. spiropyrans, spirooxazines, fulgides etc)

Of the different classes of pericyclic reactions, the electrocyclic reactions have proved to be especially suitable as basis for photochromic systems. The following scheme shows three different types of ring-opening reactions.

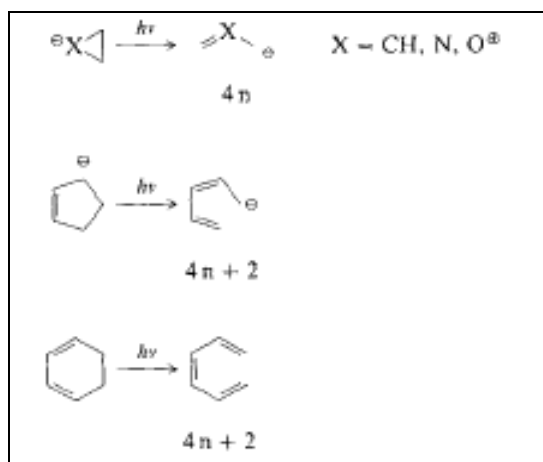
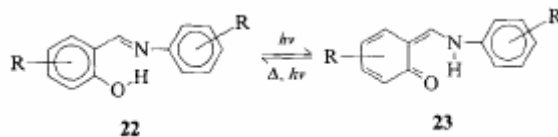


Figure 26: Pericyclic reactions

IV) *Tautomerization (Hydrogen transfer)*

Photochromic tautomerism is the shifting of the equilibrium of two tautomeric forms by the action of electromagnetic radiation. Light induced tautomerizations can occur in the form of phototropic rearrangements which include hydrogen transfer (such as those shown in the scheme below) and valence tautomerism, where bonds are rearranged causing an alternation in valences of one or more atoms. Such prototropic processes may be either thermally or photochemically activated and are responsible for the observed photochromism.



R can be any group, e.g. aryl, methyl.

Figure 27: Tautomerism

V) (Photo) *Dissociation* (e.g. triarylmethanes)

a) *Heterolytic Cleavage of Bonds*

Heterolytic cleavage is the term applied if a single bond is cleaved, leaving charged species that exists as individual ions or as moieties still connected by other bonds. In this manner, irradiation of the colorless form gives the strongly colored cations, with release of an Anion A^- . These charged species are rarely stable and quickly revert back to their original state. The thermally induced decoloration of the cation depends critically on the solvent and the anion concentration

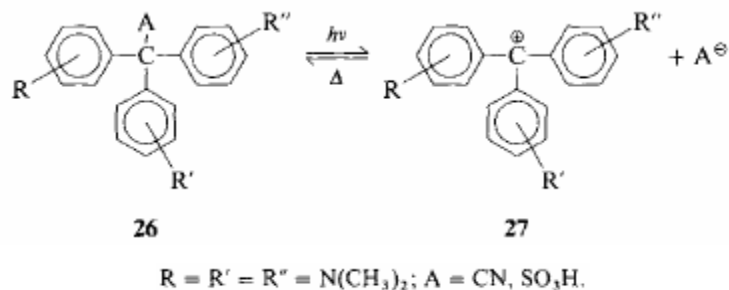


Figure 28: Heterolytic Cleavage

a) *Homolytic cleavage of bonds*

Homolytic cleavage is similar, except that on exposure to light cleavage reactions yield colored free radicals

VI) Electron Transfer/ Redox Photochromism

The formation of colored radical cations (and accompanying radical anions)

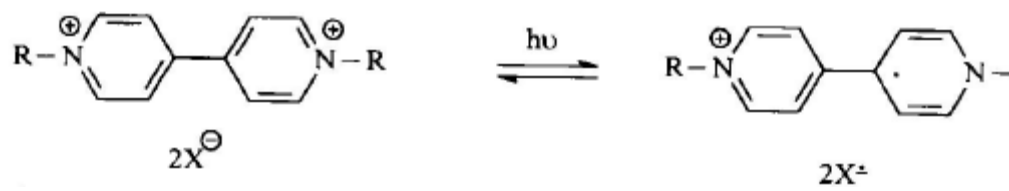
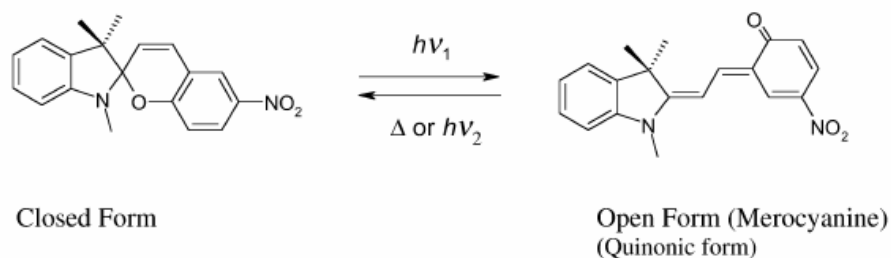


Figure 29: Electron Transfer

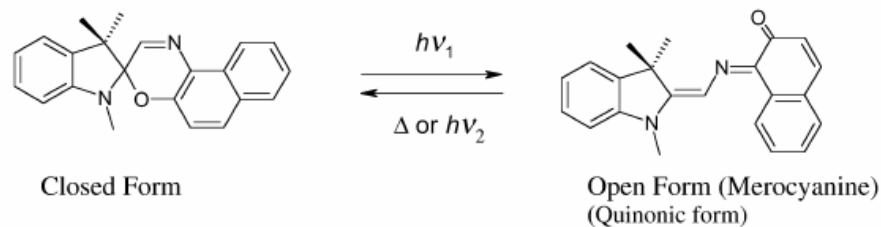
2.4 Families of organic photochromic compounds

Several classes of photochromes A have been described. These classes may be differentiated according to the chemical transformation upon which the phenomenon of reversible color change is based. In all cases stated below $h\nu_2 < h\nu_1$ [12].

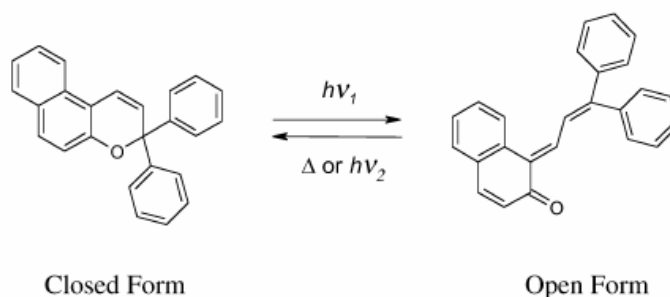
IV.1 Spiropyrans



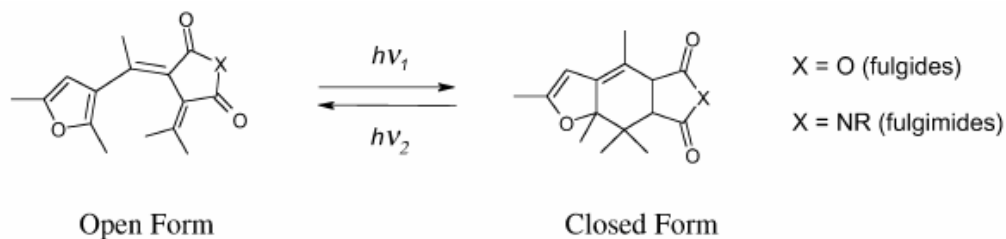
IV.2 Spirooxazines



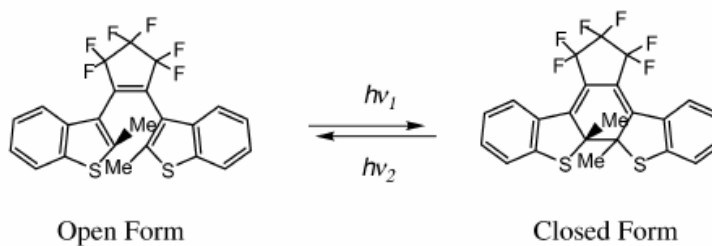
V.3 Chromenes



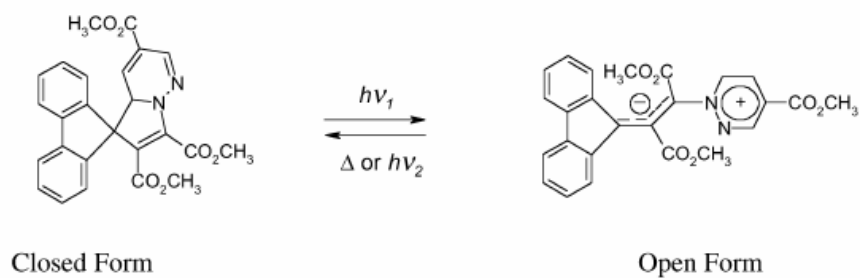
IV.4 Fulgides and fulgimides



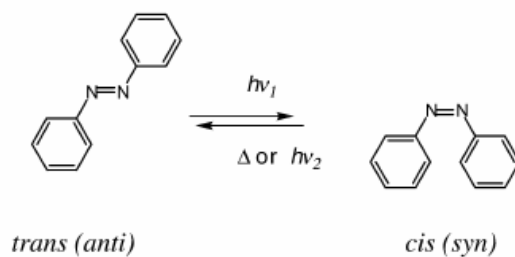
IV.5 Diarylethenes and related compounds



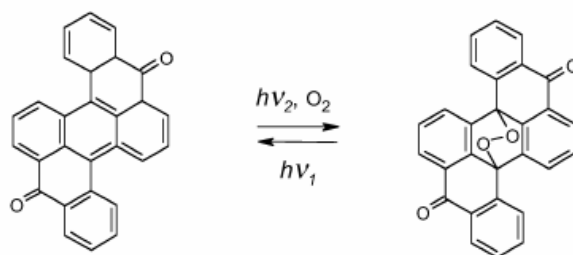
IV.6 Spirodihydroindolizines

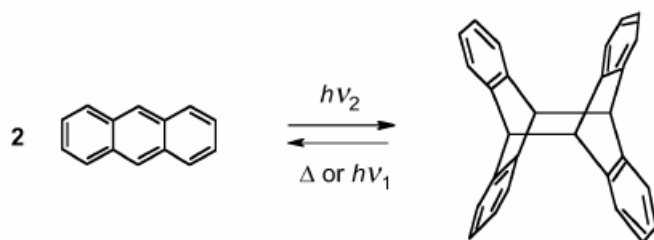


IV.7 Azo compounds

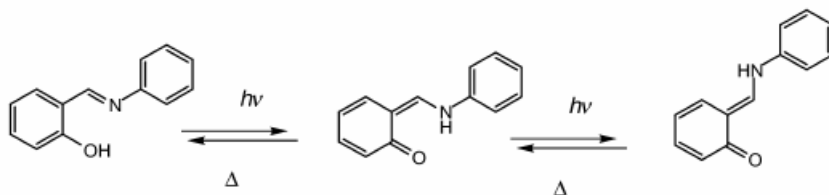


IV.8 Polycyclic aromatic compounds

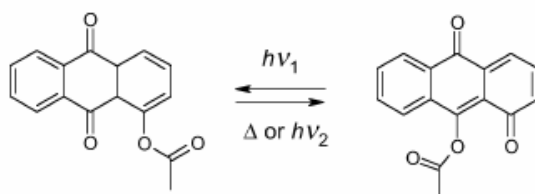




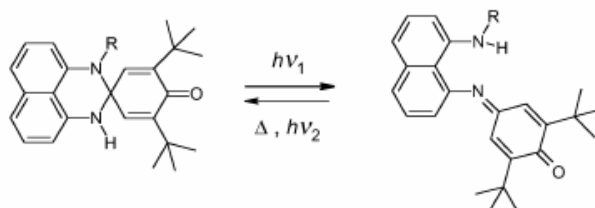
IV.9 Anils and related compounds (hydrogen transfer)



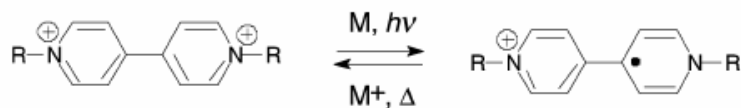
IV.10 Polycyclic quinones (periaryloxyquinones)



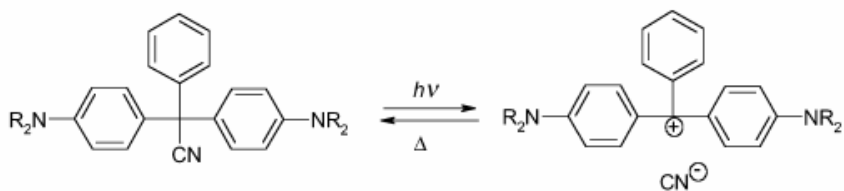
IV.11. Perimidinespirocyclohexadienones



IV.12 Viologens



IV.13 Triarylmethanes



2.4.1 Spiropyran (NO₂-BIPS)

Spiro-compounds are an important category of photochromic molecules as they induce excellent coloration when irradiated. In addition, flexibility of their synthesis can yield a wide variety of colors. Spiropyrans (and spirooxazines) can be defined as materials in which a heterocyclic and a chromene moiety are orthogonally linked through a spiro-carbon (C_{spiro}) atom. This family refers, in general, to a (substituted) 2 H-pyran having a second ring system, usually (but not necessarily) heterocyclic, attached to the 2-carbon atom of the pyran in a spiro manner [14], as shown in structure below, i.e. a carbon atom is common to both rings.

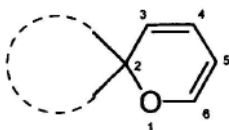


Figure 30. Spiro- carbon structure

In the present project, we will examine the case of a spiropyran family in which the pyran ring carries a nitro group at the 6-position of the moiety known as nitro – spiropyran SP_{NO₂} (or nitro BIPS, where BIPS refers to 1', 3', 3'-trimethylspiro-[2H-1-benzopyran-2, 2'-indoline])

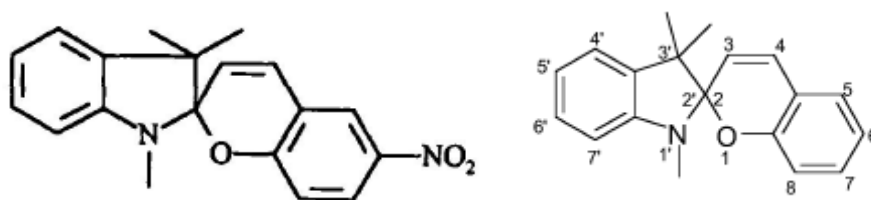


Figure 31. Nitro-BIPS form of spiropyran

The photochromic behavior of spiroyrans is based on the reversibility between the closed, colorless spiropyran form and the colored “open” merocyanine dye as shown in Figure 32. In their original state, the spiropyran molecules are bicyclic compounds with one and only one atom that is common to both rings. The photochromic spiropyran molecules are composed of two π -electron moieties that are oriented orthogonal to each

other. The configuration of the compound means that each part exhibits its own absorption spectra rather than that of a conjugated system, since the π – electron do not

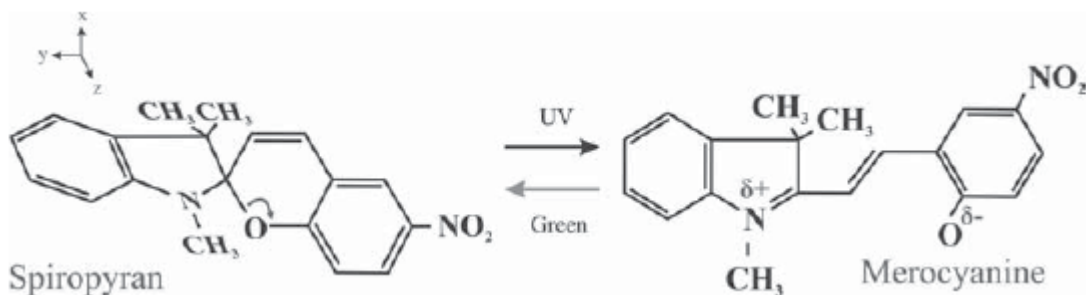


Figure 32. Closed spiropyran form and open merocyanine form

interact with one another, therefore, the absorption spectrum is a sum of the spectra for the two parts of the molecule. However, when irradiated with ultra-violet light, there is heterocyclic cleavage of the spiro – carbon oxygen (C-O) bond leading to the formation of the open chain compounds and a subsequent electrocyclic ($4n + 2$) reaction ($n=1$) takes place. This is followed by a rotation of the two moieties in the molecule resulting in the formation of a planar colored form. The colored form is highly conjugated structure referred to as the merocyanine or open form. The merocyanine itself is an equilibrium mixture of geometrical conformations, and its electronic distribution varies from highly zwitterionic to an essentially nonionic ortho-quinoidal structure.

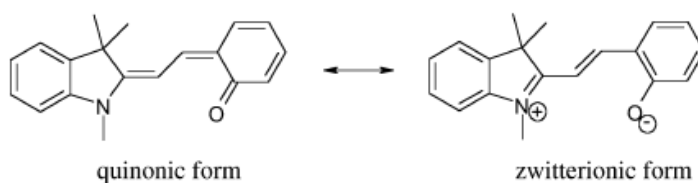


Figure 33. Quinonic and zwitterionic form of merocyanine

The closed form of spiropyran (SP) has an absorption band situated in the UV region (between 320 and 400 nm) and is thus colorless. The merocyanine form has a characteristic absorption band in the visible region (red shift in the absorption spectrum from the UV to the 500-600 nm bands) due to the extended conjugation of the fully

delocalized π - electron system accompanying the ring opening. The π -electron system is now extended throughout the molecule, since the absorption of a single photon leads to the formation of a single bond instead of the double one and the molecule is freely to rotate around it [18, 21]. The cis-isomer tends to rotate and to give the trans-isomer which is more stable. The conversion cis \rightarrow trans is thermal where the excited π^* electron returns back to the conjugated π system and the single bond becomes a double once again. Irradiation with visible light induces back conversion to the closed colorless form. The open photo-merocyanine form is thermodynamically unstable, thus, the bleaching process can also take place thermally in the dark.

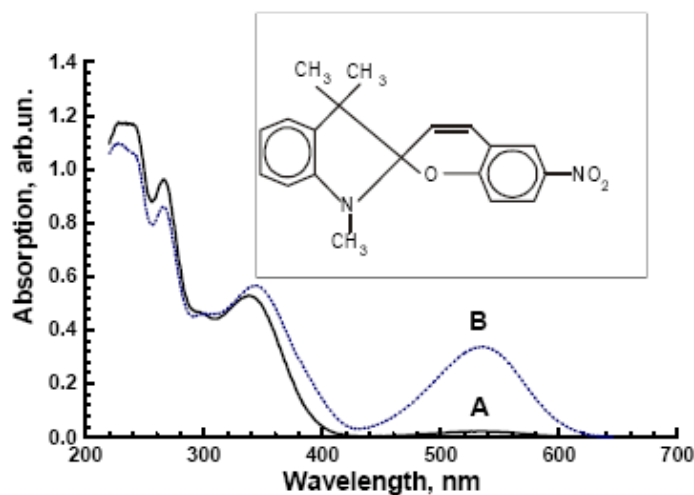


Figure 34. Absorption spectra of (A) closed spiropyran and (B) open merocyanine form

In the ground state of a molecule, electrons are predominantly in the lowest electronic state. Following excitation with electromagnetic radiation they promote to higher energy levels or excited states. The molecules subsequently relax back to the ground state by radiative pathways such as fluorescence or phosphorescence or by nonradiative pathways such as energy transfer to the solvent or other molecules. When a molecule is photochromic it can also use the absorbed energy to change conformation. The path of deactivation the molecule takes depends on kinetics. Therefore, for photochromism to occur, the switch from state A to B must be quicker than the other deactivation pathways [15].

To understand the mechanism of deactivation, quantum yields can be very useful. The quantum yield of deactivation pathway is determined by the fraction of photons, which deactivate, using that pathway, out of the total photons absorbed. The quantum yield increases when the pathway is more effective. High efficiency of the photocoloration reaction is important as it governs the depth of colorability.

The specificity of the photoprocess for a particular indoline merocyanine may be caused by the existence of several *trans* and *cis* isomers which convert sequentially into the most stable one. There are eight possible isomers of the open merocyanine structure, however, only four represent a local energy minimum and are therefore stable isomers. The stable merocyanine isomers are depicted in the above picture, where the first C or T refers to the first double bond in the centre of the molecule starting on the indole side, the second to the next single bond that can rotate to produce different structures and the third to the second double bond.

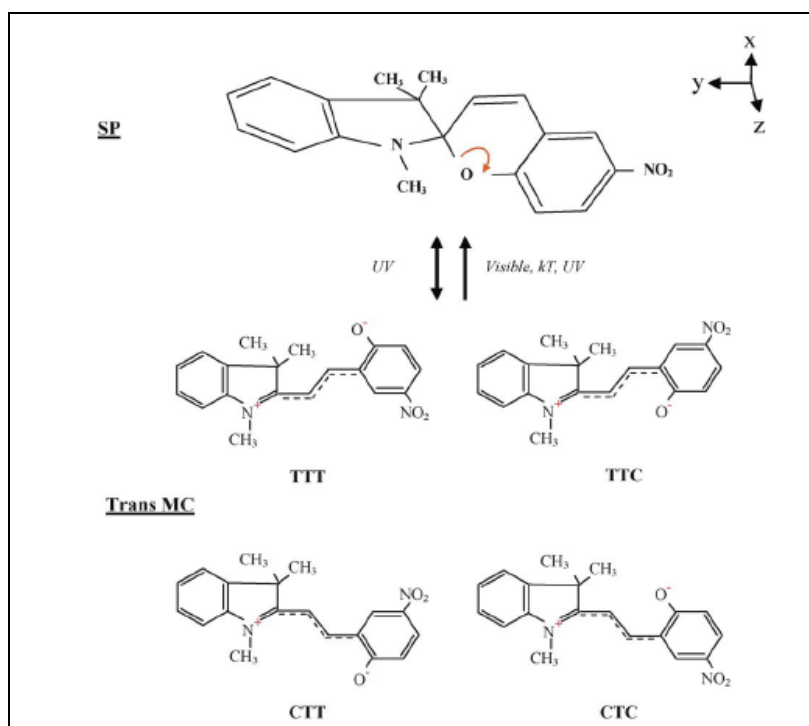


Figure 36: The four stable isomers of merocyanine

According to reference [17], of the four conformers, the most stable is the TTT, the next CTT and the most unstable is the CTC. By calculating the energy profiles of the isomerization processes, as shown in the figure below, it is concluded that (a) the TTT \leftrightarrow TTC process is allowed from both directions (b) the TTT \leftrightarrow CTT process is prohibited due to discontinuities in the potential energy surface (c) the TTC \leftrightarrow CTC is also allowed from both directions.

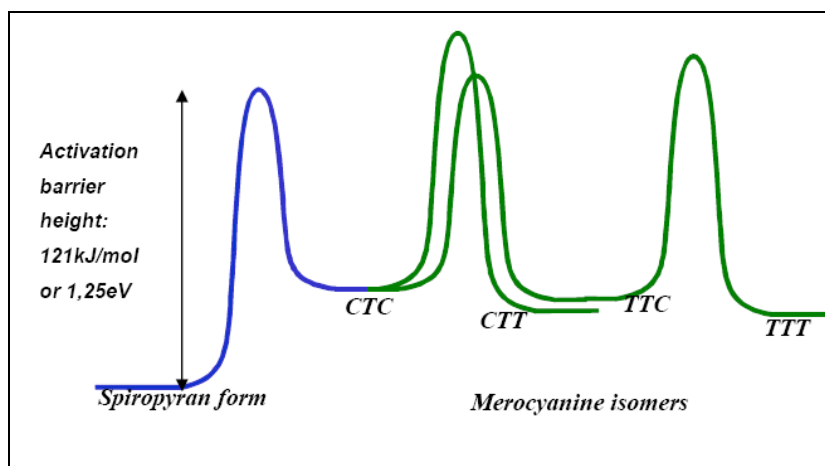


Figure 37: Potential energy surface of merocyanine's isomers

Cyclization from the CTC conformation satisfies the minimum requirement. In all cases, the potential energy curves showed a discontinuity. The discontinuities indicate that direct single step conversion from TTC, CTT or TTT conformers to the spiro-form isomer is prohibited. Careful examination of the potential energy curves reveals that the discontinuities are due to channel routes to other conformations, namely from TTC to CTC and from CTT to CTC. In the case of the TTT conformer, two conformational changes from TTT to TTC and TTC to CTC are involved.

Of the four conformers of the merocyanine-form isomers, only the CTC conformer was found to cyclize thermally through an appropriate reaction path. Isomerization from TTC to CTC is necessary for the TTC form to cyclize to the spiro form isomer. Two routes are possible for the isomerization process from TTT to CTC. One is via TTC and the other is via CTT. The route via CTT is prohibited.

The fact that only the TTC form has been observed as a merocyanine-form isomer by NMR can be interpreted as follows. Although the TTT conformer has the lowest energy, the large barrier from the TTC to the TTT conformer suppresses population of the TTT conformer. Therefore, the TTT conformer is not detected. The CTT conformer is more stable than the TTC conformer, but the population is less than that of the TTC conformer. This is due to the large energy barrier from the CTC to the CTT conformer. The photogenerated CTC conformer mostly converts to the more stable TTC conformer and other conformers, CTT and TTT, are not populated. This is the reason why the TTC conformer is the dominant merocyanine form isomer. The thermal cyclization of the TTC conformer is considered to proceed via the CTC conformer.

An insight into the mechanism of photochromism of the 6'-nitro-BIPS is given by Helmut Gerner et al [19] after performing microsecond and nanosecond laser flash techniques. It was shown that the triplet excited state of the closed spiropyran ^3SP leads to the open cisoid isomer in the triple excited state ^3X . The latter species then reacts with open transoid form MC in a bimolecular reaction to form the dimmers (maximizing at 630 nm). Moreover, the closed form SP leads directly to MC since the rise time of MC is affected by oxygen (from 10 ns in nitrogen to 22 ns in oxygen) [19].

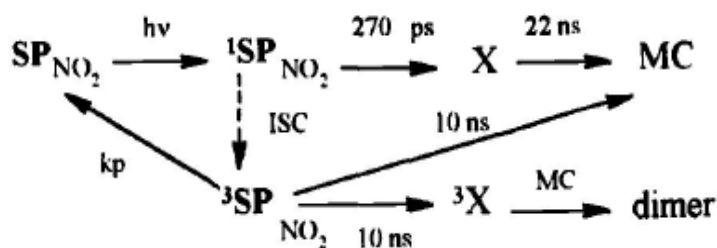


Figure 37: Potential energy surface of merocyanine's isomers

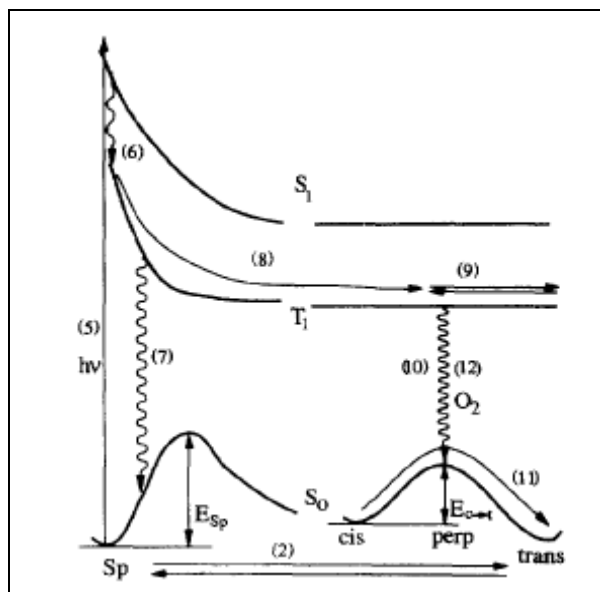


Figure 38: Potential energy surface of merocyanine's isomers

Important disadvantages of this type of molecule in reversible switching process are: low thermal stability of the colored form (ranging from a few seconds to several hours at room temperature), photochemical side reactions (degradation) [20] and the occurrence of thermochromic behavior, which might interfere with the photochromic process. Besides temperature, concentration and solvent effects, the photochemical, as well as, thermal behavior of organic photochromic molecules is influenced in various ways by the characteristics of the surrounding polymeric media.

Effects of polymer matrices are closely coupled with the regulation of photochromic reactions and with the emergence of novel photoinduced properties other than color changes, leading to a dual meaning of matrix effect [16]: the effect of *the matrix on photochromism* and the effect of *photochromism on the matrix*. In the former case, the rate of photochromism and photoinduced optical property alterations are markedly affected by polymer matrices, in particular when photochromic molecules are embedded in polymer solids. The latter case involves the reversible changes in the properties of polymer materials triggered by photochromic reactions. The purpose of the present project is related to the latter case, where we will examine the photoinduced changes in the refractive index of the polymer PEMMA doped with the photochromic spirocyan

2.5 Fatigue

Photochromism is a nondestructive process, but side reactions can occur. The loss of performance over time, due to chemical degradation of a material, is termed “fatigue” [12]. Usually the major cause of damage to photochromic substances is oxidation.

Spiropyrans, especially the nitro- substituted ones, present a short life *cycle* because of the extensive thermal and photochemical decomposition that they undergo by repeated and/or continuous light exposure. In a *cycle*, a system A is transformed (photochemically) into a system B which returns to A (thermally or photochemically); the terms “switch on” and “switch off” are used. Photodegradation of nitro-substituted SPs originates from the reaction of the cis-cisoid X isomer with solvent or impurities [16]. The lifetime of the X isomer determines the extent of the

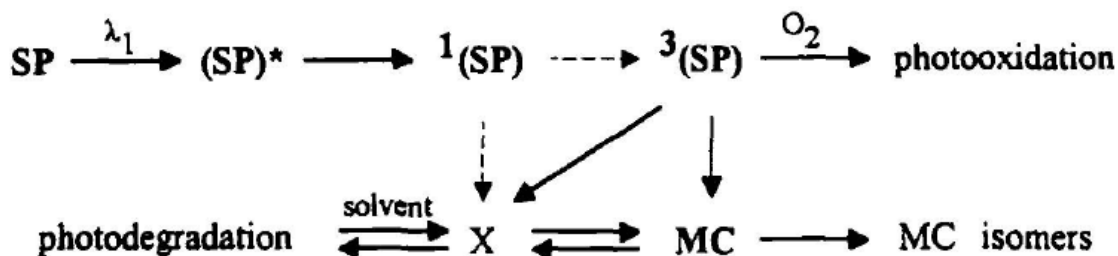


Figure 39. Photodegradation of spiropyrans

SP degradation. Conversely, photooxidation is the result of the triplet state of the closed SP form with oxygen. The two processes are initiated by the same step, i.e. cleavage of the $\text{C}_{\text{spiro}} - \text{O}$ bond. It is likely that the merocyanine form of the spirobenzopyrans would

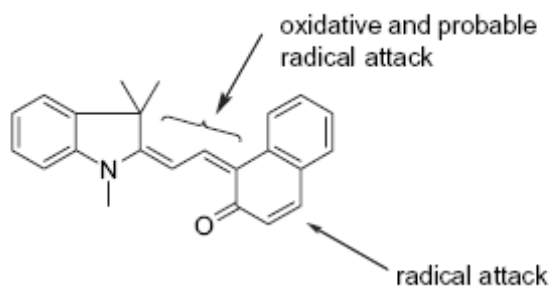


Figure 40. Photodegradation of spiropyrans: radical attack both C5' = C6' bond

be susceptible to radical attack on both C5' = C6' bond. The fatigue mechanism occurs predominantly as a pathway in competition with the isomerization of the initial ring-opened cis – cisoid merocyanine form to the final TTC merocyanine form [15, 22].

Chapter 3

Sol-Gel process

Sol-gel technology is a powerful tool for the fabrication of organic and inorganic-organic hybrid materials. The advantages of the ease of preparation, modification and processing of the materials along with their high optical quality, photochemical and electrochemical inertness and good mechanical and chemical stability have established this method among other available techniques. The process is based on the phase transformation of a sol obtained from metallic alkoxides or organometallic precursors. This sol, which is a solution containing particles in suspension, is polymerized at low temperature to form a wet gel. This one is going to be densified through a thermal annealing to give an inorganic product like glass, polycrystals or a dry gel. By using this method inorganic-organic hybrid materials offer properties better than those prepared alone. Many configurations such as monoliths, fibers, thin and thick films can be achieved in the process of fabrication. Sol-gel materials have been applied in many fields, such as membranes, chemical sensors and catalysis.

The term sol-gel originates from the individual terms of sol and gel. A sol is a suspension of solid particles in a liquid. The size of the dispersed phase (solid particles) is very small (between 1 – 1000nm) and thus gravitational forces are negligible and interaction is dominated by short – range forces like Van de Waals attraction and surface charges. The small solid particles are typically metal oxides or metal alkoxides and they are also called precursors in the sol-gel process. The precursors of the sol undergo polymerization which leads to the growth of clusters that finally collide and link together into a gel.

A sol-gel process usually involves catalytic hydrolysis of sol-gel precursor(s) and catalytic polycondensation of the hydrolyzed products and other sol-gel-active components present in the reaction medium to form a macromolecular network structure of sol gel materials. Any sol-gel material is formed through 4 steps [23]. The first one is hydrolysis and condensation in which precursors or monomers such as metal oxides or metal alkoxides are mixed with water and then undergo hydrolysis and condensation to form a porous interconnected cluster structure. An alcohol is chosen as a solvent for the precursors since they are often insoluble in water. Either an acid such as HCL or a base like NH₃ can be employed as a catalyst.

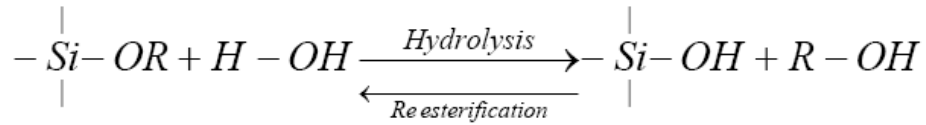


Figure 41. Hydrolysis process

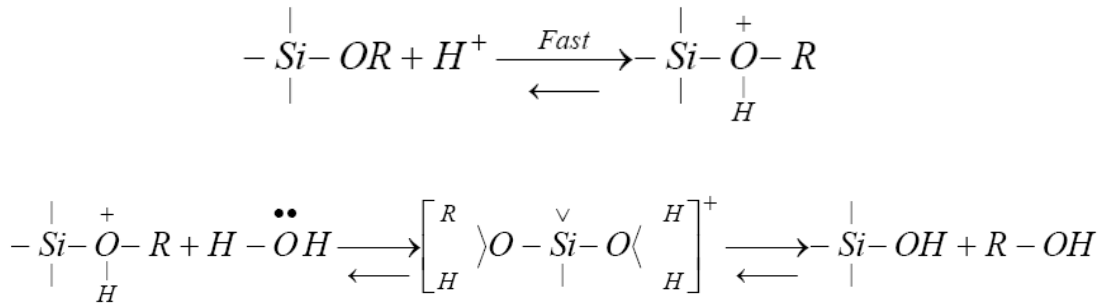


Figure 42. The acid - catalyzed mechanism

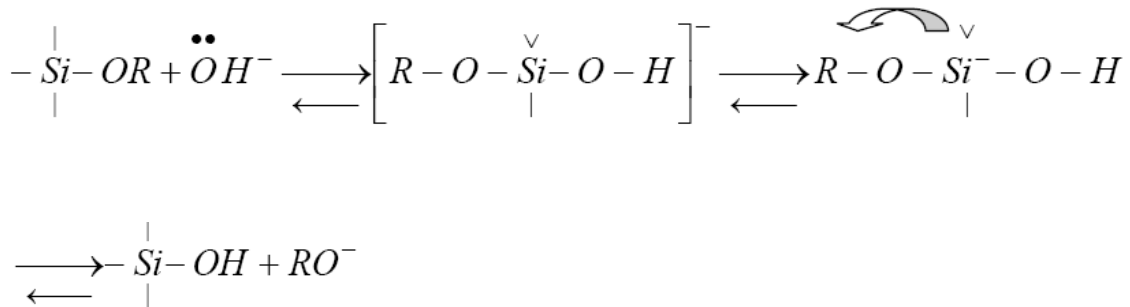


Figure 43. The base - catalyzed mechanism

The second step is gelation. As the first step of hydrolysis and condensation continues, more particles join the clusters. The clusters grow bigger and bigger and they collide each other and link together to generate a single giant spanning cluster which is called gel. With time, more clusters present in the sol phase will become connected to the network and the gel will become stiffer and an increase in viscosity and elasticity will result in. In addition, hydrolysis and condensation so do not stop with gelation. They continue to pass gelation and go to the next step of sol-gel process.

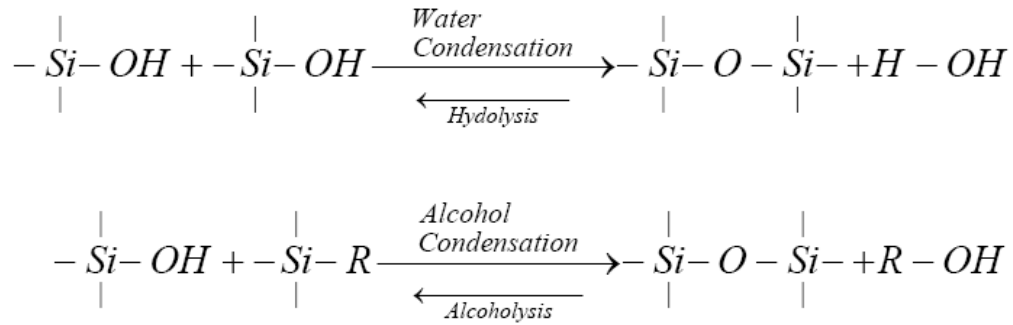


Figure 43. Gelation

Aging is the third step of the sol-gel process. During aging, the process of change after gelation can be divided into polymerization, coarsening and phase transformation. Because of presence of the unreacted hydrolysis groups, condensation reactions continue, resulting in the increase in connectivity of the network and thus the increase in stiffness and strength of the gel. As the continuing condensation process go on the pores of the gel will become smaller and liquid in the pores will be expelled, leading to gel shrinkage or syneresis. Another change on the process of aging is coarsening, also called ripening. This process involves dissolution and reprecipitation which is driven by differences in solubility between surfaces with different radii of curvature. The smaller particles, which have positive radii of curvature and higher stability, dissolve again and precipitate into crevices and necks between particles, which have negative radii and lower solubility allowing material to accumulate there. This serves to increase pore size, by filling in smaller pores, and strengthen the network. In addition, phase transformation may take

place during aging, such as crystallization from amorphous structure, segregation of a liquid phase into two or more phases.

Drying is the last step of the sol-gel process. It can be divided into three stages. In the first stage, due to evaporation of the liquid in the pores, the gel shrinks. The gel network experiences deformation thanks to capillary forces. New connections in the network are also formed and continue to strengthen the network. The liquid vapor interface remains at the external surface of the gel. Shrinkage continues until stage two starts. The second stage starts when the gel becomes too stiff to shrink and reaches the critical point in which the capillary forces are the highest and pores begin to empty the liquid in them. At this point, liquid evaporation from pores is slowing down. The liquid recedes into the interior, leaving air-filled pores near the surface. Finally, once the liquid is primarily out of pores, the liquid is isolated into pockets. Evaporating within the gel body and diffusing the vapor to the exterior is the only way for remaining liquid. No further shrinkage occurs. Loss of weight is the only significant change until equilibrium is reached with the environment.

Chapter 4

Methodology

In this chapter we will get through a detail description of the methodology followed in order to measure the refractive index of thin films according to theory already stated in previous sections. The number of independent parameters associated with the characterization of thin film optical waveguides can be reduced by the introduction of appropriately normalized parameters and associated scaling rules, which allows the creation of plots from which effective guide index and effective guide thickness can be determined.

4.1 Measurement of the refractive index and the thickness of a thin film

The effective guide index $N = \beta / k$ and the effective guide thickness can be determined for any slab-guide configuration by the introduction of appropriately normalized parameters and associated scaling rules, so that the number of independent parameters to be reduced. One of the basic guide parameter to use is the normalized frequency or film thickness V , defined as [24]:

$$V = k f (n_f^2 - n_s^2)^{1/2} \quad (3.1)$$

A second basic parameter to introduce is that for the index asymmetry of the waveguide structure, a , where

$$a = (n_s^2 - n_c^2) / (n_f^2 - n_s^2) \quad (3.2)$$

This measure is defined in a somewhat different way for the TE and the TM modes, and its values can range from zero for perfect symmetry ($a = 0$ if $n_s = n_c$) to infinity for strong asymmetry ($a \rightarrow \infty$ if $n_s \neq n_c$ and $n_s \rightarrow n_f$).

We consider, in our case, asymmetric slab waveguides where the propagation constant β of the guide and the related effective refractive index are determined by the dispersion relation (1.23) rewritten as

$$\kappa f = m\pi + \Phi_s + \Phi_c, \quad m = 0, 1, 2 \dots \quad (3.3)$$

which is the basis for our discussion. Here m is the mode number, Φ_s and Φ_c are the phase shifts associated with total internal reflection from the film-substrate and film-cover interfaces, f is the film thickness and κ is the transverse propagation constant given by

$$\kappa^2 = k^2 (n_f^2 - N^2) \quad (3.4)$$

To determine the phase shifts and the effective guide width we also need the decay constants γ_s and γ_c in substrate and cover, which are given by

$$\gamma_s^2 = k^2(N^2 - n_s^2) \quad (3.5)$$

$$\gamma_c^2 = k^2(N^2 - n_c^2) \quad (3.6)$$

It is also convenient to use a parameter b which is called the normalized guide index defined by

$$b = (N^2 - n_s^2) / (n_f^2 - n_s^2) \quad (3.7)$$

$$N^2 = n_s^2 + b (n_f^2 - n_s^2)$$

Assuming that $n_s \geq n_c$ this normalized index takes on values between zero and unity. At the cutoff of the guide we have $N = n_f$ and $b = 1$. In the case of TE modes, the formulas for the phase shifts Φ_s and Φ_c are

$$\tan \Phi_s = \gamma_s / \kappa \quad (3.8)$$

$$\tan \Phi_c = \gamma_c / \kappa \quad (3.9)$$

We use these formulas together with equations (3.4) – (3.6) and the definitions for V and b , to rewrite the dispersion relation in the normalized form

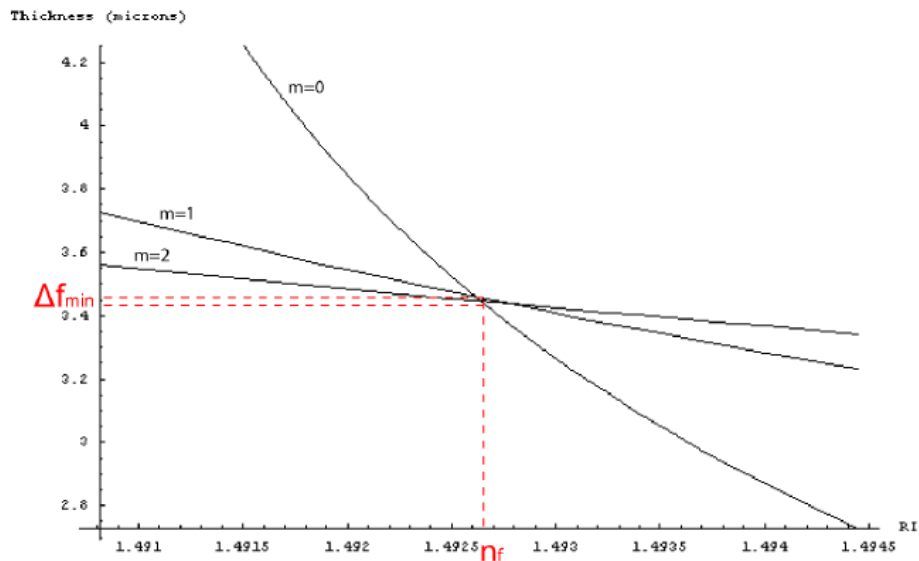
$$V (1-b) = m\pi + \tan^{-1} [b / (1-b)]^{1/2} + \tan^{-1} [(b + a) / (1-b)]^{1/2} \quad (3.10)$$

This form indicates that the guide index $b = (V, a)$ depends on only two independent parameters: the normalized thickness V and the asymmetry measure a .

A program named *SLABv3.m* written in Mathematica code, included in Appendix A, serves for the calculation of the thickness and the refractive index of our thin film. A briefly notation will be given below in order to state the main idea of the algorithm written and the way that it is related to those stated in theory. For convenience, we consider the case of TE modes.

Therefore, for each incident synchronous angle of the light beam at the prism entrance face, the program calculates through the relation (1.28) (the function *betaF* in the code) the effective refractive index related to each excited mode. According to the above formulation and using the values for each effective refractive index, we get for each mode, through equation (3.10), a value for the effective thickness V , and thus a value for the thickness f of the film using equation (3.1) (the function *te* in the code). However, since in equation (3.1) the refractive index of the film (n_f) is an unknown parameter, the code is programmed to run within a range of possible values for the n_f in the region of the

value previously obtained for the 0th order effective index (function teModes). In accordance to this, a range of values for the thickness of the film is obtained for each mode. The variance of the several $f_{m,i}$ is then calculated and minimized afterwards in order to find the minimum difference between the f_m obtained [25]. Next, the minimum variation is applied to the effective index of the 0th order, thus a value for the film index is approximated. A diagram of the thickness versus the refractive index is plotted afterwards for each mode, where each curve represents the dispersion of the thickness for a range of values n_f near the region of the film refractive index calculated previously. The desired solution (n , thickness) corresponds in principle to the point of intersection of the curves associated with each mode [26]. The value for the thickness given in the end is calculated by the *Mean* of the various f_i obtained for each mode. In this manner, the output of the program we get after executing the code has the form shown below. Note that the mode with the largest angle α of incidence has the lowest mode number.



$$\text{Thickness} = 2.46723 \times 10^{-6}$$

$$\text{Refractive index} = 1.49266$$

In order to get a fine approximation of our film's refractive index, at least three modes need to be supported by our waveguide. Minimum two are needed in order to make an

intersection point for the two unknown parameters Thickness – Refractive Index and the third one to validate the minimum variance between them. The red colored values introduced in the output plot, indicate the region of minimum variance.

4.2 Determination of thin film thickness using reflectance spectroscopy (number of modes expected)

Generally, the electronic excitation occurs in organic molecules with the energies available in the 200nm to 800nm spectral range. Consequently, favored electron promotion is excited from the highest occupied molecular orbital to the lowest unoccupied molecular orbital, which results in excited states. When the molecule is exposed to light with an energy matching a certain electronic transition, part of the light energy will be absorbed as the electron jumps to a higher energy orbital. The spectrometer records the wavelengths at which absorption occurs, in combination with the strength of absorption intensity at each wavelength. Usually, the spectrum is plotted as a graph of absorbance (A) versus wavelength. The intensity of the reference beam, which should have little or no light absorption, is defined as I_0 , and the intensity of the sample beam is defined as I_1 . In addition, absorption can be presented either as transmittance ($T = I_1 / I_0$) or absorbance ($A = \log I_0 / I_1$). The wavelength of maximum absorbance is a characteristic value, defined as λ_{\max} .

The basic principle of the absorption spectroscopy is introduced from the Beer-Lambert Law. This law defines a linear relationship between absorbance (A), concentration (M) of absorbing molecules in the sample and the thickness of the sample crossed by light. The ratio between the incident light intensity and the transmitted light intensity (for a specific wavelength) is exponentially dependent on the concentration c of absorbing molecules (at that specific wavelength) and the thickness of the sample crossed by the light. Beer-Lambert law is written as:

$$-\text{Log}(I_1 / I_0) = A = \alpha l c$$

{note that $T + A = 1 \Rightarrow A = 1 - (\%T) / 100$ }

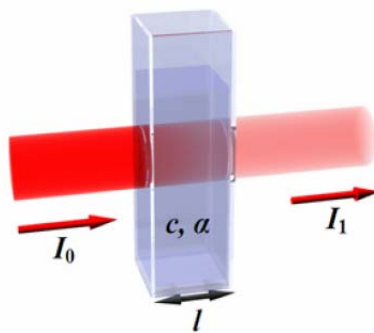


Figure 44. Beer Lambert Law

where A is the optical absorbance, I_0 is the intensity of the incident light, I_l is the intensity after passing through the sample, l is the sample thickness, c is the concentration of the absorbing species in the sample, α is the absorption coefficient or the molar absorptivity of the absorber and λ is the wavelength of the light. The absorption coefficient α is wavelength dependent and is specific to a molecule or a material. The variation of α versus the wavelength allows drawing the absorption spectrum of a material. Either absorbance or transmittance can be used for characterizing the properties and electronic structures of molecules. For a material to be transparent, the penetration depth must be large in comparison to its thickness. The high accuracy of absorption measurement allows characterizing the switching process of photochromic molecules investigated in this project.

The measurement of film thickness using reflected light is a well established technique [27]. Such optical techniques for the determination of thin film characteristics rely upon the interaction of the film with light and can be used to determine not only thickness, but also roughness and optical constants. They are dependent upon the interference pattern (or fringes) resulting from partial reflection/transmission through two partially reflecting surfaces.

In the case of a thin film on the surface of another material, both the top and the bottom surfaces of the film reflect light, with the total amount reflected being dependent upon the sum of these two reflections. Furthermore, these two reflections may add together constructively or destructively depending upon their phase relationship. This

phenomenon is due to the wavelike nature of light, with the phase relationship determined by the difference in optical path lengths of two reflections. The resulting interference pattern (interference fringes) can be used to determine the thickness of the film in question, assuming that the refractive index and the angle of incidence are both known. Conversely, refractive index can be determined if film thickness is known. Film thickness can thus be calculated using the following expression:

$$d = m_f / [2D_n (n^2 - \sin^2\theta)^{1/2}]$$

where d is the film thickness, m_f is the number of fringes in the wavenumber region used, n is the refractive index and D_n the wavenumber region used ($v_1 - v_2 \rightarrow 1/\text{cm}$).

In our case, we will use the absorption spectroscopy in order to calculate the minimum number of modes expected for a given thin film deposited on a glass substrate. For that purpose we will also use equation (1.25),

$$W_{\min} = (1/k) [m\pi + (\tan^{-1}[(n_s^2 - n_c^2) / (n_f^2 - n_s^2)])^{1/2}] / (n_f^2 - n_s^2)^{1/2}$$

which provides the minimum thickness acquired for a single mode to be excited. Therefore, the minimum number of modes expected is given by

$$m = \frac{k(n_f^2 - n_s^2)^{1/2} d - \arctan \sqrt{\frac{n_s^2 - n_c^2}{n_f^2 - n_s^2}}}{\pi}$$

where we have substituted $W_{\min} \equiv d = m_f / [2D_n (n^2 - \sin^2\theta)^{1/2}] = 2D_n n_f$ (for $\theta = 0$) calculated from the interference pattern.

A related program named *ModesNumberPrototype.m* is written in Mathematica code and is included in Appendix B. A function *GetFileRead* reads the values obtained from the spectrometer file and displays the interference pattern of the film. Another function named *TheModes* calculates the minimum number of modes m expected according to the theory stated in this section.

4.3 Measurement of the change in the refractive index based on the intensity profile of a thin film

As we have already seen in a previous section, when a light beam propagating in a medium of higher refractive index meets an interface at a medium of lower refractive index at an angle of incidence above a critical angle, the light is totally reflected at the interface and propagates back into the high refractive index medium. Although the fully reflected beam does not lose any net energy across the TIR interface, the light beam leaks an electrical field intensity called an evanescent field wave into the low refractive index medium, i.e. the beam penetrates a very short distance beyond the interface and into the less dense medium before the complete reflection occurs. The amplitude of this evanescent field wave, described from equations 1.9.i and 1.9ii (shown below)

$$C \exp(-qx) \quad , \quad x > 0 \quad (1.9.i)$$

$$E_y(x) = C [\cos(hx) - (q/h) \sin(hx)] \quad , \quad -t_g < x < 0 \quad (1.9.ii)$$

$$C [\cos(ht_g) + (q/h) \sin(ht_g)] \exp[p(x + t_g)] \quad , \quad x < -t_g \quad (1.9.iii)$$

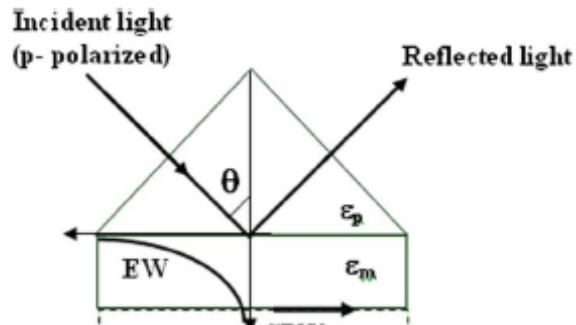


Figure 45. Evanescent wave field profile

decreases exponentially with distance from the interface, decaying in the directions orthogonal to its propagation direction. If the transmitted medium has a non-zero absorption coefficient, the evanescent field wave may transfer the matching photon

energy to it. This is exploited in internal reflection spectroscopy (IRS). Its intensity is reduced (attenuated) by the sample in regions of the IR spectrum where the sample

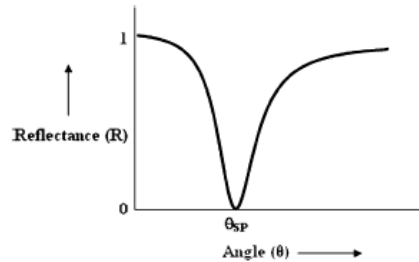


Figure 46. Reflectance dip at resonance angle

absorbs. If the light intensity is plotted against the angle of incidence, a characteristic dip can be seen due to the coupling. The angle of incidence that occurs at this point is known as the synchronous angle and is dependent on the local refractive index according to the equation of the modes

$$2 k n_2 \cos\theta_1 W - 2\Phi_{21} - 2\Phi_{23} = 2m\pi$$

The absorption of energy by the excited electrons induces a decrease in energy of the reflected beam and thus creates a reflectance minimum ($A + R = 1$: since $T = 0$ in the region of evanescent field, $A \uparrow \Rightarrow R \downarrow$). This means that within the area of the evanescent field chemical or physical interaction leads to a direct effect on the synchronous angle. This causes an alteration in the position of the mode angle and therefore, a change in the angle at which coupling occurs.

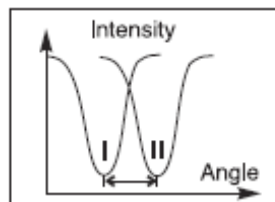


Figure 46. Resonance shift: (I) before and (II) after excitation

A few characteristic properties of the evanescent field in order to have a better insight of its physical meaning, are stated below:

- The penetration depth of the evanescent wave is usually defined as the distance over which the wave decays to $1/e$, or about 37%, of its maximum intensity and is given by

$$d_p = 1 / q = 1 / [\beta^2 - k^2 n_1^2]^{1/2}$$

Thus, the penetration depth, typically a few micrometers (μm), is a function of the incident angle.

- The evanescent wave is a non transverse wave, that is, it has electric field components directed in all spatial orientations during penetration into the lower refractive index medium.
- Intensity of the field decreases with increasing distance into the medium, normal to its surface. Therefore, the field exists only near the vicinity of the surface.
- The field intensity in the medium of lower refractive index is non zero, and there is an instantaneous normal component of energy flow into this medium, whose time average is zero (i.e. the time average of the x-component of the Poynting vector $\langle E_t \times H_t \rangle \hat{i}$ equals to zero) [28]. This signifies that, on average, no net energy flows in the x direction. Thus, there is no energy loss and the propagating radiation in the denser material is totally internally reflected.

Even though the evanescent wave does not transport any energy to the lower refractive index medium, the finite E-field in the “transmitted medium” can still polarize the atoms into it. On TIR, incident wave can not effectively penetrate the material, which corresponds to high reflectance. Relatively few electrons can “see” the transmitted wave, and therefore, although each absorbs strongly, little total energy is dissipated by them. Instead most of the incoming energy reappears as the reflected wave. Moreover, the

evanescent wave is non transverse, and therefore, has components in all spatial directions. This allows its vector components to interact with the dipoles in all orientations, causing it to be a more informative probe of the material.

In our case, we deal with the photo-chromic molecule of spiropyran, which in its closed form absorbs strongly in the UV region (between 320 and 400 nm). The open merocyanine form has a characteristic absorption band in the visible region between 500-600nm. Thus, upon UV irradiation, the absorption of energy by the ground state electrons of the closed form of SP-NO₂ will lead to the chemical transformation into the open merocyanine form accompanied with an alteration in the position of the synchronism angles. This will result in a corresponding change in the refractive index of the material. In order to measure the light – induced refractive index modifications, we will process a two beam setup known as the pump – probe method [29]. In this manner, we will use a first laser beam as a pump ($\lambda = 308\text{nm}$) to excite our sample and a second laser ($\lambda = 543,5\text{nm}$) to probe the refractive index modulation induced by the pump beam. Both pump and probe beams excite resonances in a single layer by the use of the TRPC (total reflecting prism coupler) described in theory. We note that irradiation with visible light induces back conversion to the closed colorless form.

Chapter 5

Experimental process

As mentioned in previous chapters, a well known method in order to measure thin film parameters is the prism film coupler. The refractive index and the thickness of a light-guiding film are obtained simultaneously and with good accuracy by measuring the coupling angles at the prism and fitting them through certain scaling rules for thin film optical waveguides. The experimental arrangement used for this purpose is shown below:

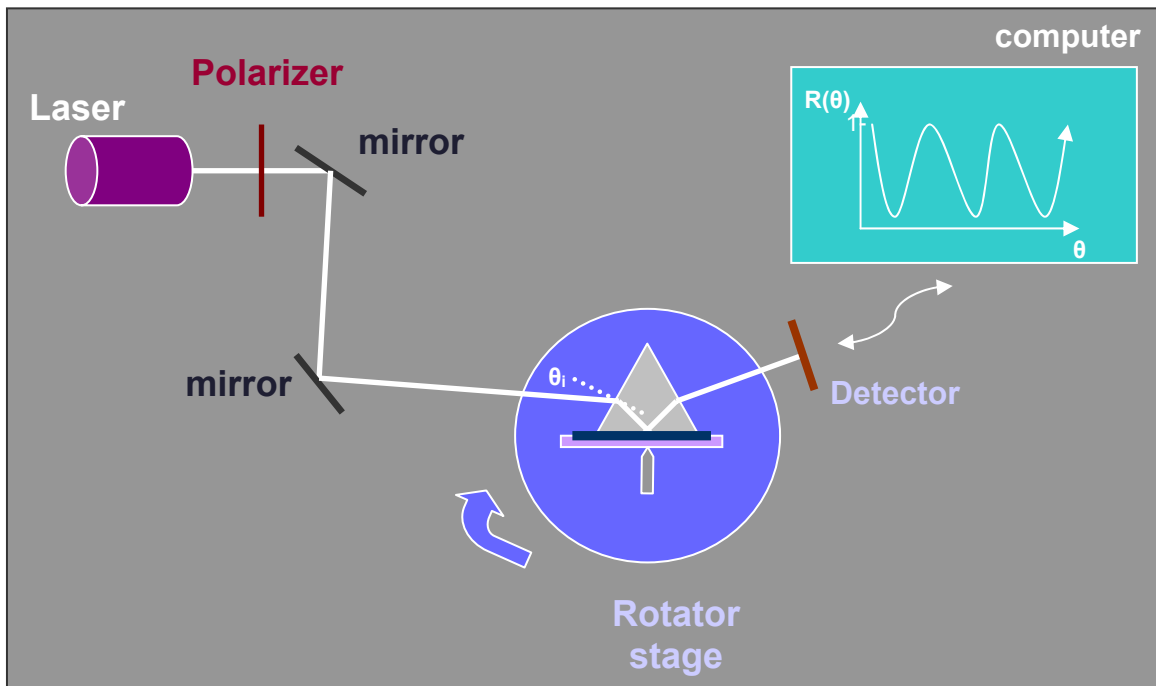


Figure 47. Experimental setup for the prism coupler

By mean of a spring-loaded clamp, the film is pressed against the base of a coupling prism. A laser beam, linearly polarized (TE or TM) by a polarizer, is directed through a system of lens and apertures onto the prism face, so that the beam coincides with the prism base. The point where the beam strikes the prism base is the coupling spot [10]. At this point, the parameters n and W are being measured. The prism sits on a yz translation stage that is mounted on a precision (~ 1 arcmin) rotary table or goniometer for the measurement of the incidence angles. For a calibration of the zero point of the angular scale we determine the position of the stage at which the beam is incident normally on the entrance face of the prism i.e. where the reflection from the front face of the prism goes back exactly into the incident beam. The angles of incidence on the entrance face of the prism are assigned positive or negative depending on whether the scale on the turntable increases clockwise or anticlockwise.

In our setup, we will use an He-Ne laser at 632nm, an SF6 optical glass prism with refractive index $n_f = 1.79884$, prism angle $\epsilon_p = 60^\circ$ and quartz substrates for our films to be deposited on with refractive index $n_s = 1.45702$. The value of the refractive index for the film and the prism at the 632nm wavelength is obtained according to the Sellmeier equation included in Appendix C.

5.1 Validation of the prism – film coupler method

In order to validate the prism film coupler method we will, at first, attempt to measure the refractive index of known materials such as PMMA and Polystyrene. For that purpose, we have prepared solutions of 1:7 weigh to volume polystyrene in toluene (1gr polystyrene – 7ml toluene) which were deposited afterwards on quartz substrates. In order to obtain a uniform solution, we have used the well known spin coat method, where optimum spinning velocity was set at 4000rpm (for 30sec and 1500rpm/sec).

Different spinning speeds alter the film thickness in a way that the greater the spin speed, the thinner the film becomes. In order to determine whether the thickness of our film deposited on the substrate is optimum (and thus the spin speed) i.e. our waveguide to support at least 3 modes, we act as follows: according to the theory stated in section 3.1 we get the absorption spectrum (or the transmittance) of our film, as shown below, within a range of wavelengths between 250nm and 1100nm, where the wavelength of our laser beam lays.

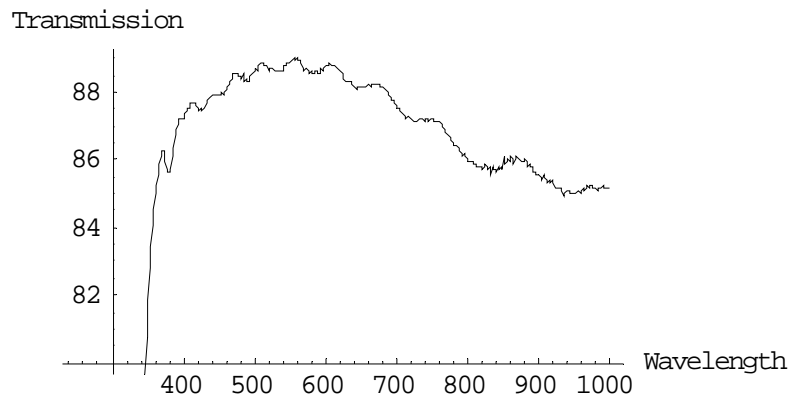


Figure 48. Transmission spectrum

We can see from the interference pattern that between the range of wavelengths 540nm and 680nm, the number of fringes obtained is $m_f=3$. Using equation

$$d = m_f / [2D_n (n_f^2 - \sin^2\theta)^{1/2}] = m_f / 2D_n n_f \quad (\text{for normal incidence})$$

and substituting the refractive index of our film as $n_s = 1.585$ according to theory and $n_c = 1$ for the air – cover, we get the number of modes expected

$$m = \frac{k(n_f^2 - n_s^2)^{1/2} d - \arctan \sqrt{\frac{n_s^2 - n_c^2}{n_f^2 - n_s^2}}}{\pi} = 4$$

Thus, the film has the optimum thickness ($d = 2134.35$ nm for this case) acquired for the selected spin speed. We note that the results stated above are obtained through a program written in Mathematica code included in Appendix B.

The film constitutes an ideal waveguide and therefore, is mounted on the rotating stage in order to measure the synchronism angles and subsequently the effective refractive index according to equation

$$\beta/k = n_p \cos[(90^\circ - \varepsilon) + \sin^{-1}(\sin \alpha / n_p)]$$

. The calculated angles are shown in the following table:

θ_1	θ_2	θ_3	θ_4	θ_5
-2.4 °	-0.883333 °	1.6 °	4.9 °	8.816667 °

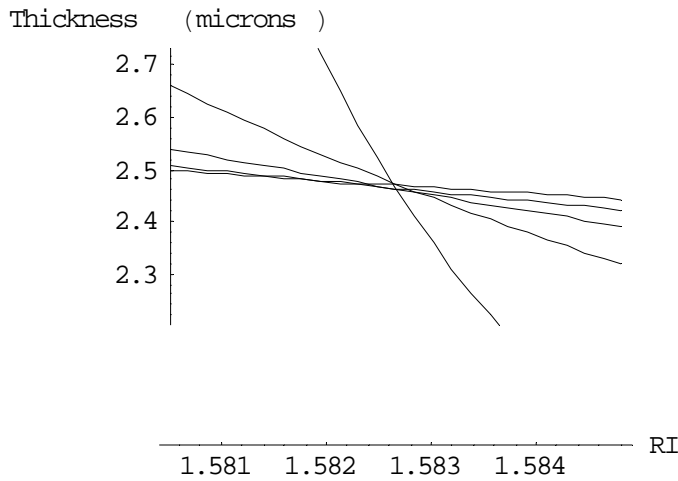
The values are entered in the program SLABv3.m, according to the methodology proposed in section 4.1, the output of which is given below:

```
<<SLABv3.m
```

```
betaF[{-2.4,-0.883333,1.6,4.9,8.816667},1,1.79884,60]
```

```
{1.57836, 1.56549, 1.54369, 1.51338, 1.47554}
```

$teModes[\{1.5783567915040329, 1.5654921548390368, 1.5436926388144052, 1.5133753957896878, 1.4755390751193842\}, 1.45702, 1, 632.8 \cdot 10^{-9}]$



$$\text{Thickness} = 2.46723 \times 10^{-6}$$

$$\text{Refractive index} = 1.58266$$

The refractive index of polystyrene obtained by this method is in good agreement with the one stated in theory [30], which is $n_{\text{polystyrene}} = 1.586$ at laser wavelength 632.8nm. We can see that the number of modes obtained in reality (5 modes) is greater than the number of modes expected (3 modes). This is because of the approximations made for the calculation of the expected number of modes, since the interference pattern method has given a smaller value for the thickness of the film. Note, also, that the angles measured by the goniometer are given in arcmins, thus, we have to convert each value in degrees in order to enter them in the program. The conversion is realized by the formula

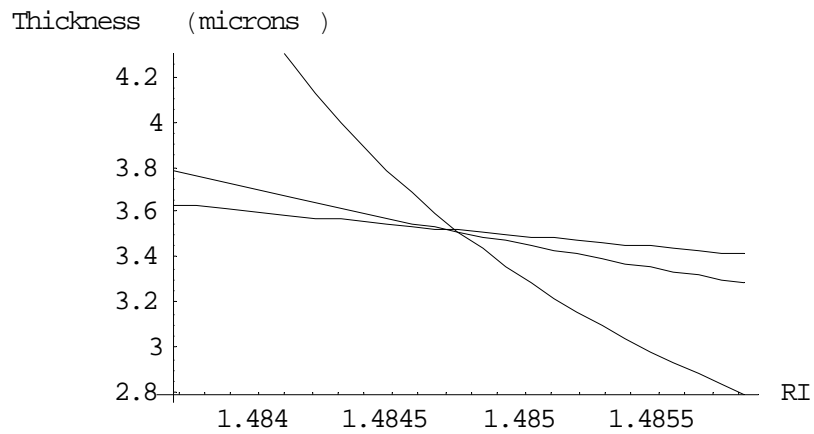
$$1 \text{ arcmin} = \text{degrees} / 60$$

For example, the first synchronous angle is measured to be $-2^{\circ} 24''$. In that way, $24 / 60 = 0.4$ degree and the angle's value in degrees becomes then 2.4° .

In the same manner as described above, we have calculated also the refractive index of PMMA. The synchronism angles measured are tabled below:

θ_1	θ_2	θ_3
8.1	8.75	9.783333

The experimental value for the refractive index is 1.48475 and for the thickness 3.51521 μm . The result obtained is in very good agreement with the theoretical value $n_{\text{PMMA}} = 1.486$ [30].



$$\text{Thickness} = 3.51521 \times 10^{-6}$$

Refractive index = 1.48475

5.2 Application of the prism-film coupler method for the calculation of the refractive index of unknown materials

After validating the prism film coupling method for characterizing thin film parameters of known materials, we will proceed in an analogous way but for materials that those parameters are unknown. The sol-gel method, already described in chapter 3, will be used as a fabrication procedure. Inorganic – organic hybrids, which are materials typically produced by this method, have the ability to modify their properties by the incorporation of dopants or other functionalized groups. In our case, we will use a silicon hybrid material containing zirconium (Si-O-Zr), which is known to strengthen the system, modify the refractive index and improve the mechanical stability when added to the precursor solution. The doping process takes place via the reaction of silanol groups with ZrOR groups, which affects the system as to reduce drying times and impart enhanced mechanical stability to deposited films [31]. This makes the cured material potentially stronger than the conventional acrylate or epoxy resins. In general, mechanical properties of the material are described as a function of percentage zirconium.

The sol-gel film is fabricated from methacryloxypropyl trimethoxysilane (MAPTMS) and methacrylic acid (MAA), both of which had photopolymerizable C = C double bonds groups, and zirconium n-propoxide ($Zr(OPr)_4$) as an inorganic network former. Firstly, MAPTMS was hydrolyzed with dilute HCL and the mixture was stirred for 30minutes. In a second reaction vessel MAA and zirconium isopropoxide ($ZrOPr_4$) were combined in several molar ratios (shown in the table below). An equal volume of 1-PrOH was then added to the chelated zirconium and the sol was stirred for 30min. It was then added dropwise to the hydrolyzed silane precursor (MAPTMS sol). This mixture is able to make a mineral and an organic network as illustrated in Figure 49. The mineral network (gel) is obtained through the hydrolysis and the polycondensation of alkoxide groups. The organics network is created by the polymerization of double bonds under UV exposure [39]. Thus, a standard amount of 0.01gr of the photoinitiator Irgacure 369 was added to the mixture, which was left stirring for a day afterwards. The photoinitiator used, presents strong single photon absorption in the 320nm-420 nm region. Next, the sol-gel was spin -

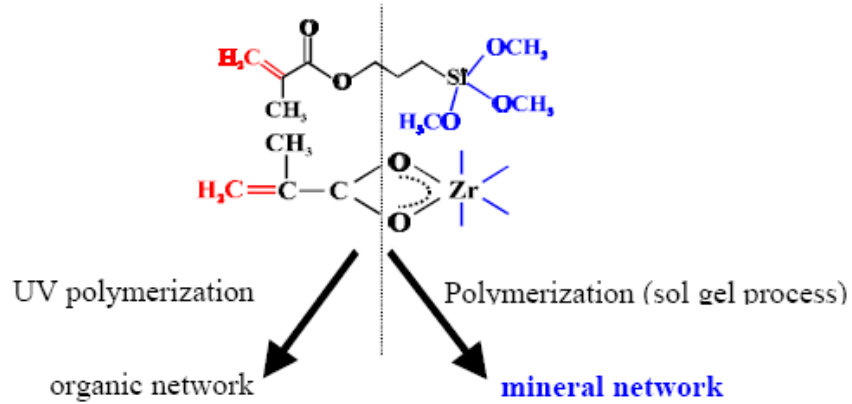


Figure 49. MAPTMS – Zr(OPr)₄ sol -gel

coated on quartz substrates and the resultant gel films were prebaked at 100 °C for an hour in order to remove solvents and give mechanical stability to the mineral network formed. Finally, the film exposed for another hour under a UV lamp for the initiator to act (on the organic part). The UV polymerization process induces the conversion of small unsaturated molecules in the liquid state to solid macromolecules either through polymerization or through crosslinking [13]. In the former case macromolecules are created through chain reactions, while the latter case is concerned more with the formation of crosslinks with chemical bonds. Both cases results in a refractive index increase.

The amount of MAPTMS used for each sample is 0.7gr diluted in 0.07gr HCl 1M. The molar weights and the density of the various materials used are:

Mw_{MAPTMS} : 248,1gr/mol

Mw_{MAA} : 86.1gr/mol , d = 1.015gr/mol

$Mw_{Zr(OPr)_4}$: 327.28gr/mol , d = 1.058gr/mol

The ratio $Zr(OPr)_4 / MAA = 1 : 4$ holds for all samples

A control sample without added Zirconium was also prepared.

Table 1. Molar Ratios of MAPTMS – Zn(OPr)₄

MAPTMS:Zn(OPr)₄	Zn(OPr)₄ (ml)	MAA (ml)	Propanol – 1 (ml)
10:0	-	-	-
9:1	0.139	0.108	0.145
8:2	0.312	0.239	0.75 (Toluene)
7:3	0.533	0.410	0.145
6:4	0.830	0.637	1.8
5:5	1.246	0.937	5.25

Our intention is to measure the refractive index modulation as a function of the percentage of zirconium added. For that purpose, we have used the same experimental setup as before, with the only addition of a second laser of 825nm in order to validate our results at two wavelengths. The lasers were aligned in that way as to excite resonances in the waveguide at the same (or close enough) position of the rotation stage. The experimental setup is shown as follows:

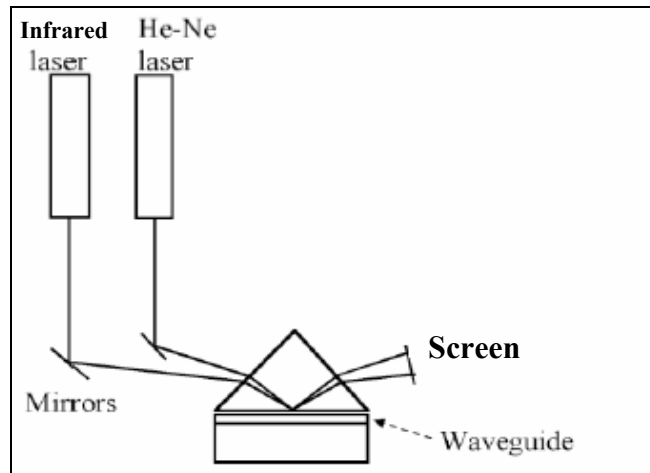


Figure 50. Experimental arrangement

From the absorption spectra of our films, depicted in the scheme below, we can see that our materials show little absorption at the working laser wavelengths (632.8nm and

825nm) and so no laser attenuation would be expected. We can also observe a strong absorption band at 320-420 nm that is due to the presence of the photoinitiator, since the same peak is also present at the control sample (10#0, no zirconium added). As it seems, even though our samples have been exposed to UV irradiance, still some amount of Irgacure 369 has remained in the sample.

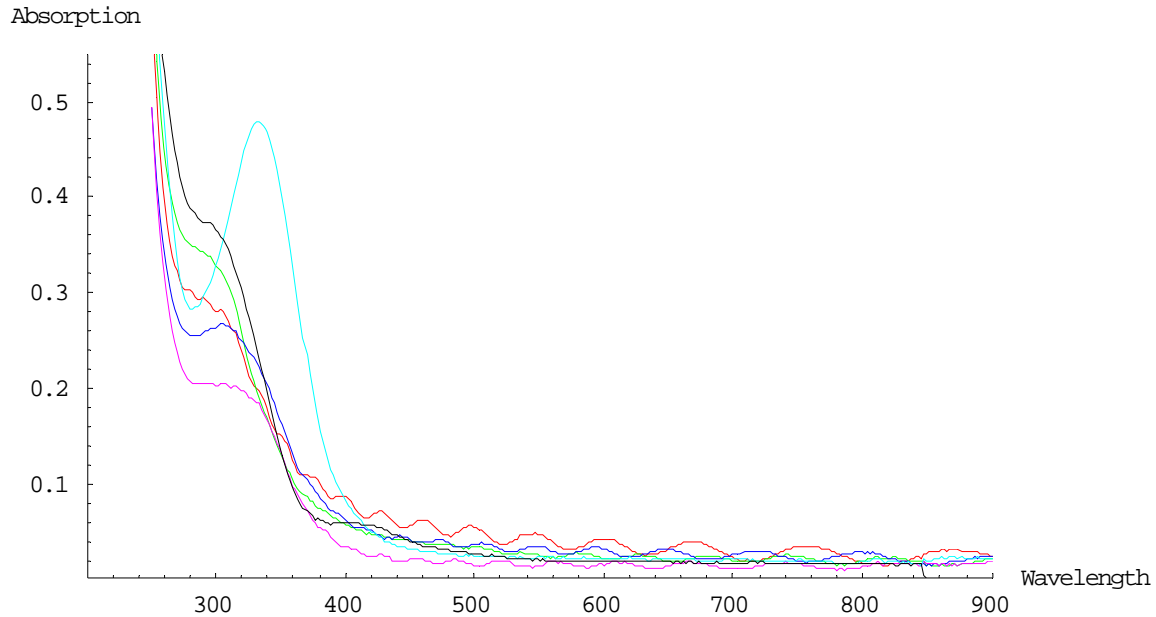


Figure 51. Absorption spectra of all the ratios MAPTMS – Zr(OPr)₄

The synchronism angles, as well as, the refractive index and the thickness measured for the films of different zirconium concentration are presented in the following tables for both laser wavelengths. The related diagrams for *Thickness* versus *Refractive Index* calculated through the program SLSBv3.m are presented in sequence.

Table 2. Synchronism angles of several ratios MAPTMS-Zr(OPr)₄ measured using an He-Ne (632.8nm) and an Infrared (825nm) laser

<u>Molar</u>	<u>He-Ne : 632.8 nm</u>				<u>Infrared: 825 nm</u>		
10:0	7.95°	8.9°	10.333333°		7.7°	8.216667°	9.05°
9:1	6.5°	7.2°	8.333333°	9.83333°	5.9°	7.0166667°	8.783333°
8:2	4.966667°		6.316667°	8.45°	4.533333°	6.65°	9.616667°
7:3	4.0666667°	5.616667°	8.0833333°		3.75°	6.133333°	9.566667°
6:4	3.35°	4.616667°	6.65°	9.3°	2.75°	5.0166667°	8.483333°
5:5	2.383333°	4.716667°	8.3°		2.1°	4.983333°	9.166667°

Table 3. Refractive index and related thickness measurements for all ratios MAPTMS –ZN(OPr)₄ for the He-Ne

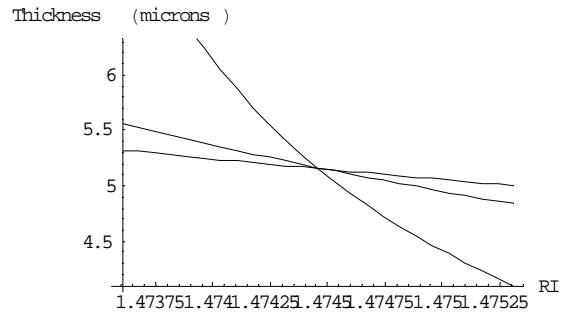
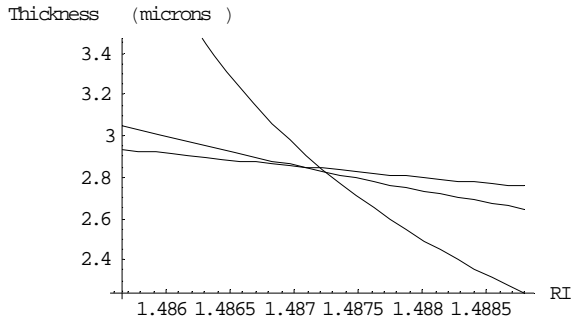
<u>He-Ne : 632.8 nm</u>	Refractive Index	Thickness (microns)
10:0	1.48986	5.19648
9:1	1.5004	3.48023
8:2	1.51703	2.37816
7:3	1.52604	2.28458
6:4	1.5317	2.59495
5:5	1.54379	1.84327

Table 4. Refractive index and related thickness measurements for all ratios MAPTMS –ZN(OPr)₄ for the Infrared

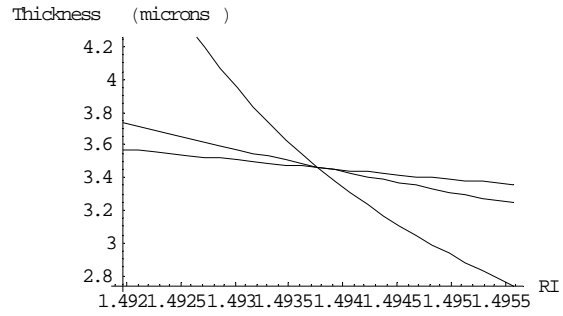
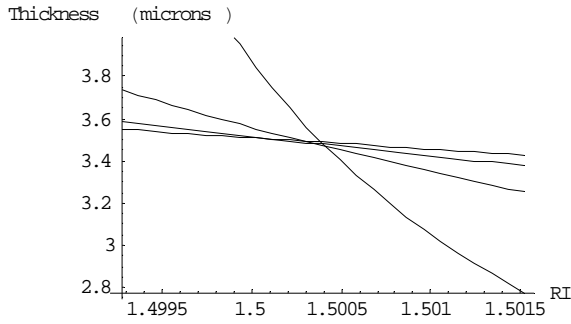
<u>Infrared: 825 nm</u>	Refractive Index	Thickness (microns)
10:0	1.47446	5.15936
9:1	1.49377	3.4636
8:2	1.50984	2.4452
7:3	1.51798	2.29738
6:4	1.52662	2.41243
5:5	1.53438	2.11152

He-Ne (632.8nm)

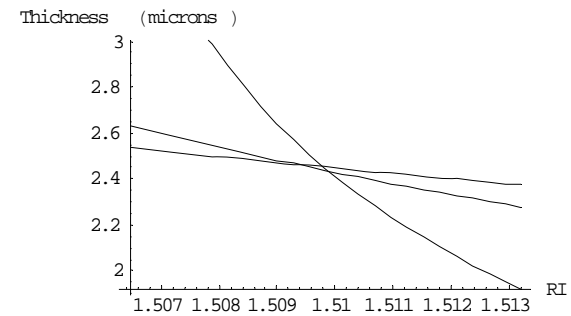
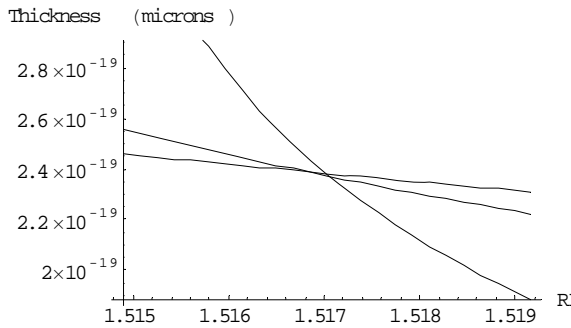
Infrared (825nm)



10#0



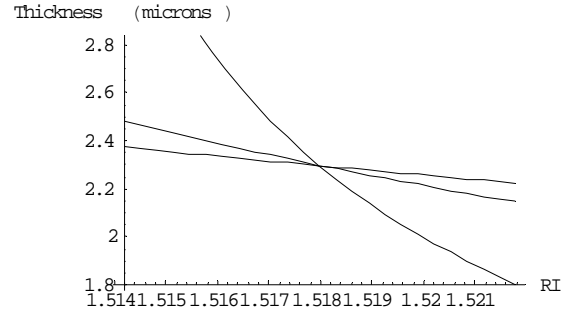
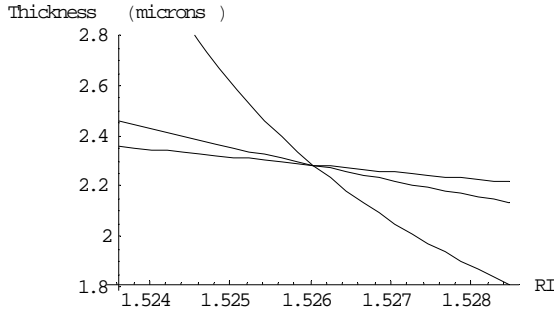
9#1



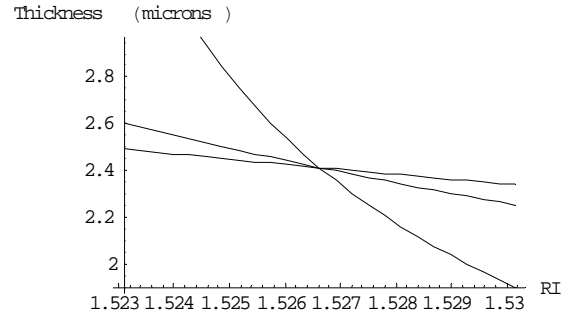
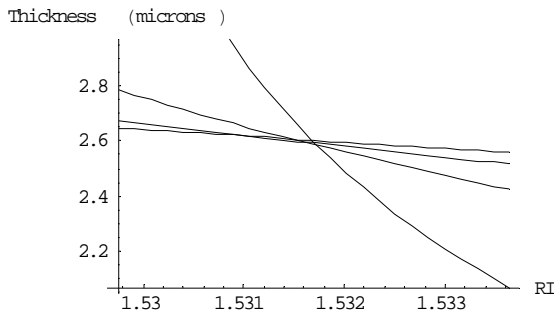
8#2

He-Ne (632.8nm)

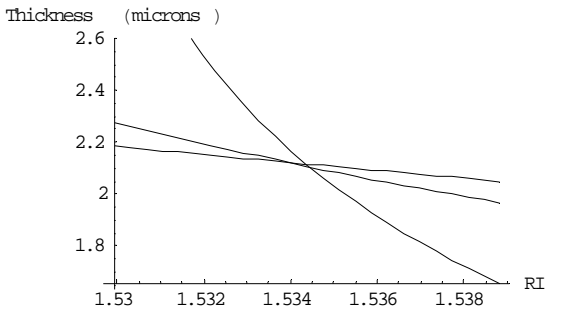
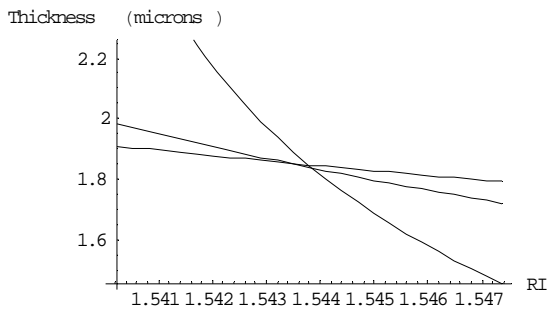
Infrared (825nm)



7#3



6#4



5#5

Next, we have tabulated the refractive index modulation versus the concentration of zirconium for both laser wavelengths. As we can see from the diagram, the refractive index shows a very good linear relationship in relation to zirconium concentration for both wavelengths ($R^2 = 0.9817$ for the He-Ne and $R^2 = 0.9588$ for the infrared). Furthermore, this linear relationship is positive since the refractive index increases as the concentration of zirconium increases too. This behaviour presents a strong evidence for the way that the properties of hybrid organic materials can be modified by the incorporation of dopants offering, in that way, the possibility of a better controlling of their mechanical stability. For all the measurements taken, the refractive index has presented greater values for the He-Ne (shorter wavelength) in comparison with those taken for the infrared, which is in agreement with the theory.

An interesting remark, that one can also make, is that occasionally the number of modes excited for each film (of a certain molar ratio) differs for the two wavelengths. Characteristic examples constitute the molar ratios 9#1 and 6#4, where four modes were excited with the use of He-Ne and three modes for the infrared. In all cases, the number of modes excited by using the 632.8nm wavelength is greater than or equal to those related to the 825nm. This is in good agreement with the related equation stated in section 4.1

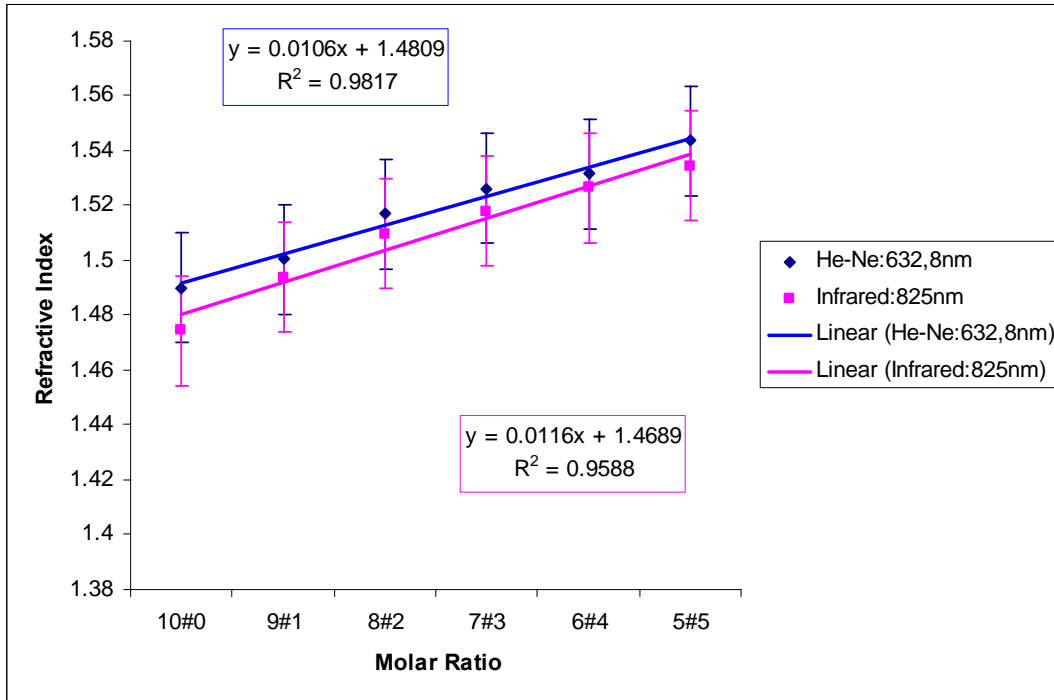
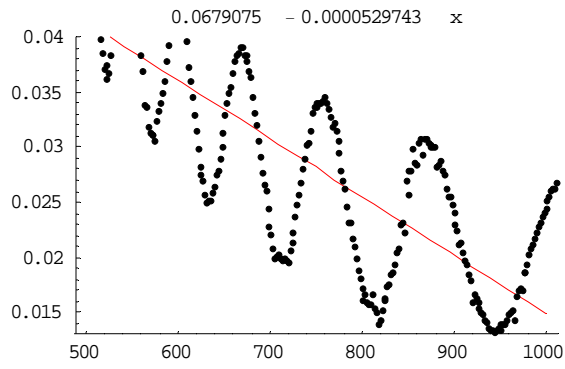
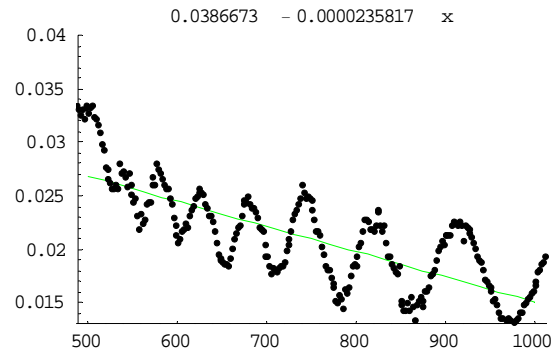


Figure 52. Refractive index modulation versus the concentration of zirconium (both wavelengths)

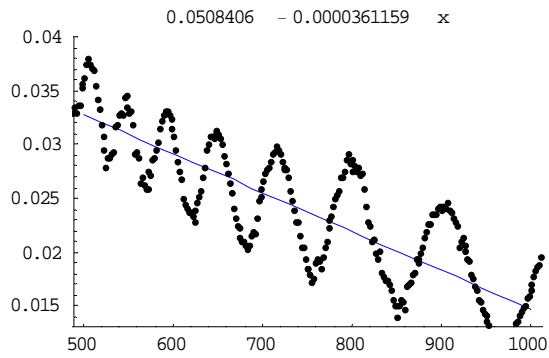
Combining the results taken from the absorbance spectrum and the related thickness for each film, we can tabulate the way that absorption coefficient, α , is related to the concentration of zirconium. Each value was approximated through a linear fitting of absorption's variation in a range of wavelengths close to those used in the experiment. The wavelengths of the lasers substituted to each linear curve and thus, the related value for absorption was obtained. The related linear fitting curves are stated below and the results obtained are concentrated in a table shown in sequence.



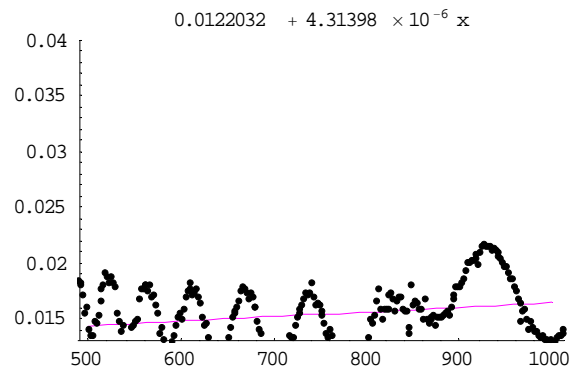
5#5



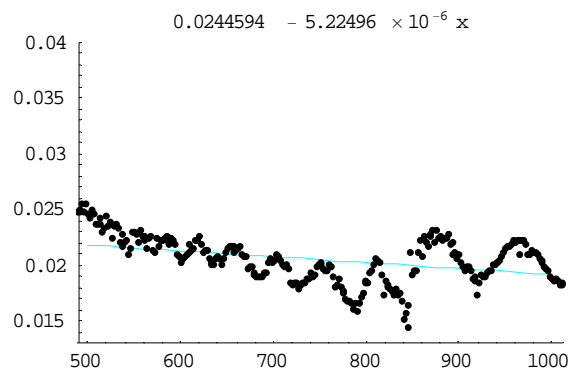
6#4



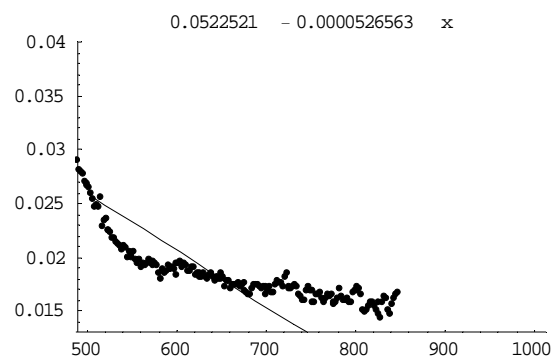
7#3



8#2



9#1



10#0

**Table 4. Absorption coefficient measurements for all ratios
MAPTMS –Zn(OPr)₄ for the Infrared and the He-Ne**

<u><i>Absorption coefficient</i></u> <u><i>(1/cm)</i></u>	He-Ne : 632.8 nm	Infrared: 825 nm
10:0	36.438	17.077
9:1	60.7805	58.173
8:2	62.7927	64.4618
7:3	122.502	91.6043
6:4	91.5039	79.6392
5:5	186.546	114.627

As we can see from the diagram of the absorption coefficient versus zirconium concentration and the related fitting curves, there is a good linear relation between those two parameters. The linear relation is positive since both values increase together. As the absorption coefficient is wavelength dependent and is specific to a molecule or a material, we can claim once again for the strong effect of zirconium as a dopant in inorganic – organic hybrid material system. The positive linear relation dominates for both laser wavelengths and is greater for the case of the infrared. Besides, in this latter case the measurements taken are within the limits of the error bars in relation to those taken with the He-Ne laser, where the results show greater fluctuations. Since the absorption coefficient is related to the sample thickness, inaccuracies during measurements seem to have played a more important role in the latter case.

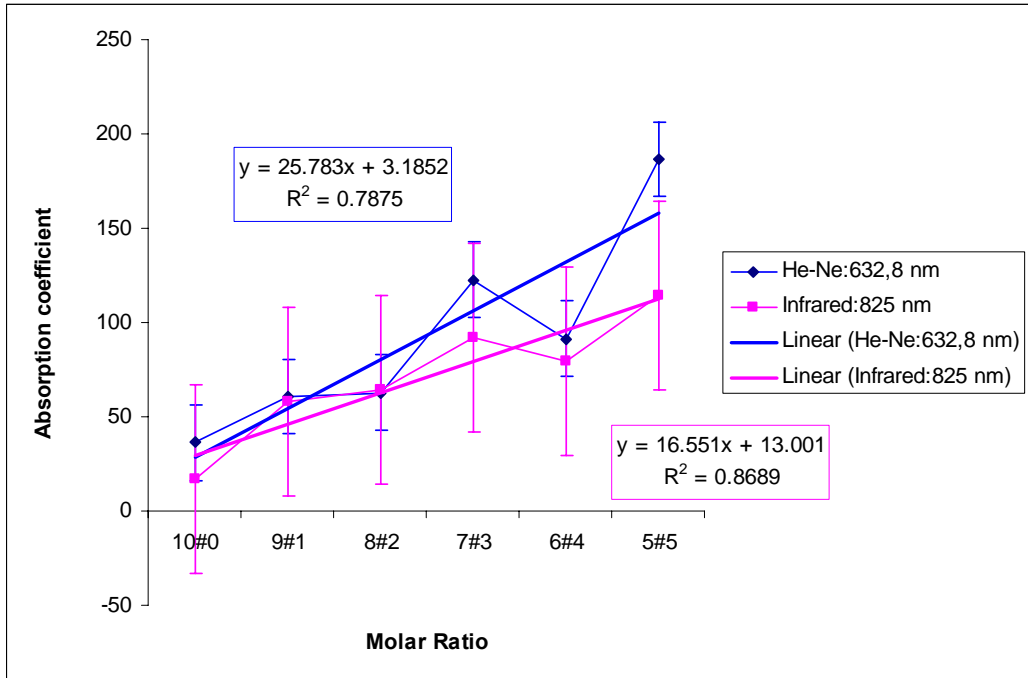


Figure 53. Absorption coefficient versus the concentration of zirconium (both wavelengths)

5.3 Measurement of the change in refractive index based on the intensity profile of a thin film

In order to characterize light – induced refractive index modifications in photochromic doped polymeric matrices, we will use a two-beam setup as the one stated in the previous section. Sp – NO₂ will serve as a dopant and PEMMA (polyethyl methacrylate) as a host polymeric matrices. The excitation of the specific photochromic molecule, from the closed spiropyran to the open merocyanine form, will take place with the use of a UV pulsed laser (pump), 308nm of wavelength and pulse frequency 3Hz according to those stated in theory. The reversible transformation to the original state will be performed with the use of a 543.5nm wavelength laser (probe), since the excited merocyanine presents high absorption in the visible region. In this case, the lasers are aligned in a way as to excite resonances simultaneously at the same position of the rotation stage. Our intention is to measure the variation in the refractive index of the material by the pump induced translation of the probe m-line. The two – beam setup is shown in the scheme below:

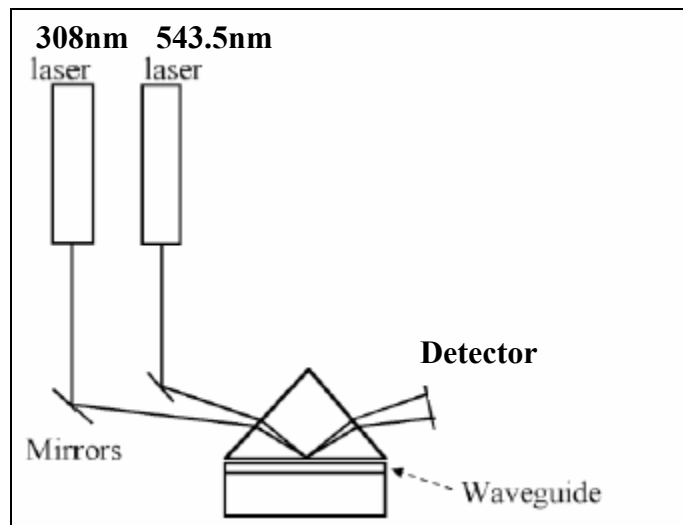


Figure 54. Experimental set-up

Both beams are focalized at the same place on the prism base. Each beam is coupled to the waveguide and excites a resonance. A light detector is located in the reflected probe

beam and is used to record the change in light intensity due to the lateral displacement of the probe m – line. The profile of the m-line is recorded by a computer under LABVIEW application.

In order to find the synchronism angles with the aid of the photodetector, we scan the intensity profile of the reflected beam by varying the position of the rotary stage. If the light intensity is recorded against the angle of incidence, a characteristic dip can be seen due to the mode excitation. Note that, perfect coupling is indicated by the appearance of a small black line inside the reflected spot, thus in that case, the intensity dip becomes the sharpest we can get providing more accuracy in our measurements.

Firstly, we fabricate several solutions of SP-NO₂ – PEMMA by varying the %wt ratio of our materials. The amount of PEMMA used is fixed (0.5 gr) and the solvent diluted in will be Toluene (2.5ml). The ratios PEMMA-Toluene used show good quality for the resultant deposited films according to the interference pattern obtained as discussed in section 4.1. As one can see, the solution is almost totally transparent to the region of laser wavelengths we intend to use.

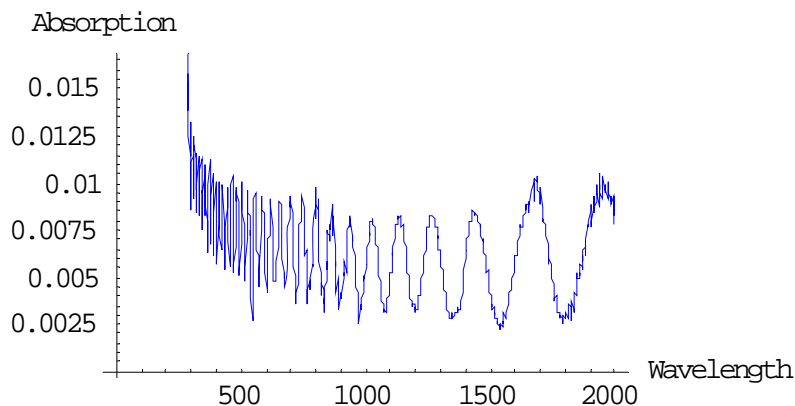


Figure 55. Absorption spectrum of PEMMA

Next, we are going to dope the PEMMA-Toluene solution by adding SP-NO₂ in several ratios. The solutions are deposited on quartz substrates, then spin coated at appropriate spin speeds and, finally, left to dry in vacuum for a day. The several solutions fabricated by varying the ratio SP-NO₂ – PEMMA are shown in the table below.

Table 5. Several ratios SP-NO₂ – PEMMA

SP (%)	3%	5%	7%	9%	11%	13%
PEMMA (%)	97%	95%	93%	91%	89%	87%
SP						
(gr)	0,015	0,026	0,038	0,049	0,062	0,075
PEMMA (gr)	0,5	0,5	0,5	0,5	0,5	0,5
Toluene (ml)	2,5	2,5	2,5	2,5	2,5	2,5

By using the prism-film coupler method, we have measured the synchronism angles and the related intensity profile for each deposited film. For the former case, the results obtained are summarized in table 6 and for the latter, Figure 56 demonstrates reflectance changes over time for the 95%:5% PEMMA-Sp film, while varying the incident angle. The intensity profile of the reflected beam is recorded over time intervals (counts) of 0.2 sec.

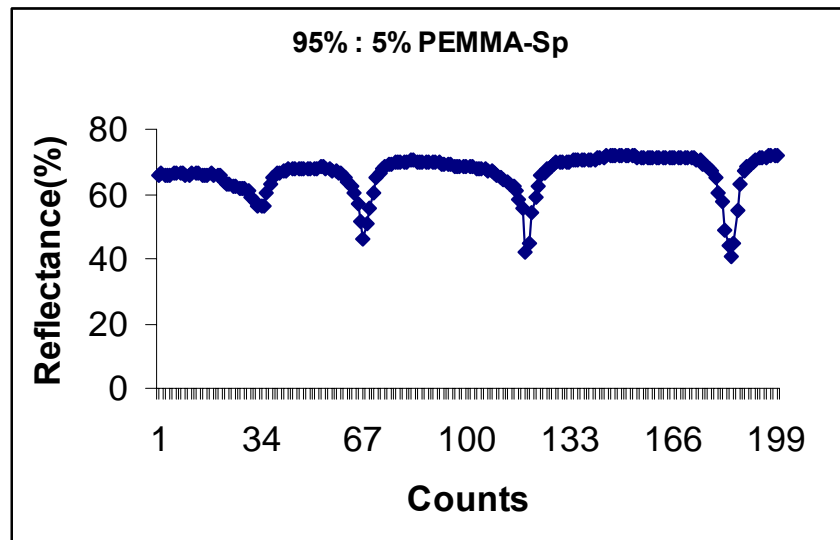


Figure 56. Reflectance variation over time of 95% : 5% PEMMA-Sp

**Table 5. Synchronous angles, Refractive index and Thickness
variation for several ratios SP-NO₂ – PEMMA**

<u>Ratio</u> <u>Sp-PEMMA</u>	543.5 nm Synchronous angles (°)				Refractive index	Thickness (µm)
100% : 0%	8.33333 3	8.9	9.85		1.49466	3.26507
97% : 3%	8.1	8.85	10.0666667		1.49754	2.81416
95% : 5%	7.8	8.31666	9.166667	10.33333	1.49969	3.47911
93% : 7%	7.31666	7.9	8.866667	10.16666	1.50461	3.27328
91% : 9%	7.38333	8.25	9.633333		1.50488	2.63372
89% : 11%	6.68333	7.66666	9.233333	11.26666	1.51199	2.47938
87% : 13%	6.43333	7.31667	8.783333	10.68333	1.51411	2.62283

Regarding the refractive index modifications of PEMMA in relation to spiropyran concentration (shown in Figure 57), we can see that by adding spiropyran in the host polymer, the refractive index of the matrix increases. This is in accordance with the absorption spectra of PEMMA before and after doping with spiropyran (1% SP – 99%PEMMA), where a peak is introduced in the range 300nm-400nm and a slightly increase in absorption for all the range of wavelengths is observed (Figure 58). In addition, the refractive index increment presents a strong linear relation to the concentration of the photochrome.

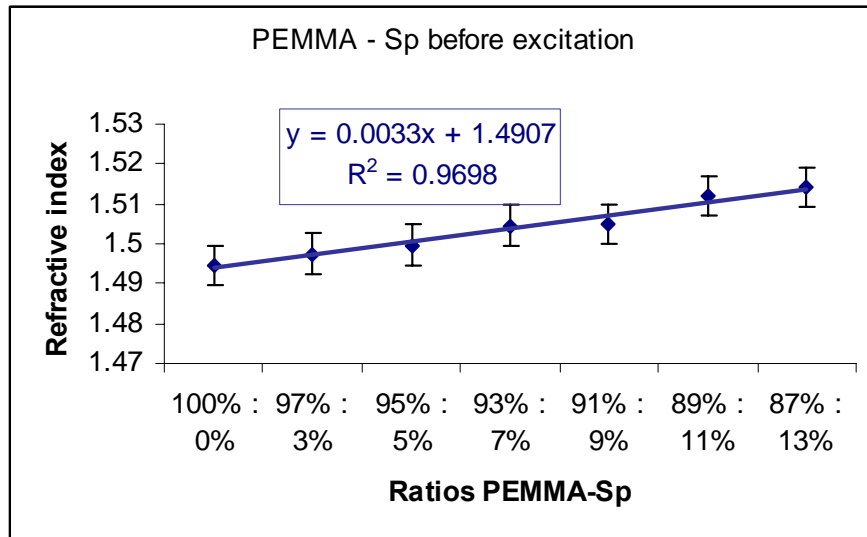


Figure 57. Refractive index modulation versus several ratios PEMMA-Sp before excitation

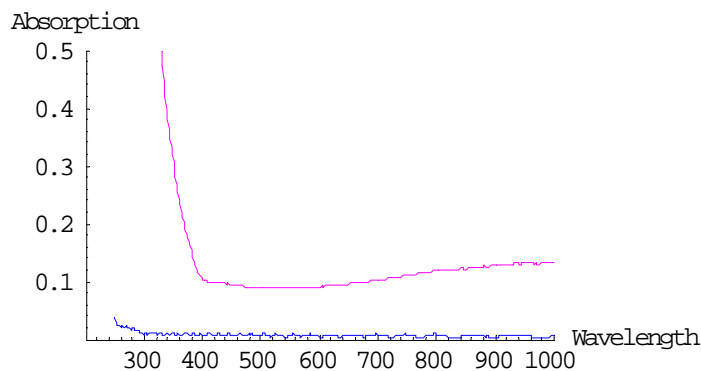


Figure 58. Absorption spectra of PEMMA before (blue line) and after doping with spiropyran (red line)

Now, in order to characterize the photoinduced manipulation of the photochromic spiropyran into the polymeric matrix of PEMMA, we have excited one of our samples (95%:5% PEMMA-Sp) using the UV pump laser. The response of the excited spiropyran observed through the variations in transmittance intensity profile of the probe beam, before and after excitation, recorded by the photodetector. The time profiles of

transmittance change are demonstrated in figure bellow [47, 49]. The absorption spectra before and after UV excitation is shown in sequence.

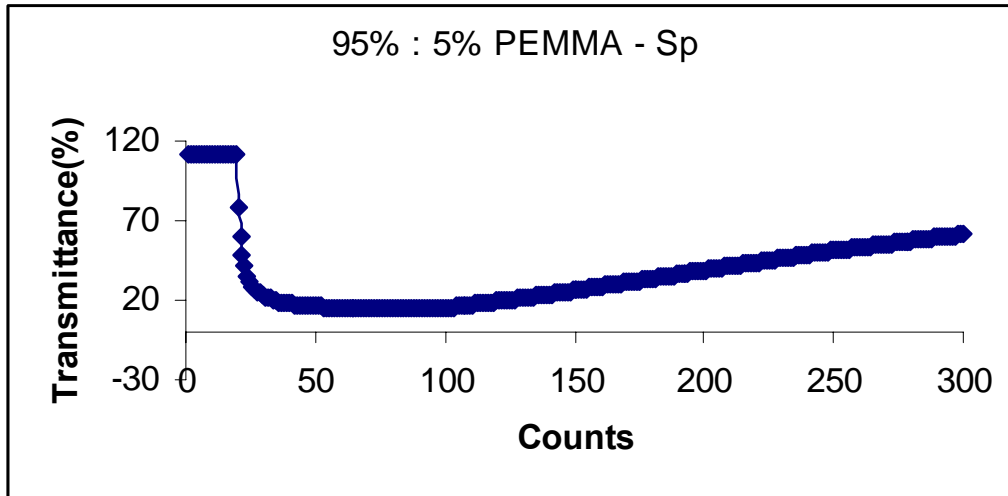


Figure 59. Time profiles of transmittance change

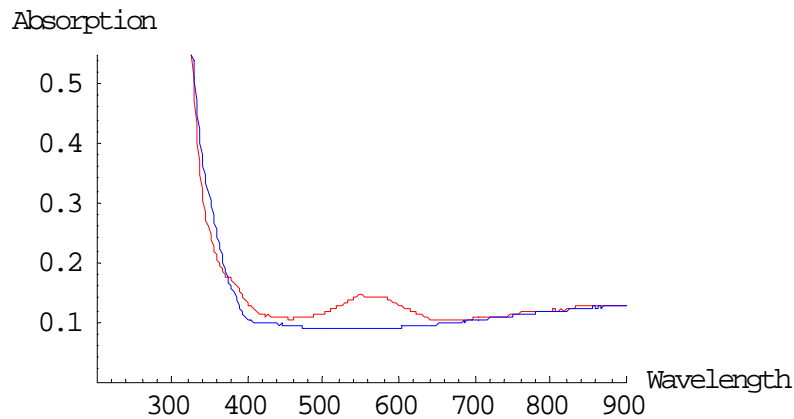


Figure 60. Absorption spectra of PEMMA - SP before (blue line) and after excitation (red line)

According to the transmittance curve over time, it is obvious the immediate decrease in intensity upon UV irradiation. Firstly, transmittance is 100% that is the sample is totally transparent to 543.5nm irradiation. On the 18th count, irradiation with UV laser begins

(UV on) and excitation of spiropyran takes place, in accordance with the sharp drop on the intensity profile. The sample strongly absorbs over a short time interval (~ for 50 counts) until it reaches a saturation, i.e. the transmittance plateau (from 54 to 104counts), which indicates that the open merocyanine has isomerized to its most stable forms. On the 104th count UV irradiation terminates (UV off) and transmittance increases slowly as the sample returns back to its original state i.e. the closed form (not fully recorded).

Those stated above are strongly supported by the absorption spectra of our sample before and after UV irradiation. A quite obvious peak around 500nm – 600nm is introduced after irradiation with the 308nm laser beam, as well as, the presence of high absorption at UV region before excitation. The wavelength of maximum absorption shifts to the red, which is in accordance with the observed purple color at the excited region of the film against the surrounding unexcited colorless area.

In order to measure the changes in the refractive index of the SP doped PEMMA films upon UV irradiation, we will be based on the procedure described in several papers [40, 41]. The main idea relies on the fact that due to film excitation, the intensity profile of the probe beam will change causing a lateral shift to the m line. The resonance dip moves toward bigger or smaller angles, as shown in the scheme bellow, and thus, we can see on

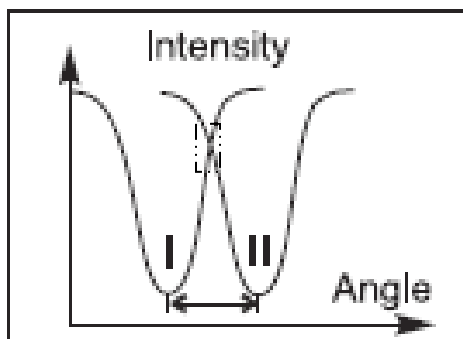


Figure 61. Lateral displacement of resonance minimum

the screen, the black line on the related m-line's bright spot to move on the right or left side respectively. In order to find the displacement of the resonance angle, the photodiode is placed at the position at which the slope of the intensity curve of the m line is the

highest (dashed area). The highest signal variation will be, thus, obtained. In this manner, supposing that the reflected spot relies within the dashed area, upon UV excitation, an immediate decrease in intensity is observed, as the resonance dip is displaced, until it reaches a saturation point. This local minimum either relies exactly on the minimum intensity, or slightly left or right in relation to the dip's new position. Relaxing back the film by green irradiation and slightly moving towards bigger or smaller angles (~5 arcmins step) close to the previous position, we re-excite the sample until a new saturation point is reached. Whether the new minimum is greater or smaller than the previous one, we continue moving towards the same or the opposite direction respectively, until the angle of minimum intensity is found.

In accordance to those stated above, we have measured the resonance shift of the 0th order mode for each concentration. The calculated variation in refractive index is again based on the code written in Mathematica program SLABv3.m, yet slightly altered. The main assumption is to consider that the thickness of the film remains unaffected by the isomerization process within the range of 1 μm accuracy provided with this method. Now, the user arbitrarily applies a range of values for the refractive index, in order to reach the value of thickness already known. The method demands user's interference within the inner code of *teModes* function, several times until thickness value is well approximated. An example is given below. The underlined region is the code alteration and the value in italic form represents the range of values applied by the user. Thereby, *NMinimize* inner function is disregarded.

```

teModes[modeIndex_List,ns_,nc_,lambda_] :=
  Module[{k,ri,filmIndex,dummy},
    k=2 Pi/lambda;
    filmIndex= modeIndex[[1]] + 2.467 10(-3);
    Plot[Evaluate[te[modeIndex,x,ns,nc,k] 1 106,
{x,modeIndex[[1]]+(filmIndex-modeIndex[[1])/2,
filmIndex+(filmIndex-modeIndex[[1])/2},
AxisLabel -> {"RI", "Thickness (microns)"},
AxisOrigin -> {modeIndex[[1]]+(filmIndex-modeIndex[[1])/2,

```

```

te[modeIndex,filmIndex+(filmIndex-modeIndex[[1]])/2,
ns,nc,k][[1]]*1 10^6}
];
Print["Thickness = ",N[Mean[te[modeIndex,
filmIndex,ns,nc,k]],3]];
Print["Refractive index = ",N[filmIndex,6]];
]

```

For each film, the resonance shift of the 0th order mode obtained in this manner is concentrated in table 6. The related refractive index measurement and the approximated thickness are shown in parallel columns.

Table 6. The resonance shift of the 0th order mode for several ratios SP-NO₂ – PEMMA and the related refractive index and thickness measured

<u>Ratio</u> <u>Sp-PEMMA</u>	543.5 nm 0 th order resonance shift Before / after		Refractive index	Thickness (microns)
97% : 3%	8.1	8.366667	1.49491	2.81414
95% : 5%	7.8	8.133333	1.49642	3.47912
93% : 7%	7.316667	7.633333	1.50152	3.2733
91% : 9%	7.383333	7.716667	1.50164	2.63375
89% : 11%	6.683333	7.66666	1.50844	2.47934
87% : 13%	6.433333	6.833333	1.51024	2.62279

By tabulating *refractive index* versus *concentration ratio* before and after film excitation, one can see the linear relation between the variations in refractive index in both cases. Upon UV irradiation, resonance angles move towards bigger angles for TE polarization leading to a decrease in refractive index value [48]. In addition, the

modification presents strong accordance for each concentration, i.e. rise or fall in refractive index value takes place in parallel.

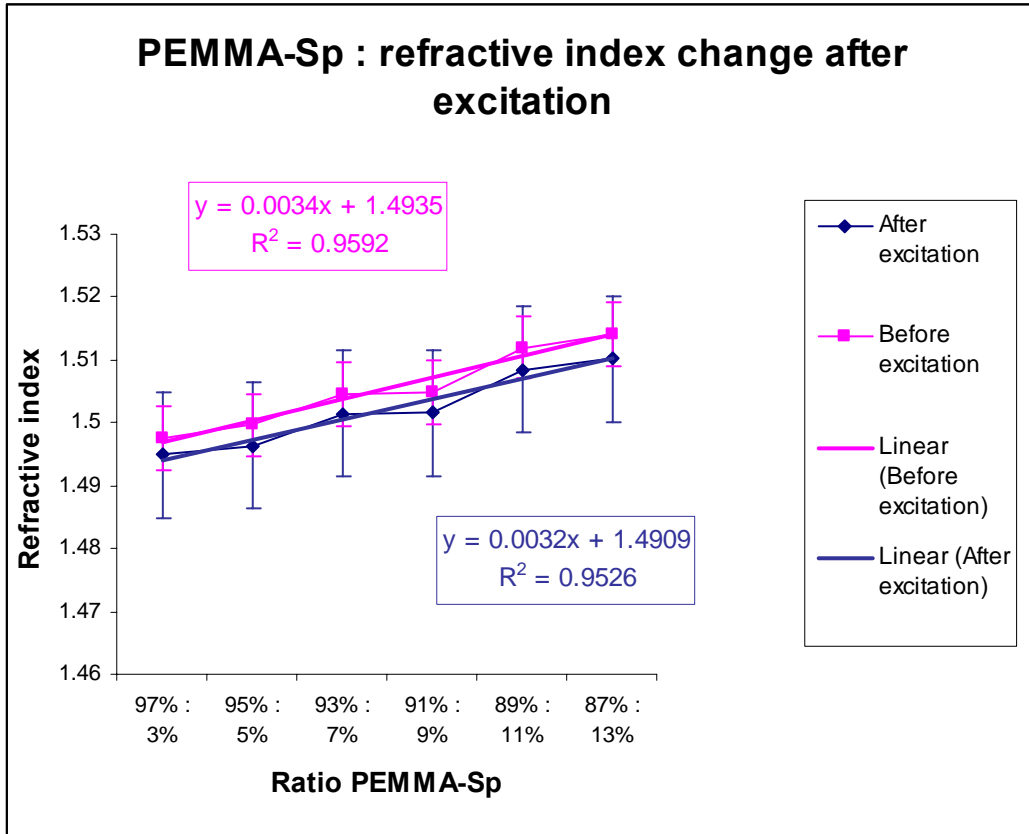


Figure 62. Refractive index changes of PEMMA - SP before (blue line) and after excitation (red line)

5.4 Fatigue

A significant disadvantage of the photochromic materials is the fatigue phenomenon. The photochemical fatigue resistance of dye-doped polymer films can be described by the changes in I_0 , I_n upon repeated UV irradiation cycles, where I_0 and I_n , represent the colored form transmittance values in the photostationary state obtained on the first and n^{th} transmittance cycles, respectively.

In detail, Figure 62 depicts 8 repetitions of the optomechanical cycle of the same sample, and its reversible optically induced mechanical actuation is clearly demonstrated. For the UV irradiation of the sample 56 counts are used. The end of each cycle, as the sample relaxes upon green irradiation, is considered as it reaches its initial position (bounded at 82% transmittance intensity). As the irradiation cycles are repeated, the sample shows a mechanical fatigue demonstrated in fig by the reduction of maximum displacement of the transmitted beam. The maximum length reduction is obtained at the first mechanical cycle.

The dye shows this fatigue phenomenon when constantly being changed from one isomer to another. Side reactions that can occur like photooxidation or undesired cis-trans isomerizations are strongly related to that drawback. Although from the results obtained that tension is clearly demonstrated, yet for 8 illumination cycles the dye displayed very little degree of fatigue. This fatigue resistance of spiropyran dye makes it a strong candidate for many applications as a photochromic switch.

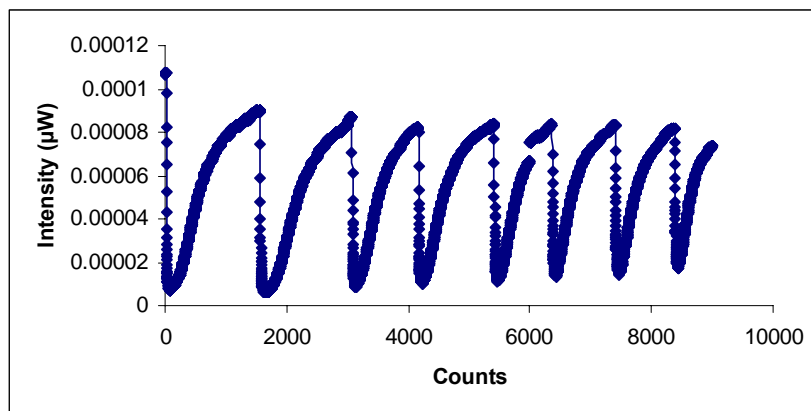


Figure 63. Fatigue of Spiropyran after eight optomechanical cycles

Chapter 6

Conclusions

Throughout the present project the refractive indices of several dielectric films deposited on quartz substrates under different reaction conditions have been determined by the prism film coupler method. A glass prism held against a film is mounted on a turntable base, so that a laser beam can enter the prism face at any desired angle. Pressure is then applied to vary the air gap between the prism and the film until a bright streak of laser light is observed in the film accompanied by the appearance of bright or dark m-lines on the screen. An evanescent optical wave is launched in the air gap contacting the exposed major surface of the transparent thin film. Such an evanescent wave can be launched from the optical prism coupler medium, when an optical beam in the prism is incident on its base at an angle greater than the critical angle for total internal reflection with respect to the air gap. The coupling of the laser beam into the film depends on the characteristics of the film and substrate used. In order to support propagating modes in the film, the refractive index of the prism n_p must be greater than both the refractive indices of the film n_f and substrate n_s , as well as, the refractive index of the film must be greater than that of the substrate and the cover. ($n_p > n_f > n_s > n_c$). That is the necessary condition for wave guiding in the film.

In general, the coupling is governed by the angle θ of incidence of the light onto the prism base. This angle θ determines the phase velocity in propagation direction (z), $u_i = c / (n_p \sin\theta)$, of the incident wave in the prism and in the gap. Strong coupling of light into the film occurs only when we choose θ so that equals the phase velocity u_m of one of the characteristics modes of propagation in the guide ($m = 0, 1, 2, \dots$). Thus, by determining these synchronous angles θ_m of strongest coupling, we find experimentally the

characteristic propagation constants of a given film, relative to the propagation constant $k = \omega / c$ of free space

$$N_m = \beta / k = c / u_m = n_p \sin\theta_m \quad ,$$

where β / k is the ratio of the velocity of light in vacuum to the phase velocity of the waveguide mode. The range of propagation constants N_m of the light along the prism base is related to the angle α of incidence on the entrance face of the prism by

$$N_m = n_p \cos[(90^\circ - \epsilon) + \sin^{-1}(\sin\alpha / n_p)]$$

If we let α to vary from $-\pi/2$ to $\pi/2$, we obtain the range of N-values possible with a given prism. In a film of index n_f deposited on a substrate of index n_s , all modes are in the interval $n_s < N_m < n_f$. In a typical case, a film of $3\mu\text{m}$ thick has five waveguide modes. Usually the values β / k obtained for the higher modes ($m \geq 5$), are not too accurate and therefore, an ideal waveguide should support less than five but more than two modes. In our case, all the films prepared ranged in thickness between $2\mu\text{m}$ to $3.5\mu\text{m}$ and the number of modes observed were minimum three to maximum five. The data obtained are fed into a computer program, which in turn, matches the observed β / k to the theoretical values computed by trying all possible combinations of the refractive index and the thickness of the film. This method provides an accuracy of 3 parts in 1000 for the calculated refractive index and $1\mu\text{m}$ for the film thickness.

In order to validate the prism film coupler method, we have attempt to characterize known films such as Polystyrene and PMMA both diluted in appropriate amount of Toluene. An agreement of four part in 1000 is obtained for the former solution, $n_f = 1.583$ in relation to the theoretical value $n_{\text{polystyrene}} = 1.586$ at laser wavelength 632.8nm . For the latter case, an agreement of one part in 1000 is obtained, $n_f = 1.485$ instead of the theoretical one, $n_{\text{PMMA}} = 1.486$.

With regard to the deviation from the related theoretical values, one of the causes of errors is the determination of the reference angle, equivalent to the goniometer table position, where the incident beam is perpendicular to the incidence face of the prism. In

our measurements, we determine the reference angle by manually adjusting the table, so that the laser beam reflected from the incidence face of the prism returns to the incidence direction. Due to this manual adjustment and visual identification, the main random error occurs. Another possible error originates from the determination of the exact position of the dark m-line, since its visibility is often restricted due to a non good quality thin film. In addition, excessive pressure applied against the prism base often broadens the modes altering their shape and shifts them slightly away from the synchronism direction. According to the formula stated for the propagation constants N_m , the most important parameters of a coupling prism are its refractive index n_p and the prism angle ε_p , thus, particular care must be taken for their evaluation before performing the actual measurements. Furthermore, the greater accuracy in the calculated PMMA's refractive index compared to the Polystyrene's one, might be attributed to the number of modes obtained for each film. In the latter case, the observed five modes seems to have introduced less accuracy in the characterization of the film in relation to the three modes obtained with the former case. That appears as a possible indication for the necessary requirement of a minimum number of modes supported for a waveguide.

The prism film coupler method was also used to demonstrate the possibility of controlling the refractive index of films containing inorganic- organic hybrids systems doped with zirconium. The sol gel process used is the most popular one among other available techniques for the fabrication of such systems (typically a metal oxide). The method is a wet chemical technique starting from a chemical solution containing colloidal precursors (sol). Typical precursors are metal alkoxides which undergo hydrolysis and polycondensation reactions to form a colloid, a system composed of solid particles (size ranging from 1nm to 1 μ m) immersed in a solvent. The sol evolves, then, towards the formation of an inorganic network containing a liquid phase (gel). Formation of a metal oxide involves connecting the metal centers with oxo (M-O-M) or hydroxo (M-OH-M) bridges, therefore generating metal – oxo or metal hydroxo polymers in solution. The drying process serves as to remove liquid phase from the gel, thus, forming a porous material, then a thermal treatment (firing) may be performed in order to further polycondensation and enhance of mechanical properties. The material produced by sol-gel synthesis constituted of a silicon alkoxide species that also possessed methacrylate

functionality. Stabilized zirconium alkoxide precursors were added to the precursor solution in order to reduce drying times and impart mechanical stability to deposited films. The systems fabricated by sol gel method have presented a linear variation of their refractive indices in relation to composition range. The basic index can be 1.48986 (at 632.8nm laser wavelength) using silicate precursors (without zirconium added) and increases up to 1.54379 using zirconium as a dopant. Similar behavior is presented with the use of infrared laser (825nm): the variation presented ranges from 1.47446, for the control sample, up to 1.53438. Organic – inorganic hybrid materials have properties similar to glasses with high transparency in visible and NIR ranges, therefore, no attenuation is expected for our waveguide measurements at those laser wavelengths. In general, sol – gels are created in low temperature process that utilizes the colloidal silica suspension to create porous silicate gel of high purity. The introduction of dopants in the sol-gel alters the resulting silica structure and thus be used to produce glasses with novel optical properties [45].

Photochromism is usually defined as the reversible color change observed upon UV or visible irradiation. Photochromic materials typically undergo photoreactions that proceed by means of excited states that cause changes in molecular structure or conformation, thereby altering the UV-visible (UV-vis) absorption spectra and the index of refraction of the sample. Therefore, the different optical and structural phenomena induced by irradiation with polarized light of thin polymer films containing photochromic molecules, can be well demonstrated by the use of the prism - film coupler method. In this project, photochromic 1, 3, 3-trimethylindolino-6'-nitrobenzopyrylospiran was used as the active materials doped in the polymeric matrix of PEMMA. The closed form of spiropyran (SP) has an absorption band situated in the UV region (between 320nm-400nm) and is thus colorless. Upon UV irradiation, heterolytic C-O ring cleavage takes place, leading to the formation of the open zwitterionic colored form, which has strong absorption in the visible region. The open photomerocyanine (MC) form of SP has a fully delocalized π -electron system and a red shift in absorption spectrum (from the UV to the 500-600nm band) accompanying the ring opening. Irradiation with visible light induces back conversion to the closed colorless form. The above behavior of SP doped in the polymeric matrix of PEMMA is in good agreement with the experimental results

obtained during the realization of the project. The absorption spectrum of SP-PEMMA films show a maximum absorption at the UV region, while after excitation with a 308nm pump laser, a peak is introduced in the region of 500-600nm. This red shift in absorption spectrum upon UV irradiation is accompanied with a change of color at the excited region of the film, which becomes purple in contrast with the surrounding unexcited colorless area. Doping PEMMA with SP molecules results in the increase in refractive index of the polymer matrices, in accordance with the peak introduced at UV region of the absorption spectrum of PEMMA after doping. In addition, the refractive index increment presents a strong linear relation to the concentration of the photochrome.

The photoinduced phenomena described above result in a change in the refractive index of SP doped PEMMA films before and after excitation with UV irradiation. As already stated, coupling of energy from the prism into the film takes place via the excitation of evanescent waves in the air layer. An evanescent wave is characterized by an exponentially decreasing value of intensity in the gap as a function of distance from the surface of the medium. The evanescent field leaking into the waveguide matches its propagation constant and a mode is resonantly excited at the expense of the reflected light intensity $R(\theta)$, which then shows a sharp dip as a function of the angle θ . The value of R depends on the combination of incident light frequency and angle of incidence, thus, any absorption of incident light causing refractive index modification, results in an angular shift of the resonance dip. During the experimental procedure the incident-angle dependence of reflectance was detected by a photodiode by varying its position in parallel with the rotary stage. After scanning the intensity profile of the reflected beam in relation to the incident angle, sharp dips clearly demonstrated the related resonant modes excited in the film. Furthermore, in order to record the refractive index change due to UV excitation, a second laser was introduced working at 543.5nm wavelength. Our intention has been to measure the variation in the refractive index of the material by the pump (UV) induced translation of the probe (543.5nm) m-line. The results based on the measurements of the 0th order mode displacement, have demonstrated a small change in refractive index of SP – PEMMA films after excitation. Resonance angles moved towards bigger angles for TE polarization leading to a decrease in refractive index value.

In addition, the variations in refractive index showed a strong linear relation to spiropyran concentration.

Finally, in order to verify photochemical degradation, we have recorded the photochemical fatigue resistance of the SP under repeated UV and visible irradiation cycles. The decrease in transmittance length after eight repeated cycles was obvious, yet slightly deviated from the initial one. The spiropyran shows, therefore, relatively low levels of fatigue. Moreover, a last remark that should be made is that fatigue seems to be one of the causes of errors in the determination of the resonance shift in relation to the reference angle. Repeated cyclizations will miss the initial position of reflectance minimum introducing a supplement factor of inaccuracy.

Appendix A

```
(*****  
  
    Adapted from  
    Roman E. Maeder: Programming in Mathematica,  
    Second Edition, Addison-Wesley, 1991.  
  
    *****)  
  
(* set up the package context, included any imports *)  
  
BeginPackage["MyPackages`Slabv3`"]  
  
Needs["Statistics`DescriptiveStatistics`"] (* read in any hidden  
imports \  
*)  
  
(* usage messages for the exported functions and the context itself *)  
  
Skeleton::usage = "Skeleton.m is a package for slab waveguide  
analysis."  
  
betaF::usage = "betaF[Angles,nc,np,prism angle]=mode indices ."  
  
teModes::usage = " teModes[mode indices, ns, nc, lambda]=ri and  
thickness "  
  
tmModes::usage=" tmModes[mode indices, ns, nc, lambda]=ri and thickness  
"
```

```

Begin["`Private`"]      (* begin the private context *)

te[modeIndex_List,nf_,ns_,nc_,k_] :=
  Module[{a,b,i1,i2,n,v},
    a=(ns^2-nc^2)/(nf^2-ns^2);
    b=(modeIndex^2-ns^2)/(nf^2-ns^2);
    i1=ArcTan[Sqrt[b/(1-b)]] + ArcTan[Sqrt[(b+a)/(1-b)]];
    i2=Table[i1[[n]]+(n-1) Pi,{n,Length[i1]};
    v=i2/Sqrt[1-b];
    v/(k Sqrt[nf^2 - ns^2])
  ]

tm[modeIndex_List,nf_,ns_,nc_,k_] :=
  Module[{a,b,d,qs,i1,i2,n,v},
    qs=modeIndex^2/nf^2 + modeIndex^2/ns^2 - 1;
    a=nf^4/nc^4 * (ns^2-nc^2)/(nf^2-ns^2);
    b=(modeIndex^2-ns^2)/(nf^2-ns^2)*(nf^2)/(qs*ns^2);
    d=(1-ns^2)/nf^2 * (1-nc^2)/nf^2;
    i1=ArcTan[Sqrt[b/(1-b)]]+ArcTan[Sqrt[(b+a*(1-b*d))/(1-b)]];
    i2=Table[i1[[n]] + (n-1) Pi, {n,Length[i1]};
    v=i2/(Sqrt[qs]*nf/ns*Sqrt[1-b]);
    v/(k Sqrt[nf^2-ns^2])
  ]

betaF[theta_List,nc_,np_,phi_] :=
  np Cos[90 Degree - phi Degree + ArcSin[nc Sin[
theta Degree]/np]]/nc//N

teModes[modeIndex_List,ns_,nc_,lambda_] :=
  Module[{k,ri,filmIndex,dummy},
    k=2 Pi/lambda;
    ri=NMinimize[Variance[te[modeIndex,nf,ns,nc,k]],
      {nf,modeIndex[[1]]+1 10^(-5),modeIndex[[1]]+1 10^(-3)}];
    filmIndex=nf/.ri[[2,1]];
    Plot[Evaluate[te[modeIndex,x,ns,nc,k] 1 10^6],

```

```

    {x,modeIndex[[1]]+(filmIndex-modeIndex[[1]])/2,
    filmIndex+(filmIndex-modeIndex[[1]])/2},
    AxesLabel -> {"RI", "Thickness (microns)"},
    AxesOrigin -> {modeIndex[[1]]+(filmIndex-modeIndex[[1]])/2,
    te[modeIndex,filmIndex+(filmIndex-modeIndex[[1]])/2,
    ns,nc,k][[1]]*1 10^6}
];
Print["Thickness = ",N[Mean[te[modeIndex,
    filmIndex,ns,nc,k]],3]];
Print["Refractive index = ",N[filmIndex,6]];
]

tmModes[modeIndex_List,ns_,nc_,lambda_] :=
Module[{k,ri,filmIndex,dummy},
    k=2 Pi/lambda;
    ri=NMinimize[Variance[tm[modeIndex,nf,ns,nc,k]],
        {nf,modeIndex[[1]]+1 10^(-5),modeIndex[[1]]+1 10^(-3)}];
    filmIndex=nf/.ri[[2,1]];
    Plot[Evaluate[tm[modeIndex,x,ns,nc,k] 1 10^6],
        {x,modeIndex[[1]]+(filmIndex-modeIndex[[1]])/2,
        filmIndex+(filmIndex-modeIndex[[1]])/2},
        AxesLabel -> {"RI", "Thickness (microns)"},
        AxesOrigin -> {modeIndex[[1]]+(filmIndex-modeIndex[[1]])/2,
        tm[modeIndex,filmIndex+(filmIndex-modeIndex[[1]])/2,
        ns,nc,k][[1]]*1 10^6}
    ];
    Print["Thickness = ",N[Mean[tm[modeIndex,
        filmIndex,ns,nc,k]],3]];
    Print["Refractive index = ",N[filmIndex,6]];
]

End[]      (* end the private context *)

Protect[ betaF,teModes,tmModes ]      (* protect exported symbols *)

EndPackage[] (* end the package context *)

```

Appendix B

```
BeginPackage["ModesNumber`"];
(*Load required packages*)

Needs["Statistics`DescriptiveStatistics`"]
(*Usage messages for exported functions*)

GetFileRead::usage = "GetFileRead[filename_path] = the \
path of our file target as string"
TheModes::usage = "TheModes[la,lb,fringes,nfilm,nair,n\
sub,laserwave,gwnia] = the number of modes expected"
Begin["`Private`"];
(*Definitions*)
GetFileRead[file_String] := Module[{fileTarget},
  fileTarget = OpenRead[file];
  OurData = (ToExpression[#1] & ) /@
    (StringSplit[#1] & ) /@ Flatten[
      (StringReplace[#1, ",", "-> "."] & ) /@
        Drop[ReadList[file, Record, RecordLists ->
          True], 84]]; ListPlot[OurData,
    PlotJoined -> True]]

TheModes[la_, lb_, fringes_, nfilm_, nair_, nsub_,
  laserwave_, ui_] := Module[{va, vb, Dm, u, d, a, k,
  v, m}, va = 1/la; vb = 1/lb; Dm = va - vb;
  d = fringes/(2*Dm*Sqrt[nfilm^2 - Sin[ui]^2]);
  a = d/2; k = (2*Pi)/laserwave;
  v = a*k*Sqrt[nfilm^2 - nsub^2];
  {m = N[Ceiling[(2*v - ArcTan[Sqrt[
    (nsub^2 - nair^2)/(nfilm^2 - nsub^2)])]/
    Pi]], d,
  N[(2*v - ArcTan[Sqrt[(nsub^2 - nair^2)/
    (nfilm^2 - nsub^2)])]/Pi]]]
(*Error Conditions*)
End[];
```

```
(*Protect exported values*)  
Protect[GetFileRead, TheModes];  
EndPackage[]
```

Appendix C

Sellmeier Dispersion Formula for the prism index according to the Schott Optical Glass catalogue [42]:

Sellmeier Dispersion Formula

$$n^2(\lambda) - 1 = B_1\lambda^2 / (\lambda^2 - C_1) + B_2\lambda^2 / (\lambda^2 - C_2) + B_3\lambda^2 / (\lambda^2 - C_3)$$

Constants of Dispersion Formula	
B ₁	1.77931763
B ₂	0.338149866
B ₃	2.08734474
C ₁	0.0133714182
C ₂	0.0617533621
C ₃	174.01759

Sellmeier Dispersion Formula for the quartz index according to the fused silica dispersion [43]:

$$\varepsilon = 1 + \frac{a_1\lambda^2}{\lambda^2 - l_1^2} + \frac{a_2\lambda^2}{\lambda^2 - l_2^2} + \frac{a_3\lambda^2}{\lambda^2 - l_3^2},$$

where

$$a_1 = 0.69616630, \quad l_1 = 0.068404300,$$

$$a_2 = 0.40794260, \quad l_2 = 0.11624140,$$

$$a_3 = 0.89747940, \quad l_3 = 9.8961610,$$

Wavelength is measured in micrometers.

References

- [1] “*Optics*”, Hecht Eugene, pp. 125-128
- [2] “*Modes of propagating light waves in thin deposited semiconductor films*”, P.K. Tien, R. Ulrich and R.J. Martin Appl. Phys. Letters Vol. 14, No 9
- [3] “*Guided - wave technique for the measurement of dielectric thin - film materials’ thermal properties*”, P. Huguet - Chantome, L. Escoubas and F. Flory Appl. Optics June 2002, Vol. 41, No 16
- [4] “*Introduction in Electrodynamics II*”, Griffith David, pp. 163-164
- [5] “*Introduction in Electrodynamics II*”, Griffith David, pp. 158-160
- [6] “*Quantum Mechanics I*”, Trahanas Stefanos, pp. 292-301
- [7] “*Theory of Prism-Film Coupler and Thin-Film Light Guides*”, P. K. Tien and R. Ulrich, Journal of the Optical Society of America, Vol 60, No 10
- [8] “*Integrated Optics: Theory and technology*”, R.G. Hunsperger
- [9] “*m - lines technique*”
- [10] “*Measurement of Thin Films Parameters with a Prism Coupler*”, R. Ulrich and R. Torge Applied Optics, Vol.12, No 12
- [11] “*Perspectives in Photochromism: A novel System Based on the 1,5 Electrocyclization of Heteroanalogous Pentadienyl Anions*”, Heinz Durr Chem. Int. Ed. Engl. 28 (1989) pp. 413-431
- [12] “*Organic Photochromism*”, H. Bouas – Laurent, H. Durr Pure App. Chemistry, Vol. 73, No 4, pp. 639-665, 2001
- [13] “*Two-Photon Photopolymerization and 3D Lithographic Fabrication*”, Hong-Bo Sun and Satoshi Kawata APS (2004), Vol. 170, pp. 169-273
- [14] “*Spiropyrans*”, Robert C. Bertelson
- [15] “*Factors Influencing Photochromism of Spiro – Compounds Within Polymeric Matrices*”, G. Such, R. A. Evans, L. H. Yee and Thomas P. Davis Journal of Macromolecular Science, Vol. C, No \$, pp 547-579, 2003
- [16] “*Organic Photochromic and Thermochromic compounds*”, Vol. 1, John C Carno and Robert Gugliemetti Press, New York, 1999

- [17] “MNDO-PM3 MO studies on the thermal isomerization of photochromic 1, 3',3' – trimethyl-6-nitrospiro[2h-1-benzopyran-2,2-indoline]”, Yasuo Abe, R. Nakao, T. Horii, S. Okada, M. Irie J. of Photochem. And Photobiology A: Chemistry 95 pp. 209-214
- [18] “Photochromism in Spiropyrans. Part IV. Evidence for the existence of several forms of the colored modification”, R. Heiligman-Rim, Y. Htrshberg and E. Fischer J. Chem. Soc., Vol. 150 (1961)
- [19] “Photoprocess in spiropyran – derived merocyanines: singlet versus triplet pathway”, H. Gorner, L. S. Atabekyan, Alexander K. Chibisov Chemical Physics Letters 260 (1996) pp.59-64
- [20] “Photochemical ring opening in nitrospiropyrans: triplet pathway and the role of singlet molecular oxygen”, H. Gorner Chemical Physics Letters, Vol. 282, (1998) pp. 381-390
- [21] “Photochromism in Spiropyrans. Part V On the Mechanism of phototransformation”, R. Heiligman-Rim, Y. Hirshberg and E. Fischer J. Chem. Soc., Vol. 66 (1961), pp. 2470 – 2477
- [22] “Laser controlled mechanical actuation of photochromic – polymer microsystems”, A. Athanassiou, M. Kalyva, K. Lakiotaki, S. Georgiou and C. Fotakis Rev. Adv. Mater., Vol. 5 (2003) pp. 245-251
- [23] “Sol – Gel science, the physics and chemistry of sol-gel processing”, Brinker CJ, Scherer
- [24] “Scaling Rules For Thin-Film Optical Waveguides”, H. Kogelnik and V. Ramaswamy Applied Optics, Vol. 13, No 8 (1974)
- [25] “Measuring anisotropic refractive indices and film thickness of thin organic crystals using the prism coupling method”, G. Zhang and K. Sasaki Applied Optics, Vol27, No 7 (1988)
- [26] “Optical characterization of thin films by guided waves”, E. Pelletier, F. Flory and Y. Hu Applied Optics, Vol. 28, No 14 (1989)
- [27] “The determination of thin film thickness using reflectance spectroscopy”, Varian UV At Work No 090, www.varianinc.com
- [28] “Fundamentals of Optics: Lectures 16&17”, Li Qian

- [29] “*Nonlinear coupling in a planar waveguide*”, M. Berlotti, E. Fazio, A. Ferrari, F. Michelotti, G. C. Righini and C. Sibilìa *Optics Letters*, Vol. 15, No 8 (1990)
- [30] “*Stress effects in prism coupling measurements of thin polymer films*”, A. Agan, F. AY, A. Kocabas and A. Audinli *Appl. Phys. A*, Vol. 80, pp. 341-345 (2005)
- [31] “*Investigation of the two- photon polymerization of Zr-based inorganic-organic hybrid material system*”, B. Bhuian, R.J. Winfield, S. O’Brien, G. M. Crean *Applied Surface Science*, Vol. 252, pp 4845 – 4849 (2006)
- [32] “*Integrated optics based on organo-mineral materials*”, P. Coudray, P. Etienne, Y. Moreau *Invited paper (European Materials conference – Strasbourg-June 99)*
- [40] “*Light – induced refractive index modifications in dielectric thin films: experimental determination of relaxation time and amplitude*”, S. Monneret, S. Tisserand, F. Flory and H. Rigneault *Applied Optics*, Vol. 35, No 25 (1996)
- [41] “*Optical characterization of ZnO, SnO₂, and TiO₂ thin films for butane detection*”, T. Mazingue, L. Escoubas, L. Spalluto et al *Applied Optics*, Vol. 45, No 7 (2006).
- [42] http://www.us.schott.com/optics_devices/english/download/datasheet_all_us.pdf
- [43] http://en.wikipedia.org/wiki/fused_silica
- [44] “*Light Waves in Thin Films and Integrated Optics*”, P. K. Tien *Appl. Optics*, Vol. 10, No 11, pp.2395-2413, 1971
- [45] “*Thin Organosilicon Films for Integrated Optics*”, P. K. Tien, G. Smolinsky and R. J. Martin *Appl. Optics*, Vol. 11, No 3, pp. 637-642, 1972
- [46] “*An efficient method for measuring the parameters of single mode anisotropic slab waveguides using the prism-coupling technique*”, F. Gao, G. Du, Vannadeth, P. Zhang and F. Lun *Wiley Periodicals* 2005, Inc.
- [47] “*Photoinduced manipulations of photochromes in polymers: Anisotropy, modulation of the NLO properties and creation of surface gratings*”, Y. Atassi, J. Chauvin, J. A. Delaire, J. F. Delouis, I. Fantome-Maltey and K. Nakatani *Pure and Appl. Chemistry*, Vol. 70, No 11, pp. 2157-2166, 1988
- [48] “*Electrochromic and optical waveguide studies of corona – poled electro - optic polymer films*”, R.H. Page, M. C. Reck, A. Sen, R. J. Twieg, J.D. Swalen, G. C. Bjorklund, and C. G. Willson, *Opt. Soc. Am. B*, Vol 7, No 7, pp1239-1250, 1990

[49] “*Ultrafast wide range all-optical switch using complex refractive-index changes in a composite film of silver and polymer containing photochromic dye*”, Journal of Appl. Physics, Vol. 83, No 6, pp 2894-2900, 1998